Photoionization of isomeric molecules: From the weak-field to the strong-field limit

by

STEFAN JOHN ZIGO

B.S., University of Michigan, 2011

AN ABSTRACT OF A DISSERTATION

submitted in partial fulfillment of the
requirements for the degree

DOCTOR OF PHILOSOPHY

Department of Physics
College of Arts and Sciences

KANSAS STATE UNIVERSITY
Manhattan, Kansas

2017

Abstract

Ultra-fast spectroscopy has become a common tool for understanding the structure and dynamics of atoms and molecules, as evidenced by the award of the 1999 Nobel Prize in Chemistry to Ahmed H. Zewail for his pioneering work in femtochemistry. The use of shorter and more energetic laser pulses have given rise to high intensity table-top light sources in the visible and infrared which have pushed spectroscopic measurements of atomic and molecular systems into the strong-field limit. Within this limit, there are unique phenomena that are still not well understood. Many of such phenomena involve a photoionization step.

For three decades, there has been a steady investigation of the single ionization of atomic systems in the strong-field regime both experimentally and theoretically. The investigation of the ionization of more complex molecular systems is of great interest presently and will help with the understanding of ultra-fast spectroscopy as a whole. In this thesis, we explore the single ionization of molecules in the presence of a strong electric field. In particular, we study molecular isomer pairs, molecules that are the same elementally, but different structurally. The main goal of this work is to compare the ionization yields of these similar molecular pairs as a function of intensity and gain some insight into what differences caused by their structure contribute to how they ionize in the strong-field limit. Through our studies we explore a wavelength dependence of the photoionization yield in order to move from the multi-photon regime of ionization to the tunneling regime with increasing wavelength. Also, in contrast to our strong-field studies, we investigate isomeric molecules in the weak-field limit through single photon absorption by measuring the total ionization yield as a function of photon energy.

Our findings shed light on the complexities of photoionization in both the strong- and weak-field limits and will serve as examples for the continued understanding of single ionization both experimentally and theoretically.

Photoionization of isomeric molecules: From the weak-field to the strong-field limit

by

Stefan John Zigo

B.S., University of Michigan, 2011

A DISSERTATION

submitted in partial fulfillment of the
requirements for the degree

DOCTOR OF PHILOSOPHY

Department of Physics
College of Arts and Sciences

KANSAS STATE UNIVERSITY
Manhattan, Kansas

2017

Approved by:

Major Professor
Carlos Trallero-Herrero

Copyright

Abstract

Ultra-fast spectroscopy has become a common tool for understanding the structure and dynamics of atoms and molecules, as evidenced by the award of the 1999 Nobel Prize in Chemistry to Ahmed H. Zewail for his pioneering work in femtochemistry. The use of shorter and more energetic laser pulses have given rise to high intensity table-top light sources in the visible and infrared which have pushed spectroscopic measurements of atomic and molecular systems into the strong-field limit. Within this limit, there are unique phenomena that are still not well understood. Many of such phenomena involve a photoionization step.

For three decades, there has been a steady investigation of the single ionization of atomic systems in the strong-field regime both experimentally and theoretically. The investigation of the ionization of more complex molecular systems is of great interest presently and will help with the understanding of ultra-fast spectroscopy as a whole. In this thesis, we explore the single ionization of molecules in the presence of a strong electric field. In particular, we study molecular isomer pairs, molecules that are the same elementally, but different structurally. The main goal of this work is to compare the ionization yields of these similar molecular pairs as a function of intensity and gain some insight into what differences caused by their structure contribute to how they ionize in the strong-field limit. Through our studies we explore a wavelength dependence of the photoionization yield in order to move from the multi-photon regime of ionization to the tunneling regime with increasing wavelength. Also, in contrast to our strong-field studies, we investigate isomeric molecules in the weak-field limit through single photon absorption by measuring the total ionization yield as a function of photon energy.

Our findings shed light on the complexities of photoionization in both the strong- and weak-field limits and will serve as examples for the continued understanding of single ionization both experimentally and theoretically.

Table of Contents

List of Figures

List of Tables

Acknowledgments

In total, my graduate studies at Kansas State University have spanned the course of six years. Throughout this time, I have encountered many challenges that I could never have faced without the support of many people. First and foremost, I would like to thank my family in Michigan for their unwavering love and support from a distance. Although they still only barely know that my research involves lasers of some kind, they have never stopped taking the time to listen to me recall my graduate school adventures and encourage me to "keep my nose to the grindstone."

A PhD is not simply a credential on a piece of paper. Instead, it is a journey full of intellectual growth and self discovery, both personally and professionally. In that sense, I have my advisor, Dr. Carlos Trallero-Herrero, to thank for his guidance throughout this journey. In addition to being a source of knowledge and experience, he was always willing to listen to what I had to say, even when I was disagreeing with him. His ever present optimism and sense of humor have always been a welcomed attribute that have gotten me through the toughest of projects.

I owe a great deal of my growth and sanity to my fellow research group mates. They are not only my coworkers, but also my friends. To them, I am forever indebted. Although my search for a deeper physical understanding of nature was all I truly needed to get out of bed in the morning, the fact that I had a supportive team of fantastic people to interact with on a daily basis was a definite plus in that regard. All jokes aside, I would like to thank Derrek Wilson for helping me to better understand nonlinear optical techniques, Adam Summers for always being the professional voice of reason, Pratap Timilsina for his moral support through the classes we took together and for building the time-of-flight mass spectrometer used throughout this thesis, Jan Troß for his good natured humor, and Wes Erbsen for helping set the tone of my main research projects and teaching me the experimental fundamentals of ultrafast spectroscopy. Also, in general, I would like to thank the James R. Macdonald

Laboratory as a whole. There is no finer example of comradery in the research world than that of the students and faculty of the JRM lab. It did not matter which research group you were a part of or what project you were working on, everyone always found time to help each other. I am especially thankful to the JRM support staff: Al Rankin, Mike Wells, Scott Chainey, Vince Needham, and Chris Aikens. Throughout the years, they were always willing to help me with what they probably considered to be trivial issues.

I would like to thank my PhD committee members, Artem Rudenko, Chii-Dong Lin, and Christine Aikens. Also, my outside chairperson, Will Hageman. In addition to being my committee members, they were also my teachers and mentors. Their advice and encouragement throughout my graduate school career were always appreciated. In addition, special thanks to A. T. Le for his theory support regarding the SFI of isomeric molecules. Also, Daniel Rolles for inviting me to participate in an ALS beamtime that resulted in significant weak-field ionization measurements pertaining to the theme of this thesis.

As a brief aside, from a time prior to my life in Kansas, I would like to thank my undergraduate research advisor, Dr. Georg Raithel, and his graduate student at the time, Eric Paradis, for helping me to fall in love with AMO physics research. Eric was my graduate student mentor for two and a half years at the University of Michigan. He taught me everything fundamental I know about optics in a laboratory setting and had the patience to teach me how to align optical setups. My quick involvement and solid start in research in the JRM lab is mainly due to his help in setting an experimentalist's foundation within me, prior to attending graduate school. Throughout my time at KSU, I have attempted to be as good of a mentor to other students as Eric was to me.

Finally, I would like to thank Colleen Geertsema for constantly reminding me that there is a world outside of the lab and that I should take the time to enjoy it!

Chapter 1

Introduction

Through fundamental atomic and molecular research, a better understanding of the structure and dynamics of atomic and molecular systems can lead to the prediction within and ultimate control of those systems. This type of deeper understanding can provide a base for new technologies that has the potential to be impactful on both a local and global scale. Such technologies can be used to advance improvements in environmental protection, clean energy production, medical procedures, and defense applications. [1]

One approach to studying atomic and molecular systems is through the use of ultra-fast, ultra-intense laser pulses. The journey to femtosecond laser sources started with solid-state and organic dye lasers in the early 1960's and 70's [2, 3]; however, they were considered impractical and inefficient. Now considered a benchmark in ultrafast development, it was the realization of Kerr-lens mode-locked Ti:sapphire laser oscillators, in the 1980's, that allowed for a dramatic increase in femtosecond pulse output power [4, 5]. Table-top Ti:sapphire laser systems coupled with the chirped-pulse amplification technique [6] have since become the "work-horses" of the ultra-fast community producing sub-100 fs pulses with mJ level pulse energies, centered in the near infrared.

The development of femtosecond laser systems prompted the use of ultra-fast spectroscopy which has become a common tool for understanding the structure and dynamics of atoms and molecules. With the birth of femtochemistry in the 1980's, as evidenced by

the award of the 1999 Nobel Prize in Chemistry to Ahmed H. Zewail for his pioneering work [7, 8] in the field, we witnessed an explosion of spectroscopic techniques that utilized the short time scales of table-top femtosecond laser sources. Over the next three decades, many new experimental techniques were introduced. One such technique was the camera shutter-like "pump-probe" experiment [7]. A "pump" pulse dresses a system, usually by excitation resulting in a dynamic process, and a second "probe" pulse, delayed with respect to the first pulse, accesses the evolution of the system on time scales faster than the phenomenon being studied. Another technique is strong-field photoionization spectroscopy [9]. Here, the interaction with the laser pulse is so strong that the binding potential of the system can bend as a function of time, releasing the electron to the continuum via multiphoton or tunneling ionization. The photoelectrons and resulting ion yields can be studied to better understand the energy structures of the system in the presence of the strong electric field. Finally, through the use of tunneling ionization, the unique phenomenon of higher-order harmonic generation (HHG) was observed [10–12], leading to the technique known as HHG spectroscopy. Described by the "three-step" model [13], a tunneled electron is accelerated in the laser field before finally recombining with the parent ion. The excess energy gained from the field interaction is released as a photon that is a harmonic of the central frequency of the driving field. Measuring the emitted harmonics can give insight to the structure of the system being studied [14]. It is important to note that the majority of strong-field phenomena or experimental techniques involve an ionization step. Therefore, in this thesis, the focus will mainly remain on the process of single strong-field photoionization.

High energy femtosecond laser sources capable of generating intensities $\geq 10^{13}\ W/cm^2$ allowed for the study of atomic and molecular systems in the presence of a strong electric field. Essentially, the laser pulses are so intense that perturbative theoretical approaches break down which lead to nonlinear phenomena. Although originally theorized in the late 1960's [15–17], the ability to work experimentally in the strong-field limit was not realized until the 1980's [18]. Since then, the confirmation of theoretical models [15–17, 19–23] compared to experiment for atoms ionized in a strong electric field has become a prevalent research topic [24–27]. Through these studies, the contributions of different ionization regimes as

a function of intensity to the ionization yield were identified, such as multi-photon and tunneling ionization. It is a continued research endeavor to increase the dynamic range of intensity dependent ionization experiments [28] and further confirm our understanding of atomic strong-field ionization.

Although presently the treatment of atoms in the strong-field limit is considered to be relatively well understood, the treatment of more complex molecular systems is still a growing development, both experimentally [29–33] and theoretically [34–40]. The differences between strong-field ionization of atoms compared to molecules of similar ionization potential were investigated [29–31] and it was determined that the differences arise from the arrangement of the molecular bonds and the corresponding molecular orbitals. In order to better understand the effects that structure and bond placement have on ionization, in this thesis, molecular isomer pairs, same chemical formula, but different elemental arrangement, are investigated. The study of isomeric molecules in the strong-field limit was studied in the past via HHG spectroscopy [41–44] and photoionization [45, 46] in general; however, few studies were made with the intent of comparing the ionization yields of isomer pairs as a function of intensity.

Contrasting the use of femtosecond laser systems for the study of molecular systems, is the use of synchrotron radiation. Starting as an accidental bi-product of accelerating electrons in synchrotron accelerators in 1947 [47], the use of synchrotron radiation has become a standard light source for the study of molecular systems. 3rd generation facilities, considered X-ray sources with high brilliance, now exist and intentionally generate photons in the UV and soft X-ray regions of the spectrum. This allows for single photon ionization of both the valence and core electrons in molecular systems [48] and is an excellent source for scattering and X-ray imaging experiments [49]. The radiation is only intense enough to be considered in the weak-field limit of ionization. In this thesis, we aim to compare the ionization yields of weak-field ionized isomeric molecules to strong-field ionized isomeric molecules.

This chapter serves to give a general background and introduction to the topics covered in this thesis. Additional information with more in depth detail will be given in the chapters to come.

1.1 Thesis Outline

The primary goal of this thesis is to study the complexities of photoionization in both the strong- and weak-field limits such that they serve as examples for the continued understanding of single ionization both experimentally and theoretically. The strong-field studies are accomplished by measuring the ionization yields of isomeric molecules, experimentally, after the interaction with ultra-fast, ultra-intense light sources in the near-infrared. The complementing weak-field experiments measured the total ionization yields of isomeric molecules using synchrotron radiation in the extreme ultra-violet (XUV). Through our experiments, we show that the structure of molecules is more influential in the strong-field limit than in the weak.

We begin, in chapter 2, with a brief overview of the fundamentals of strong-field physics. Intensity dependent ionization regimes are explained. Both atomic and molecular strong-field ionization theoretical models are introduced. Since molecular ionization models are actively being developed, the availability of experimental molecular ionization data will help to further that development.

Next, in chapter 3, the process of making ionization yield measurements is explained through the introduction of experimental equipment/techniques, such as the time-of-flight mass spectrometer and single-shot intensity discrimination. Also, the main laser source used in the strong-field experiments is described: a high energy, Ti:sapphire, chirp pulse amplified femtosecond laser system with an optical parametric amplification option. Additionally, pulse characterization techniques are discussed, e.g. frequency resolved optical gating.

In chapter 4, the theoretical discussions of chapter 2 and the experimental techniques of chapter 3 are brought together to explain the importance of intensity in strong-field ionization experiments. The experiments performed in this thesis are all intensity dependent when in the strong-field limit; therefore, accurate intensity measurement is essential. With that in mind, the idea of external and internal laser characterization is explained. Ultimately, an intensity calibration method is introduced with additional comments on the benefits of the analysis process, robust fitting of theoretical to experimental ionization data.

Chapters 5 and 6 summarize a combination of experiments measuring the parent ion yields of molecular isomers as a function of intensity. The yields of the isomer pairs are compared in order to reveal the importance of structural differences in molecules as well as intensity dependent effects. Additionally, the light sources described in chapter 3 are utilized to perform wavelength dependent ionization studies in the range 790 - 2000 nm, which gives insight into the effects of the different strong-field ionization regimes described in chapter 2.

In chapter 7, we complement the results of chapters 5 and 6 by performing total ionization yield measurements in the weak-field limit at the Advanced Light Source at Lawrence-Berkeley National Lab. The same isomeric pairs are studied. Ionization via single photon absorption of XUV radiation, in our studies, is suggested to be less affected by the structure of the target molecule when compared to the multi-photon strong-field case.

Finally, in chapter 8, we summarize initial efforts to expand our molecular ionization studies into three new directions. The first of which is photoelectron spectroscopy. By resolving the energy distribution of the emitted photoelectrons in the strong-field limit, information about the electronic structure of the molecules can be extracted. Also, with the use of the ultra-fast "pump-probe" technique, the underlying dynamics can be better understood. Secondly, the wavelength dependent strong-field ionization studies can be advanced further into the infrared by using a newly developed intense femtosecond light source capable of producing light in the long-wave infrared (5500 - 8500 nm). Lastly, carrier envelope phase dependent spectroscopic studies can be explored through the use of a light source with excellent long-term single-shot carrier envelope stability ($\sim$ 300 mrad RMS error). Although there is still plenty of preliminary work to accomplish in all three new directions, eventually the same isomeric pairs from chapters 5, 6, and 7 can be studied. This will bring deeper insight into molecular structural effects in the strong-field limit.

Chapter 2

Strong-field Ionization Fundamentals and Theory

We begin this chapter by discussing what it means to be in the strong-field limit. We start with the fundamentals of strong-field ionization laid out by Keldysh [15] in 1965, where intensity dependent ionization regimes are described. Although the only true correct way to describe the phenomenon is through solving the time-dependent Schrödinger equation (TDSE), the current state of technology, as advanced as it is, causes this option to remain unrealistic. Regardless, since the work of Keldysh, many experimentally verified atomic ionization theories have been developed that are close approximations of the solution to the TDSE. In the first half of this chapter, we describe a few of these atomic theories. Overall, many consider the strong-field ionization of atoms in the VIS-NIR to be relatively well understood. Similarly, in the second half of this chapter, we explore the current state of molecular ionization theory. The added complexity of molecules both structurally and dynamically, cause the description of ionization to be very challenging in the theoretical sense. We introduce some of the current theories being developed in this active and growing field of research.

2.1 What is Strong-field Ionization?

As mentioned in the introduction, chapter 1, with the advancement of "table-top" laser technology came the realization of femtosecond laser pulses with high pulse energy outputs. As a result, the ability to generate peak intensities of 10^{13} W/cm^2 and higher has become common place. Working in the strong-field limit is considered the study and experimental investigation of the unique phenomena that occur at these higher intensities.

2.1.1 Single Electron Ionization Regimes

Once in the strong-field limit, ionization can be divided into three basic regimes: (i) multi-photon (MPI), (ii) tunneling (TI), and (iii) over-the-barrier ionization (OBI). Each regime will be described in greater detail in the following subsections. MPI is generally associated with low intensity, whereas TI and OBI are associated with high intensity. In terms of atomic and molecular systems, what is considered low intensity and what is considered high intensity is relative to the atomic binding potential of a single electron in the highest orbital of the ground state of the system. Keldysh defines this connection between electric field strength and ionization potential as γ, see ref.[15], which later became known as the Keldysh parameter:

$$\gamma = \sqrt{\frac{I_p}{2U_p}} \tag{2.1}$$

$$U_p = \frac{I}{(2\omega)^2} = \left(\frac{E_0}{2\omega}\right)^2 \tag{2.2}$$

where I_p is the ionization potential, U_p is the ponderomotive potential, I is the intensity, ω is the frequency, and E_0 is the field amplitude. Equations are shown in atomic units. As a side comment, when working with more colloquial units, a handy conversion for quick "back of the envelope" calculations is U_p (in eV) $\propto I$ (in 10^{14} W/cm^2) $\cdot(\lambda$ (in μm))^2.

Multi-Photon Ionization

There are enough photons such that it becomes significantly probable for multiple photons to interact with the same atom during the same laser pulse. Electronic states that were forbidden in the weak-field limit before are now accessible. In the extreme case, the atom absorbs enough photons to impart enough energy to an electron such that it overcomes the Coulomb potential barrier binding it to the atom. This is known as multi-photon ionization. Note that the electric field strength is not of the order of the atomic binding potential of the system and therefore $\gamma \gg 1$.

The ionization rate, in the multi-photon regime, for n photons is:

$$\omega_n = \sigma_n I^n \tag{2.3}$$

where n is the number of photons, σ_n is the n-photon cross section, and I is the intensity. For example in Fig. 4.4, the exponential n-photon intensity dependence of the ionization rate gives simple atomic systems the characteristic linear slope at low intensity in their parent ion yield as a function of intensity when plotted in a log-log plot.

Although in this thesis we focus mainly on the ionization yields of the parent ions, it is appropriate to also mention ionization yields of electrons and their corresponding energies. When in the multi-photon regime, we witness the phenomenon known as above-threshold ionization (ATI). In order to ionize an atom or molecule in this regime, $n\hbar\omega \geq I_p$, where $\hbar\omega$ is the photon energy of the light and I_p is the minimum energy required to remove an electron from its ground state. We visualize this effect in Fig. 2.2 and see that the electron energies are equally spaced by $\hbar\omega$ starting with E_0, the electron with the lowest energy above the ionization potential (i.e. $E_0 = -I_p + n\hbar\omega$). Note also that the probability of ionization decreases as a function of increasing photon absorption. An example of how ATI are measured experimentally is in section 8.1.2.

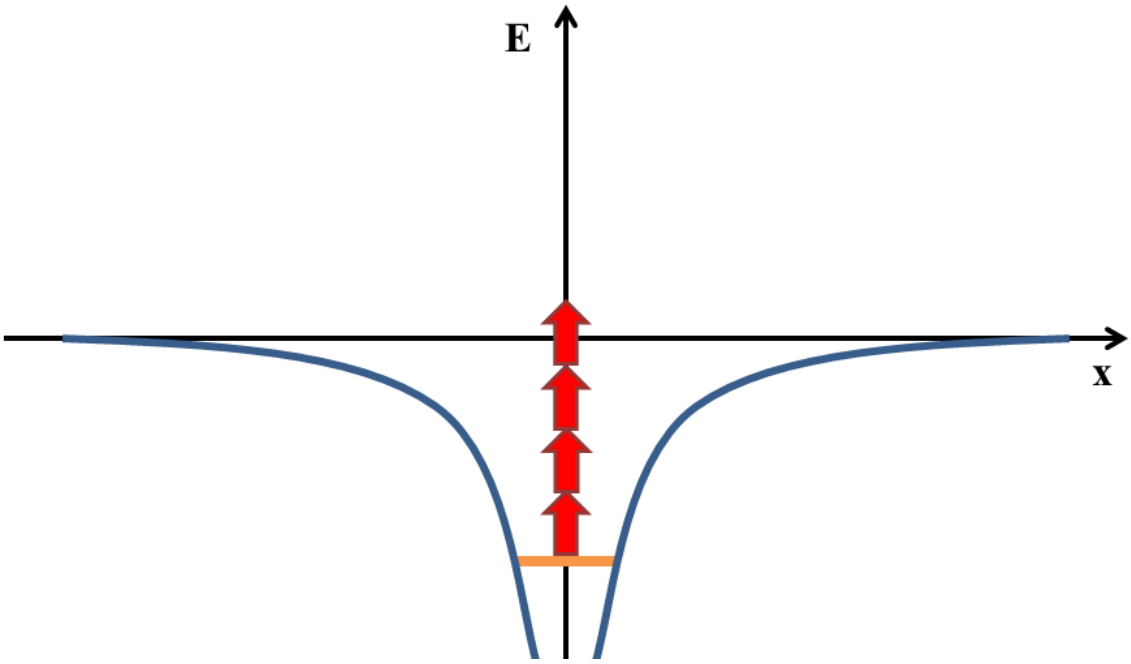

Figure 2.1: Multi-Photon Ionization: The electron absorbs many photons in order to overcome the binding potential of the atom.

Tunneling Ionization

As the intensity increases, we transition from the multi-photon regime into the tunneling regime. The electric field strength is now comparable to or greater than the atomic binding potential of the system, $\gamma \ll 1$. Essentially, the field has the strength to deform the potential such that the electron can tunnel through the Coulomb barrier. A semi-classical illustration of the tunneling picture is shown in Fig. 2.3

In the static picture, the tunneling ionization rate is:

$$\omega_{static} \propto \exp\left(-\frac{2(2I_p)^{3/2}}{3|E_{field}|}\right) \tag{2.4}$$

where I_p is the ionization potential and E_{field} is the instantaneous electric field strength. A more detailed and complete picture of tunneling ionization was described in ref. [19] and will be described in a later section.

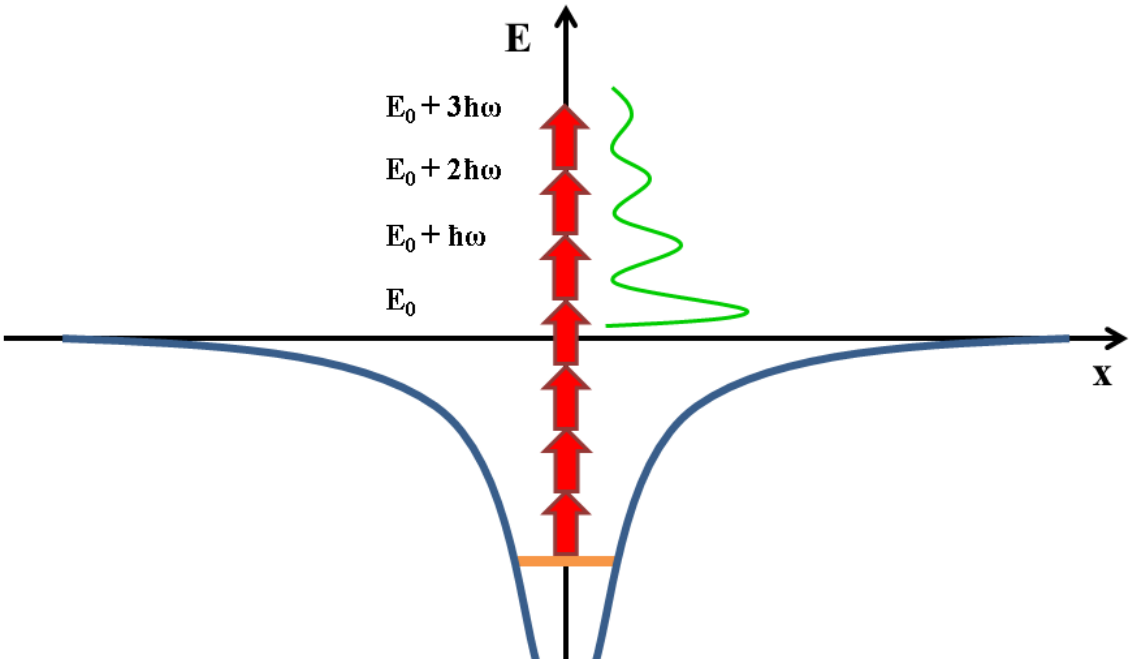

Figure 2.2: Above-Threshold Ionization: In the multi-photon regime, ionization is not restricted to the minimum number of photons required to overcome I_p.

Over-the-Barrier Ionization

In the tunneling ionization regime, the intensity is already high enough to deform the binding potential. If the intensity continues to increase eventually the Coulomb barrier will be suppressed enough such that the electron spills into the continuum. The electron no longer needs to tunnel out. The threshold electric field for OBI is:

$$E_{thresh} = \frac{I_p^2}{4Z} \tag{2.5}$$

where I_p is the ionization potential and Z is the charge of the ion.

It should be noted that although we present the many ionization regimes of strong-field physics as separate, the reality is that there are contributions from all of the regimes for all intensities. The Keldysh parameter is simply a gauge to determine roughly what regime the system is in, or rather which mechanism is contributing the most. Above, we indicate that $\gamma \gg 1$ or $\gamma \ll 1$, but often times, the system is in the grey area of $\gamma \approx 1$. Can multi-photon and tunneling ionization exist at the same time and, if so, what does that mean theoretically?

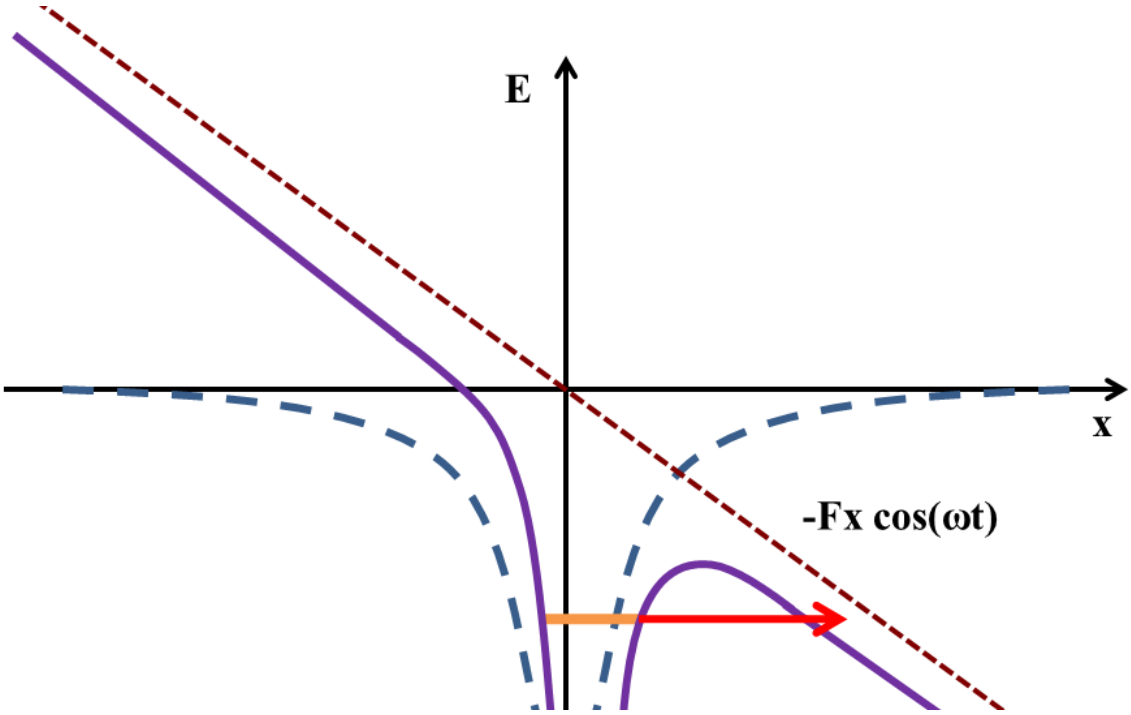

Figure 2.3: Tunneling Ionization: The electric field deforms the binding potential such that the electron can tunnel through the Coulomb barrier.

2.2 Atomic Ionization Models and Theory

In the previous section, 2.1.1, the basic description of the different ionization mechanisms were presented without any indication of where the descriptions came from. In this section, we take a step back to understand the underlying theoretical foundation of current ionization models. First we start with the TDSE and transition into the commonly used strong-field approximation (SFA). In addition, we go into details about some simpler approximations that will be used through out this thesis, such as non-adiabatic tunneling ionization (NTI) and ADK theory. It should be noted that the discussion in this section was heavily influenced by Ivanov *et al.* [50].

2.2.1 Time-dependent Schrödinger Equation

Here, we formally state the time-dependent Schrödinger equation in atomic units:

$$i\frac{\partial}{\partial t}|\Psi\rangle = \hat{H}(t)|\Psi\rangle \tag{2.6}$$

with the solution

$$|\Psi(t)\rangle = e^{-i\int_0^t \hat{H}(t')dt'}|\Psi(t=0)\rangle = e^{-i\int_0^t \hat{H}(t')dt'}|\Phi_i\rangle \tag{2.7}$$

where $\exp[-i\int_0^t \hat{H}(t')dt']$ is the propagator and $|\Phi_i\rangle$ is the initial state at $t = 0$.

We make the substitution of $\hat{H} = \hat{H}_0 + \hat{V}_L(t)$ and arrive at this solution:

$$|\Psi(t)\rangle = -i\int_0^t dt' \left[e^{-i\int_{t'}^t \hat{H}(t'')dt''}\right]\hat{V}_L(t')\left[e^{-i\int_0^{t'} \hat{H}_0(t'')dt''}\right] \times |\Phi_i\rangle + e^{-i\int_0^t \hat{H}_0(t'')dt''}|\Phi_i\rangle \tag{2.8}$$

where $\hat{H}_0$ is the field-free Hamiltonian and, in the length gauge, $\hat{V}_L(t) = -\boldsymbol{dF}(t)$ is the interaction with the laser field. $\boldsymbol{d}$ is the dipole moment of the system and $\boldsymbol{F}$ is the strength of the electric field.

Projecting $|\Psi(t)\rangle$ onto a continuum state, $|\boldsymbol{v}\rangle$, with the assumption that the initial population in the continuum was zero, we get the following amplitude populating the electron velocity $\boldsymbol{v}$:

$$a_{\boldsymbol{v}}(t) = -i\int_0^t dt' |\boldsymbol{v}\rangle \left[e^{-i\int_{t'}^t \hat{H}(t'')dt''}\right]\hat{V}_L(t')\left[e^{-i\int_0^{t'} \hat{H}_0 dt''}\right]|\Phi_i\rangle \tag{2.9}$$

Although a very complicated expression, the solution to the TDSE formally with the above substitutions is a starting point for additional approximations.

2.2.2 Strong-field Approximation and the Non-adiabatic Tunneling Ionization Method

In short, the strong-field approximation (SFA) makes two assumptions, (i) while the electron is bound, it only interacts with the binding potential of the atom (or molecule) and (ii) that once in the continuum, the electron is overwhelmed by the electric-field and no longer feels the

binding potential of the atom (or molecule). The second assumption is realized through the analytic Volkov propagator, $\exp(-i\int_{t'}^{t}\hat{H}_F dt'')$, which is the propagator for the free electron in the laser field. Here, $\hat{H}_F \equiv \hat{H} - \hat{V}_A$ where $\hat{V}_A$ is the field-free binding potential of the system.

We begin the SFA by defining the velocity, $\boldsymbol{v}$, of the free electron in the continuum with initial appearance at t' and velocity $\boldsymbol{v'}$:

$$\boldsymbol{v} = \boldsymbol{v'} + \frac{q}{m}\boldsymbol{A}(t') - \frac{q}{m}\boldsymbol{A}(t) \tag{2.10}$$

where $\boldsymbol{A}(t)$ is the vector-potential of the electric field. q is the electron charge and m is the electron mass which are removed when $q/m = -1$.

We define $\boldsymbol{A}(t)$ from:

$$\boldsymbol{F}(t) = -\frac{\partial \boldsymbol{A}(t)}{\partial t} \tag{2.11}$$

Knowing that the canonical momentum is $\boldsymbol{P} = \boldsymbol{v}(t) - \boldsymbol{A}(t)$, we obtain the instantaneous oscillation energy of the electron:

$$E(t) = \frac{1}{2}(\boldsymbol{v'} - \boldsymbol{A}(t') + \boldsymbol{A}(t))^2 \tag{2.12}$$

Resulting in the Volkov propagator:

$$e^{-i\int_{t'}^{t}\hat{H}_F dt''}|\boldsymbol{v'}\rangle = e^{-i\int_{t'}^{t}E(t'')dt''}|\boldsymbol{v}\rangle \tag{2.13}$$

We now rewrite the amplitude from equation (2.9) in the SFA and relabel it as $\Psi(\boldsymbol{v}, t)$:

$$\Psi(\boldsymbol{v}, t) = -i\int_0^t dt' e^{-i(1/2)\int_{t'}^{t}(\boldsymbol{v'}-\boldsymbol{A}(t')+\boldsymbol{A}(t))^2 dt''}\langle \boldsymbol{v'} + \boldsymbol{A}(t') - \boldsymbol{A}(t)|V_L(t')|g\rangle e^{iI_p t'} \tag{2.14}$$

where $|g\rangle$ is the ground state of the system with energy $-I_p$.

Although the end result of the SFA is much easier to deal with than the formal TDSE,

there are a few issues that arise from the approximations made. Namely, the lack of inclusion of the interaction of the free electron with the atomic binding potential. This causes the ionization rates to be different from their true values. This issue can be mended by comparing the SFA rates in the constant electric field limit and the well known tunneling rates, and then making the appropriate changes to the pre-exponential term in the ionization amplitude. Additionally, the SFA does not account for the ability for the electron to scatter off of the parent ion which would also affect the ionization amplitude. Finally, the SFA is not gauge invariant which means that the theory does not match reality where observable effects do not depend on gauge. Fortunately, these issues affect only the pre-exponential term of the ionization amplitude, therefore, the SFA is considered to have only exponential accuracy.

Non-adiabatic Tunneling Ionization

Now that SFA has been well established, it would be a good opportunity to revisit the question, can multi-photon and tunneling ionization exist at the same time? Earlier in this chapter, we gave the reader a simple picture of what multi-photon ionization is, the absorption of many photons to overcome the binding potential of the atom or molecule, depicted in Fig. 2.1. Another way to look at it would be that as the binding potential oscillates every laser cycle, the electron gains energy as it bounces against the walls of the potential, essentially "heating" up, before it is finally ejected into the continuum, see Fig. 2.4. With tunneling ionization, the potential is distorted every laser cycle such that the electron can tunnel out. However, the motion of the potential must be relatively slow so that the electron has time to tunnel. This is the case for $\gamma \ll 1$, but what happens as γ increases? The electron can tunnel at anytime it is quantum mechanically allowed. What happens if the barrier is changing as the electron is tunneling? The electron will gain energy under the barrier. This is referred to as non-adiabatic tunneling. This is a description of how multi-photon ionization can still occur when tunneling is still allowed. This coexistence between regimes is an important result of the non-adiabatic tunneling ionization theory (NTI) and was outlined by Yudin and Ivanov in ref. [51].

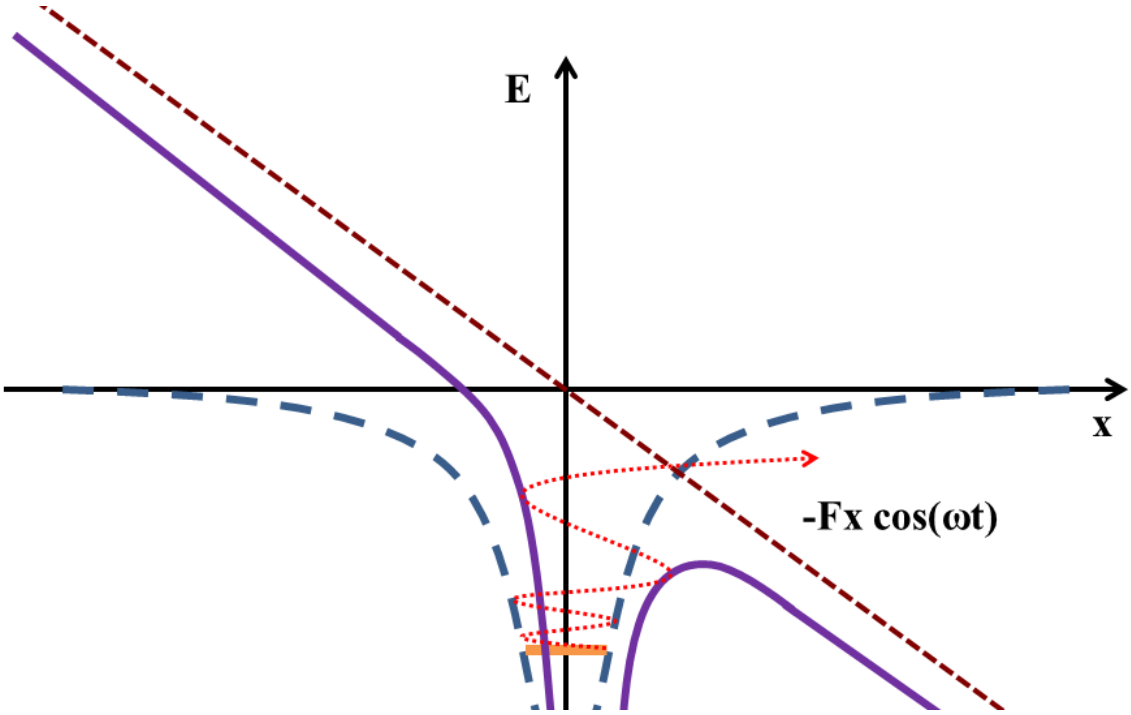

Figure 2.4: Alternative view of Multi-Photon Ionization: The electron is "heated" by the oscillating binding potential of the atom or molecule.

We begin the NTI theory by recalling the ionization amplitude, equation (2.14), from the SFA. If $a_{\boldsymbol{v}}(t) = \Psi(\boldsymbol{v}, t)$, we can write the population of the continuum states at time t as:

$$W(t) = \int d^3\nu |a_{\boldsymbol{v}}(t)|^2 \tag{2.15}$$

Then, using the Dykhne method in references [52, 53], with exponential accuracy:

$$a_{\boldsymbol{v}}(t) \sim \int_{-\infty}^{t} dt' \exp\left(-iS_{\boldsymbol{v}}(t, t')\right) \tag{2.16}$$

and the action integral is:

$$\begin{aligned} S_{\boldsymbol{v}}(t, t') = (I_p + \frac{1}{2}\nu_\perp^2)(t - t') + \frac{1}{2}\int_{t'}^{t} dt''[\nu_\parallel + \nu_0 f(t) \\ \times \sin\phi(t) - \nu_0 f(t'')\sin\phi(t'')]^2 \end{aligned} \tag{2.17}$$

for a linearly polarized laser field, where $\nu_\perp$ and $\nu_\parallel$ are the velocity components perpen-

dicular and parallel to the laser field, $f(t)$ is the field envelope in time, and $\phi(t) = \omega_L t + \varphi_0$ is the instantaneous phase of the linearly polarized laser field, with φ_0 as the absolute carrier phase of the electric field under the envelope.

Through a saddle point analysis detailed in ref. [51], the instantaneous ionization rate with exponential accuracy, for a continuous envelope is:

$$\Gamma(t) \sim \exp\left(-\frac{\mathcal{E}^2 f^2(t)}{\omega_L^3} \Phi(\gamma(t), \theta(t)) \right) \tag{2.18}$$

where $\theta(t) = \phi(t) - \pi k$ is a conveniently defined phase and k is chosen to ensure $-\pi/2 \leq \theta(t) \leq \pi/2$. In addition, γ is the Keldysh parameter, but now relies on the pulse envelope, $\gamma(t) = \gamma / f(t)$. Also:

$$\Phi(\gamma, \theta) = (\gamma^2 + \sin^2\theta + \frac{1}{2}) \ln c - \frac{3\sqrt{b-a}}{2\sqrt{2}} \sin|\theta| - \frac{\sqrt{b+a}}{2\sqrt{2}} \gamma \tag{2.19}$$

$$a = 1 + \gamma^2 - \sin^2\theta \tag{2.20}$$

$$b = \sqrt{a^2 + 4\gamma^2 \sin^2\theta} \tag{2.21}$$

$$c = \sqrt{\left(\sqrt{\frac{b+a}{2}} + \gamma\right)^2 + \left(\sqrt{\frac{b-a}{2}} + \sin|\theta|\right)^2} \tag{2.22}$$

In order to find the ionization rate, to more than just exponential accuracy, the correct pre-exponential term must be used in the expression for the rate:

$$\Gamma(t) = N(t) \exp\left(-\frac{\mathcal{E}^2 f^2(t)}{\omega_L^3} \Phi(\gamma(t), \theta(t)) \right) \tag{2.23}$$

where the pre-exponential term, $N(t)$, originates from the PPT model for ionization (see section 2.2.3) and is defined as:

$$N(t) = A_{n^*,l^*} B_{l,|m|} \left(\frac{3(\ln(\gamma + \sqrt{\gamma^2+1}) - \frac{\gamma}{\sqrt{\gamma^2+1}})}{\gamma^3} \right)^{\frac{1}{2}} C I_p \left(\frac{2(2I_p)^{\frac{3}{2}}}{\mathcal{E} f(t)} \right)^{2n^* - |m| - 1} \tag{2.24}$$

where

$$A_{n^*,l^*} = \frac{2^{2n^*}}{n^* \Gamma(n^* + l^* + 1) \Gamma(n^* - l^*)} \tag{2.25}$$

$$B_{l,|m|} = \frac{(2l+1)(l+|m|)!}{2^{|m|}|m|!(l-|m|)!} \tag{2.26}$$

$$C = (1+\gamma^2)^{\frac{|m|}{2} + \frac{3}{4}} A_m(\omega_L, \gamma) \tag{2.27}$$

and $A_m(\omega_L, \gamma)$ is defined in equations (55) and (56) of ref. [20]:

$$A_m(\omega_L, \gamma) = \frac{4}{\sqrt{3\pi}} \frac{1}{|m|!} \frac{\gamma^2}{1+\gamma^2} \sum_{q \geq_{thr}}^{\infty} A_q(\omega, \gamma) \tag{2.28}$$

$$A_q(\omega, \gamma) = e^{-\alpha(q-\nu)} w_m \left[\sqrt{\beta(q-\nu)} \right] \tag{2.29}$$

$$\nu = \frac{I_p}{\omega} \left(1 + \frac{1}{2\gamma^2} \right) = \frac{I_p + U_p}{\omega} \tag{2.30}$$

$$\alpha(\gamma) = 2 \left[\sinh^{-1} \gamma - \frac{\gamma}{\sqrt{1+\gamma^2}} \right] \tag{2.31}$$

$$\beta(\gamma) = \frac{2\gamma}{\sqrt{1+\gamma^2}} \tag{2.32}$$

$$w_m(x) = \frac{x^{2|m|+1}}{2} \int_0^1 \frac{e^{-x^2 t} t^{|m|}}{\sqrt{1-t}} dt \tag{2.33}$$

The resulting ionization rate, equation (2.23), was used as a key component of the experimental ionization calibration from the strong-field ionization experiments shown in this thesis, chapter 4. Its accuracy is reliable for $\gamma \sim 1$, which is the regime many of the intensity calibration experiments were performed in. As will be mentioned in the following section, we acknowledge that PPT would also serve the same purpose as the NTI model, however, we found that the inclusion of an arbitrary electric field (envelope and phase) in the NTI theory would allow more versatility when comparing the theory to experiment. The results of the FROG measurements (section 3.1.3) for the experimental intensity calibration can be used directly in the theory to generate ionization yields for comparison to experimental yields. The use of NTI in this thesis is explained in better detail in section 4.3.3.

2.2.3 PPT and Cycle-averaged ADK

Shortly after Keldysh's publication which outlined how to determine the ionization rates of atoms and molecules in strong electric fields and ultimately lead to the SFA theory, A. M. Perelomov, V. S. Popov, and M. V. Terent'ev, in 1966, published on the same topic [20]. Their model, now known as the PPT model, was derived for a short-range potential. It also includes long-range Coulomb interaction effects through a first-order correction in the quasiclassical action where only the ground state is considered. It is commonly said that compared to SFA, PPT is a more accurate and versatile model, but technically more complicated.

Without any additional information or derivation besides what has been mentioned previously in this chapter, we present the ionization rate equation from the PPT model:

$$w_{PPT}(F,\omega) = A_{n^*,l^*} B_{l,|m|} I_p \left(\frac{2F_0}{F}\right)^{2n^*-|m|-1} \left(\frac{1}{\sqrt{1+\gamma^2}}\right)^{-|m|-1} A_m(\omega,\gamma) e^{-\frac{2F_0}{3F} g(\gamma)} \tag{2.34}$$

$$g(\gamma) = \frac{3}{2\gamma}\left[\left(1+\frac{1}{2\gamma^2}\right)\sinh^{-1}(\gamma) - \frac{\sqrt{1+\gamma^2}}{2\gamma}\right] \tag{2.35}$$

where A_{n^*,l^*}, $B_{l,|m|}$, and $A_m(\omega,\gamma)$ are defined by equations (2.25), (2.26), and (2.28), respectively. F is the electric field strength and $F_0 = (2I_p)^{\frac{3}{2}}$ is the Coulomb field. Also, q is the number of photons absorbed, n is the principal quantum number, l is the orbital quantum number, m is the magnetic quantum number, $n^* \equiv Z/\sqrt{2I_p}$, and $l^* = n^* - 1$.

ADK Ionization Model

As an extension of the PPT theory, in 1986, Ammosov, Delone, and Krainov published an ionization model [19] that works only in the tunneling regime, $\gamma \ll 1$. It is commonly used by experimentalists for "on-the-fly" calculations when designing and implementing strong-field ionization experiments predominantly in the tunneling regime. Due to its simplicity, the model is easy to use and not computationally costly.

When $\gamma \ll 1$, the following approximations can be made: (i) $\left(1/\sqrt{1+\gamma^2}\right)^{-|m|-1} \approx 1$, (ii) $\sum_{q \geq thr}^{\infty} A_q(\omega,\gamma) \approx 1$, and (iii) $g(\gamma) \approx 1$. From equation (2.34), we can reduce to what is known as the ADK ionization rate:

$$w_{ADK} = |C_{n^*l^*}|^2 G_{lm} I_p \left(\frac{2F_0}{F}\right)^{2n^*-|m|-1} e^{-\frac{2F_0}{3F}} \tag{2.36}$$

Equation (2.36) is only the static electric field ionization rate of the ADK model. In strong-field experiments pulsed AC electric fields are used. In that case, an entire cycle of the field will contribute to the ionization rate and will be significantly smaller than a field of constant strength. The cycle-averaged rate of the ADK ionization model is:

$$\begin{aligned} \bar{w}_{ADK}(F_a) &= \frac{1}{T_0}\int_0^{T_0} w_{ADK}(t)dt \\ &\approx \sqrt{\frac{2}{\pi}}\sqrt{\frac{3F_a}{2F_0}} w_{ADK}(F_a) \end{aligned} \tag{2.37}$$

where T_0 is the time of one period or one cycle of the field and F_a is the amplitude of the field.

It should be stressed once again that the ADK model is only applicable in the tunneling

regime of strong-field ionization. With that said, however, it has been an essential tool in the work shown in this thesis and will be used as an example theory in our experimental intensity calibration method outlined in section 4.3.

2.3 Molecular Ionization Models and Theory

Now that the fundamentals of single electron ionization have been outlined, we turn to more advanced systems, i.e. molecular systems. Even for diatomic molecules, the simplest of molecular systems, the added complexity to the ionization theory is quite significant. The majority of the issues stemming from two things: (i) molecular dynamics and (ii) molecular orbitals. In most cases, the first issue is ignored. Similarly to how the single active electron approximation (SAE) must be used, for single ionization, the time duration for ionization to occur is much shorter than the motion of the molecule. For the second issue, unlike atoms where the ground state orbitals are very well known, molecular orbitals are difficult to approximate and are not spherically symmetric. Even with the use of modern quantum chemistry software (e.g. GAUSSIAN [54] and GAMESS [55]) where molecular orbitals can be calculated to rather high precision with large basis sets, the accuracy of the theories are limited.

As mentioned previously, strong-field molecular ionization theory is a growing topic for many reasons and is essential to the success of future strong-field investigation. In this section, we will outline the current state of molecular ionization theory, focusing mainly on the theories used to complement the experiments shown in this thesis, and comment on where the theory is headed in the future.

2.3.1 Current Molecular Ionization Models

Subsequently, we describe, briefly, the underlying assumptions and results of the molecular orbital (MO) -ADK, MO-PPT, and MO-SFA strong-field molecular ionization models.

Molecular Orbital SFA

A detailed description of the strong-field approximation was given in section 2.2.2 for the case of atoms. The end result of that discussion was the rewriting of the population amplitude of the electron velocity, equation (2.9), as equation (2.14) under the assumptions of the SFA. Mainly, the interaction of the electron with the binding potential is only present when the electron is bound and, also, the electron only feels the electric-field of the laser while in the continuum, approximated by a Volkov state. For the molecular case, the approach is the same. Using ref. [56, 57] as a guide, the amplitude for a transition from a bound state $\Phi_0(r)$ to continuum is given by:

$$f(\boldsymbol{p}) = i\int_{-\infty}^{\infty} dt \langle \boldsymbol{p} + \boldsymbol{A}(t)|\boldsymbol{r}\cdot\boldsymbol{E}(t)|\boldsymbol{\Psi}_0\rangle \exp[-iS(\boldsymbol{p},t)] \tag{2.38}$$

where

$$S(\boldsymbol{p},t) = \int_{t}^{\infty} dt' \left\{ \frac{[\boldsymbol{p}+\boldsymbol{A}(t')]^2}{2} + I_p \right\} \tag{2.39}$$

with $\boldsymbol{p}$ as the momentum of the emitted electron, I_p is the ionization potential, and $\boldsymbol{A(t)}$ is the vector potential. The bound state wave functions are calculated using quantum chemistry packages, such as GAUSSIAN or GAMESS.

The Volkov state used, as per one of the SFA approximations, is:

$$\langle|\boldsymbol{p}+\boldsymbol{A}(t)\rangle = \frac{1}{(2\pi)^{\frac{3}{2}}} e^{[\boldsymbol{p}+\boldsymbol{A}(t)]\cdot\boldsymbol{r}} \tag{2.40}$$

As was realized in the atomic discussion of the SFA, the calculation is not always straightforward. Next we introduce MO-ADK and MO-PPT as computationally simpler molecular ionization models, where species dependent parameters are often tabulated for ease-of-use.

Molecular Orbital ADK and PPT

In the spirit of the atomic ADK tunneling ionization model, see section 2.2.3, where atoms are considered to be hydrogen-like, with atom specific modifications, a molecular ionization

theory was created, termed molecular orbital ADK (MO-ADK) theory, which takes the assumptions of the atomic ADK model and is modified to account for electronic wave function differences between atoms and molecules. This model is considered approachable in terms of ease-of-use, but as a result, it also lacks the inclusion of more complex phenomena, such as many-electron effects.

The MO-ADK model was detailed in Tong *et al.* [34] for linear molecules. In atomic units, the asymptotic wavefunction of the valence electron at large distances is:

$$\Psi^m(\boldsymbol{r}) = \sum_l C_l F_l(r) Y_{lm}(\hat{\boldsymbol{r}}) \tag{2.41}$$

with m as the magnetic quantum number along the molecular axis. C_l is normalized such that:

$$F_l(r \to \infty) \approx r^{z_c/\kappa - 1} e^{-\kappa r} \tag{2.42}$$

with Z_c as the effective Coulomb charge and $\kappa = \sqrt{2I_p}$.

The leading term of the spherical harmonic along the molecular axis, assuming field direction along the same axis, is:

$$Y_{lm}(\hat{\boldsymbol{r}}) \simeq Q(l,m) \frac{1}{2^{|m|}|m|} \sin^{|m|}\theta \frac{e^{im\phi}}{\sqrt{2\pi}} \tag{2.43}$$

where

$$Q(l,m) = (-1)^m \sqrt{\frac{(2l+1)(l+|m|)}{2(l-|m|)}} \tag{2.44}$$

Therefore, equation (2.41) can be rewritten for the tunneling region:

$$\begin{aligned} \Psi^m(\boldsymbol{r}) &\simeq C_l Y_{lm}(\hat{\boldsymbol{r}}) r^{z_c/\kappa - 1} e^{-\kappa r} \\ &\simeq B(m) r^{z_c/\kappa - 1} e^{-\kappa r} \frac{1}{2^{|m|}|m|} \sin^{|m|}\theta \frac{e^{im\phi}}{\sqrt{2\pi}} \end{aligned} \tag{2.45}$$

with

$$B(m) = \sum_l C_l Q(l,m) \tag{2.46}$$

The static field tunneling ionization rate then becomes:

$$w_{stat,MO-ADK}(F,0) = \frac{B^2(m)}{2^{|m|}|m|}\frac{1}{\kappa^{2Z_c/\kappa-1}}\left(\frac{2\kappa^3}{F}\right)^{2Z_c/\kappa-|m|-1} e^{-2\kappa^3/3F} \tag{2.47}$$

where F is the peak field strength.

In the case of a nonlinear molecule at an arbitrary angle $\boldsymbol{R}$ with respect to the field direction, $B(m)$ is replaced with:

$$B(m') = \sum_{lm} C_{lm} D^l_{m',m}(\boldsymbol{R}) Q(l,m') \tag{2.48}$$

where $D^l_{m',m}(\boldsymbol{R})$ is the Wigner rotation matrix and $\boldsymbol{R}$ is the Euler angles between the molecular axis and the field direction.

This results in the static field tunneling ionization rate:

$$w_{stat,MO-ADK}(F,\boldsymbol{R}) = \sum_{m'} \frac{B^2(m')}{2^{|m'|}|m'|}\frac{1}{\kappa^{2Z_c/\kappa-1}}\left(\frac{2\kappa^3}{F}\right)^{2Z_c/\kappa-|m'|-1} e^{-2\kappa^3/3F} \tag{2.49}$$

and the cycle-averaged ionization rate is:

$$w_{MO-ADK}(F,\boldsymbol{R}) = \left(\frac{3F}{\pi\kappa^3}\right)^{\frac{1}{2}} w_{stat}(F,\boldsymbol{R}) \tag{2.50}$$

The C_{lm} coefficients can be found tabulated in the literature. The wavefunctions used in the MO-ADK method can be determined from the quantum chemistry packages, however, in general, sufficiently accurate wavefunctions are required in the asymptotic region and therefore, caution should be taken. Ill-behaved or small basis set calculated wavefunctions can introduce error into the ionization rate calculation.

Mentioned many times, the ADK method is designed to work in the tunneling regime only, $\gamma \ll 1$. As was the case with the atomic case, the PPT ionization model was able

to handle a broader range of γ. In a similar style as MO-ADK, the molecular orbital PPT (MO-PPT) model modifies the existing atomic PPT model to account for the structure parameters of a molecule. Using ref. [35, 39, 40], the cycle-averaged ionization rate is:

$$w_{MO-PPT}(F,\omega,\boldsymbol{R}) = \left(\frac{3F}{\pi\kappa^3}\right)^{\frac{1}{2}} \sum_{m'} \frac{B^2(m')}{2^{|m'|}|m'|} \frac{A_{m'}(\omega,\gamma)}{\kappa^{2Z_c/\kappa-1}} (1+\gamma^2)^{|m'|/2+3/4} \times \left(\frac{2\kappa^3}{F}\right)^{2Z_c/\kappa-|m'|-1} e^{-(2\kappa^3/3F)g(\gamma)} \tag{2.51}$$

where γ is the Keldysh parameter, ω is the angular frequency of the laser pulse, $g(\gamma)$ is the same as equation (2.35), $B(m')$ is the same as equation (2.48), and $A_{m'}(\omega,\gamma)$ is the same as equation (2.28). Although the MO-PPT model is able to accommodate a broader range of γ, the same issues with the approximated wavefunctions that was cautioned about with MO-ADK exist.

As a final note, the equations for molecular ionization rates stated above are angle dependent with respect to the ionizing laser field. Depending on the experiment, either measurements on aligned molecules or randomly oriented molecules are performed. In the experiments presented in this thesis, the molecules studied are all randomly oriented. The calculated ionization rates must be averaged over all possible angles in order to have a fair comparison of theory and experiment.

2.4 Translating Theoretical Rates to Yields for Experimental Comparison

Thus far, we have presented three different practical approaches to calculating the ionization rates for atoms and molecules in the presence of a strong electric field: SFA, PPT, and ADK. The final result of all of those models is the rate. Experimentally speaking, the ionization rate is not measured. Instead, the ionization yield is measured. In this section, we present the necessary steps to determine the theoretical ionization yields based on the calculated

ionization rates.

2.4.1 Ionization Probability and Volume Averaging

The Probability of Ionization

In the simplest example, the ionization rate indicates how quickly the initial population of neutral atoms will be depleted through ionization assuming the only mechanism available is single ionization. In that case, the probability of ionization is:

$$p(I) = 1 - \exp\left(- \int_{-\infty}^{\infty} w(F) dt \right) \tag{2.52}$$

where w is any of the rates mentioned earlier, such as equations (2.37), (2.34), (2.50), and (2.51).

In a more formal description, following ref. [58], we consider the possibility of multiply ionized systems where ionization occurs sequentially. In the following, Γ is now the rate coefficient for generality. The rate equations for an n times ionized atom or molecule are:

$$\begin{aligned}
\frac{dp_0}{dt} &= -\Gamma_0 p_0, \\
\frac{dp_1}{dt} &= -\Gamma_1 p_1 + \Gamma_0 p_0, \\
\frac{dp_2}{dt} &= -\Gamma_2 p_2 + \Gamma_1 p_1, \\
&\dots \\
\frac{dp_n}{dt} &= \Gamma_{n-1} p_{n-1}
\end{aligned} \tag{2.53}$$

where p_n is the probability that the target is n times ionized.

The solutions to the rate equations in equation (2.53) are:

$$
\begin{aligned}
p_0(t) &= \exp[-\phi_0(t)], \\
p_1(t) &= \exp[-\phi_1(t)] \int_{-\infty}^{t} \exp[\phi_1(s)]\Gamma_0(s)p_0(s)ds, \\
p_2(t) &= \exp[-\phi_2(t)] \int_{-\infty}^{t} \exp[\phi_2(s)]\Gamma_1(s)p_1(s)ds, \\
&\dots \\
p_{n-1}(t) &= \exp[-\phi_{n-1}(t)] \int_{-\infty}^{t} \exp[\phi_{n-1}(s)]\Gamma_{n-2}(s)p_{n-2}(s)ds, \\
p_n(t) &= \int_{-\infty}^{t} \Gamma_{n-1}(s)p_{n-1}(s)ds
\end{aligned}
\tag{2.54}
$$

where

$$
\phi_k(t) = \int_{-\infty}^{t} \Gamma_k(t')dt' \tag{2.55}
$$

In order to make the calculations simpler, we consider the decaying edge of the lower charge state probability to be sufficient to use. Therefore, p_{n-1} can be replaced with $\exp(-\phi_{n-1})$ in equation (2.54). This yields:

$$
\begin{aligned}
p_0(t) &= \exp[-\phi_0(t)], \\
p_1(t) &= \exp[-\phi_1(t)] \int_{-\infty}^{t} \exp[\phi_1(s)]\Gamma_0(s)\exp[-\phi_0(s)]ds, \\
p_2(t) &\approx \exp[-\phi_2(t)] \int_{-\infty}^{t} \exp[\phi_2(s)]\Gamma_1(s)\exp[-\phi_1(s)]ds, \\
&\dots \\
p_{n-1}(t) &\approx \exp[-\phi_{n-1}(t)] \int_{-\infty}^{t} \exp[\phi_{n-1}(s)]\Gamma_{n-2}(s)\exp[-\phi_{n-2}(s)]ds, \\
p_n(t) &\approx \int_{-\infty}^{t} \Gamma_{n-1}(s)\exp[-\phi_{n-1}(s)]ds
\end{aligned}
\tag{2.56}
$$

Equation (2.56) is not to be used with an arbitrary laser pulse, however, for narrow laser pulses, such as the femtosecond pulses used throughout this thesis, the approximation for the ionization probability at $t = \infty$ is:

$$
\begin{aligned}
&p_0(\infty) = \exp(-\phi_0), \\
&p_1(\infty) \approx \phi_0 \frac{\exp(-\phi_0) - \exp(-\phi_1)}{\phi_1 - \phi_0}, \\
&p_2(\infty) \approx \phi_1 \frac{\exp(-\phi_1) - \exp(-\phi_2)}{\phi_2 - \phi_1}, \\
&\dots \\
&p_{n-1}(\infty) \approx \phi_{n-2} \frac{\exp(-\phi_{n-2}) - \exp(-\phi_{n-1})}{\phi_{n-1} - \phi_{n-2}}, \\
&p_n(\infty) \approx 1 - \exp(-\phi_{n-1})
\end{aligned}
\tag{2.57}
$$

Volume Averaging

Thus far, we presented the theoretical models as ionization from single peak intensity laser pulses at a single point in space. However, in an actual experiment, the target sample is a collection of atoms or molecules within the volume of the laser focus. The intensity as a function of position is not constant and, therefore, the probability of ionization will be different throughout the volume of the laser beam. The ionization yield measured in an experiment is the total ion output of the target sample after laser electric-field interaction. That total is a sum from all points in space. In order to approximate the ionization yield of an experiment, the probability of ionization must be calculated and summed over the entire focal volume. This is referred to as volume averaging.

For a Gaussian beam with peak intensity of I_0, the volume of the focusing beam can be written in terms of the isointensity boundary for I as:

$$
V = \frac{\pi^2 \omega_0^4}{\lambda} \left[\frac{2}{9} \left(\frac{I_0}{I} - 1 \right)^{\frac{3}{2}} + \frac{4}{3} \left(\frac{I_0}{I} - 1 \right)^{\frac{1}{2}} - \frac{4}{3} \arctan \left(\frac{I_0}{I} - 1 \right)^{\frac{1}{2}} \right] \tag{2.58}
$$

where λ is the central wavelength of the laser and ω_0 is the beam radius.

The ionization yield of an $n+1$ ion is calculated by:

$$
N_{n+1} = \rho \int_0^{I_0} \frac{dV}{dI} p_{n+1} dI \tag{2.59}
$$

where ρ is the density of the target sample and p_{n+1} is the probability of ionization of

an $n+1$ ion calculated using equation (2.57). For completeness, the derivative of equation (2.58) with respect to intensity is:

$$\frac{dV}{dI} = \frac{\pi z_0 \omega_0^2}{3} \frac{2I + I_0}{I^2} \left(\frac{I_0 - I}{I} \right)^{\frac{1}{2}} \tag{2.60}$$

The basic idea of modifying theoretical ionization rate calculations to account for experimental actualities was laid out in this subsection. A real example of how the ionization models and yield calculations, including volume averaging, are used to compliment and better understand experimental results can be found in chapter 4.

2.5 Summary

In this chapter we introduced the fundamentals of strong-field ionization. Through the use of the Keldysh parameter, γ, the different types of SFI regimes are identified, such as the multi-photon and the tunneling ionization regimes. Over-all, however, the typical working regime we find ourselves in is $\gamma \sim 1$ where MPI and TI coexist. We also gave a brief overview of the current state of both atomic and molecular strong-field ionization theory. After starting with the solution to the TDSE, we moved onto more computationally friendly methods, such as the SFA, PPT, and ADK ionization models. Through the exploration of those approaches, we gained insight into when certain models are appropriate to use and what the limitations of each model are. Also, once the appropriate theoretical ionization model is chosen, the ionization rates can be converted to ionization yields and used to aid with the understanding of experimental results, chapter 5, or used to perform calibrations, chapter 4.

In the following chapters, the focus will shift to a more experimental approach to studying the strong-field single ionization of molecules. We encourage the reader to make note of the fundamentals of strong-field ionization and the possible ionization models as they will only aid in the understanding of the observed strong-field phenomena presented in this thesis.

Chapter 3

Experimental Techniques

In this chapter we introduce the various light sources used in the experiments presented in later chapters of this thesis. We begin the chapter with a description of an intense pulsed laser system, the titanium doped sapphire (Ti:sapphire) femtosecond laser. Although considered the "work horse" of the ultra-fast community, the particular system used in our experiments has a very high pulse energy output used to pump an optical parametric amplifier (OPA) which in turn also has a very high energy output. We then describe a device used to measure and characterize the laser pulses produced by these ultra-fast light sources.

We also describe the spectrometer used to detect and quantify the amount of particular charged particles emitted during the strong-field ionization process in the experiments presented in later chapters of this thesis and the underlying fundamentals of how the apparatus works. In addition, we describe our ability to perform single-shot measurements.

3.1 Light Sources and Pulse Characterization

3.1.1 High Intensity Tunable Source

The High Intensity Tunable Source (HITS), Fig. 3.1, is a commercially purchased titanium doped sapphire (Ti:sapphire) femtosecond laser system. HITS is capable of producing pulses with a center wavelength of ~ 790 nm and a bandwidth (FWHM) of ~ 50 nm , corresponding

to a fourier transform limited (FTL) Gaussian pulse duration (FWHM of the intensity) of about 25 fs. The system runs at a repetition rate of 1 kHz with a maximum energy-per-pulse of 20 mJ [59].

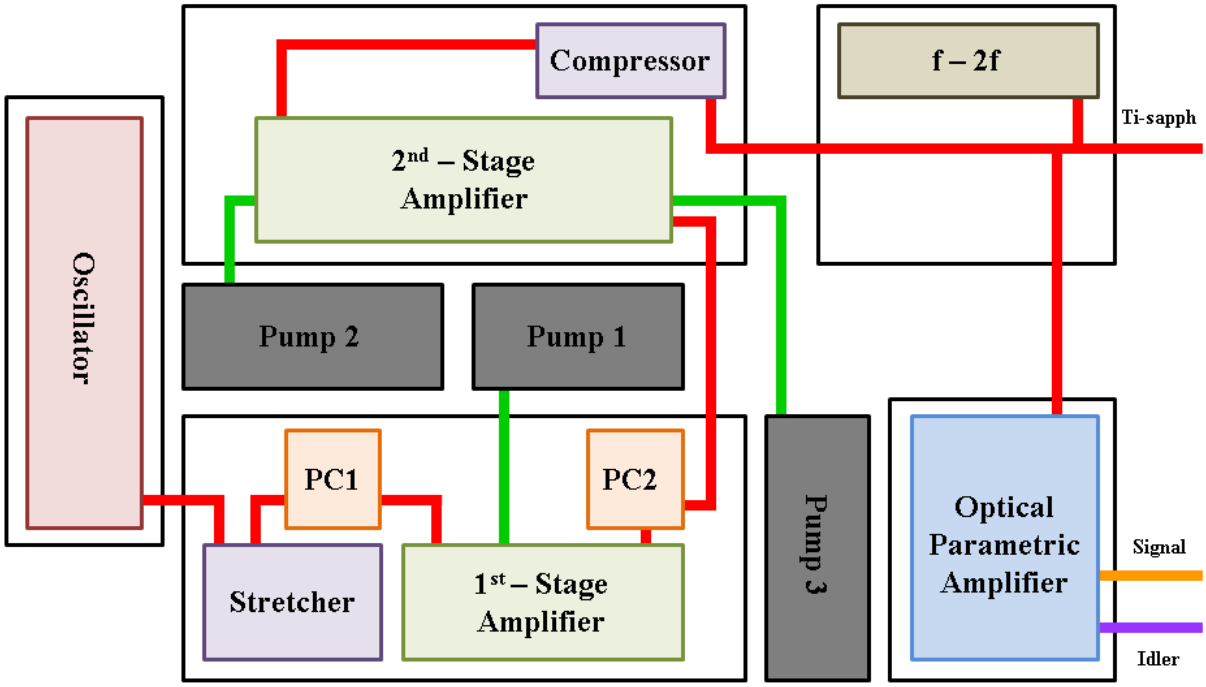

Figure 3.1: The basic layout of the HITS laser, a 2-stage, chirped pulse amplified, cryo-cooled, Ti:sapphire laser. Output: 790 nm center wavelength, 50 nm bandwidth, 25 fs FWHM pulse duration, 1 kHz repetition rate, and 20 mJ energy-per-pulse.

The laser system starts with a mode locked Ti:sapphire oscillator which produces pulses with a central wavelength of about 790 nm and runs with a repetition rate of 80 MHz. The resulting laser pulses have a bandwidth (FWHM) in the range of 65 - 80 nm which corresponds to an FTL pulse duration (FWHM) of about 14 - 11 fs, respectively. With an output of 5 nJ (400 mW), the laser pulses under go a process called chirped pulse amplification [6]. The pulses are stretched to roughly 100 picosecond time durations using optical gratings (stretcher) and then go through a Pockels cell where a pulse is "picked" once every millisecond (1 kHz). Pockels cells are essentially voltage controlled waveplates. By applying a high voltage to a crystal lacking inversion symmetry, birefringence is induced and can be used to change the polarization of a laser pulse. A pulse can be selected by using a polarization dependent filter to choose only the pulses with the polarization induced by the Pockels

cell. The pulses are then amplified by passing through a cold helium cryo-cooled Ti:sapphire crystal pumped with a single frequency doubled diode-pumped-solid-state (DPSS) laser (532 nm, nanosecond pulsed) with a maximum output of 35 W (Photonics Industries, model DM-30). The amplification is accomplished with 13 passes through the crystal in a "ring-type" configuration. The final pass exits the ring and goes through a second Pockels cell for "pulse cleaning". This is necessary due to the production of amplified spontaneous emission (ASE) in the amplifier crystal from the pump lasers. Although ASE is minimized with proper alignment of the amplification stage, the Pockels cell helps to remove this incoherent and undesired light. Next, the laser pulses are transported to a second amplification stage where again they pass (5 passes, "bow tie-type") through a cryo-cooled Ti:sapphire crystal pumped with two counter propagating DPSS lasers (532 nm, nanosecond pulsed) each with a maximum output of 50 W (Photonics Industries, model DM-50). The fully amplified laser pulses (29 mJ, 29 W) are subsequently expanded to a Gaussian beam profile of about 22 mm ($1/e^2$ of the intensity) and compressed back to a 25 fs pulse duration with the use of a grating pair (compressor). The final maximum output is approximately 20 mJ, (20 W). A basic diagram of the layout of HITS is shown in Fig. 3.1.

HITS is able to operate continuously for days at a time with very little maintenance. The long term stability of the laser, typically $\leq 1\%$ power fluctuation over 5 hours, was essential for the experiments presented in this thesis.

3.1.2 Optical Parametric Amplifier

18 of the 20 mJ output of HITS can be diverted into a commercially produced, high energy white light seeded optical parametric amplifier (OPA), an HE-TOPAS by Light Conversion.

Optical parametric generation (OPG), also known as spontaneous parametric down-conversion, is defined as the conversion of a photon with frequency ω_1 to two additional lower energy photons with frequency ω_2 and ω_3 through a $\chi^{(2)}$ nonlinear medium. Since energy must be conserved, $\omega_1 = \omega_2 + \omega_3$. In the context of an OPA, ω_1 is the pump, ω_P, and the two outputs are the signal, ω_S, and idler, ω_I. Conventionally, the signal is higher

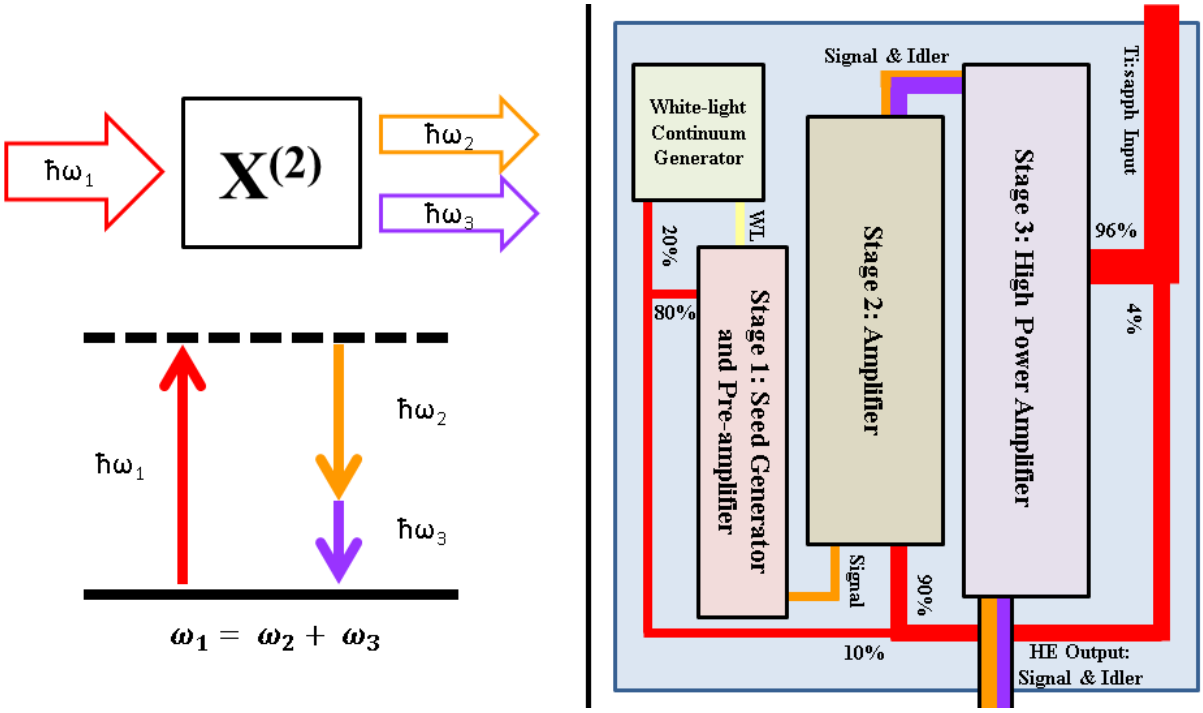

Figure 3.2: (left) Diagram illustrating the conversion of a photon with frequency ω_1 to two additional lower energy photons with frequency ω_2 and ω_3 through a $\chi^{(2)}$ nonlinear medium, known as optical parametric generation. (right) Basic layout of the HITS OPA, a high energy white light seeded optical parametric amplifier. Tunable output: 1150 - 1600 nm signal (1600 - 2600 nm idler) center wavelength with 6 mJ total (signal + idler) output energy-per-pulse.

frequency than the idler, $\omega_S > \omega_I$. A diagram illustrating OPG is shown on the left half of Fig. 3.2.

The HITS OPA utilizes the idea of OPG to convert the high energy, femtosecond output of the HITS laser into the wavelength range 1150 - 2600 nm. This is accomplished through three different amplification stages. A diagram showing the basic layout of the HITS OPA is shown in the right half of Fig. 3.2. 18 mJ of the HITS laser output is put into the OPA. 0.4% of that input is used in the first stage of the OPA, the seed generator and preamplifier. A portion of the light sent into the first stage is focused into a sapphire plate and white-light continuum (WLC) is generated. The WLC output is then mixed with the other portion of the Ti:sapphire input (pump) into the first stage. The mixing is done in a type II β - barium borate (BBO) crystal. The crystal is oriented in such a way that it is most efficient for the target signal wavelength. This is what gives the OPA its wavelength tunability. The now

preamplified signal is the seed for the next stage.

In the second stage, the preamplified seed of signal radiation is amplified to tens of μJ using the same OPG process as before where now 3.6% of the original Ti:sapphire input is used as a pump to be mixed in a BBO crystal with the signal seed. Finally the third stage is called the high power (energy) amplifier. It utilizes the remaining pump energy (96% of the original Ti:sapphire input) and mixes with the seed from the second stage in yet another BBO cyrstal. The amplification brings the signal to mJ levels and, as a biproduct, an idler of similar energy output is also generated. For greatest efficiency, the OPA signal and idler outputs should propagate collinearly. Note, however, in the experiment conducted in chapter 6, the OPA was intentionally aligned in a non-collinear configuration in order to separate signal and idler in the far field and circumvent the use of filtering optics.

The fully amplified output consists of two pulses of perpendicular polarization, the signal (1150 - 1600 nm) and the idler (1600 - 2600 nm) with a maximum total combined (signal + idler) output of about 6 mJ (6 W). The total output is variable depending on the wavelength settings. For this system, the crystals are most efficient when tuned for 1300 nm signal (2000 nm idler) resulting in a 2:1 total output ratio favoring the signal. The resulting pulses at the output of the OPA for the signal have a bandwidth (FWHM) of $\sim$ 71 nm with a corresponding pulse duration (FWHM) of 35 fs. For the idler, the bandwidth (FWHM) is $\sim$ 147 nm with a corresponding pulse duration (FWHM) of 40 fs.

Note that the FTL pulses occur at the output of the OPA, but in the experiments presented in this thesis, FTL pulses were unable to be maintained due to induced group velocity dispersion. Unlike the 790 nm output of HITS where the compressor gives an ability to compensate for linear chirp obtained through propagation, the OPA has no such feature. For the greatest efficiency, the final amplification through the final crystal is performed such that the 790 nm light is FTL in the final amplification crystal. The resulting OPA pulses are consequently also approximately FTL at the output, but quickly pickup linear chirp through propagation of air and other optical elements. Propagation through bulk materials, such as UV fused silica, GaAs, etc. can be used to compensate for induced phase. Of course, the dispersion properties are wavelength dependent so which material is used and how much of

it, will depend on the tuned state of the OPA.

3.1.3 Frequency Resolved Optical Gating (FROG)

In ultrafast experiments, the femtosecond laser pulses used are too short in time to be measured/characterized by electronic means, such as a photodiode, which has nanosecond to picosecond response times. Instead, the laser pulses must be measured using a process that can respond on the same time scales of the pulses, such as a self-gated nonlinear process in a crystal.

Frequency resolved optical gating (FROG) [60–62] is a pulse characterisation technique that is basically a spectrally resolved autocorrelation or cross-correlation. For the purposes of this thesis, we will keep the discussion focused only on the second harmonic generation (SHG) FROG. The reader should be aware, however, that there are many types of FROG techniques available which can be more applicable depending on the experiment being performed.

Autocorrelation is performed by overlapping, in space, a pulse and a copy of that pulse in a SHG crystal, usually non-collinearly. Additionally, the two pulses are delayed in time with respect to one another. The frequency doubled output due to the momentum conservation, the sum of the k-vectors of the two input beams results in a measurable signal that is delay dependent. The nonlinear output is typically measured with a photodiode and integrated. The intensity autocorrelation is defined as:

$$A^2(\tau) \equiv \int_{-\infty}^{\infty} I(t)I(t-\tau)dt \tag{3.1}$$

where $I(t)$ is the intensity of the original pulse and $I(t-\tau)$ is the intensity of the delayed pulse by some amount τ. In the standard example of a gaussian pulse, the intensity autocorrelation signal's FWHM width, $\Delta\tau_A^{FWHM}$, is related to the FWHM width of the input pulse intensity, $\Delta\tau_{pulse}^{FWHM}$, by $\Delta\tau_A^{FWHM} = 1.41\Delta\tau_{pulse}^{FWHM}$. Note there are two problems with autocorrelation. The first is that the signal is always symmetric, meaning the direction of the pulse is indiscernible and second, the pulse envelope is determined, but there is no information related to the phase. The solution to the second problem is to include spectral

information.

The jump from autocorrelation to SHG-FROG is simple, the photodiode is now replaced with a spectrometer. Instead of measuring the intensity signal of the nonlinear output as a function of delay, now a spectrum is measured as a function of delay. This results in a spectrogram, see Fig. 3.3(c), which is defined as:

$$I_{FROG}(\omega,\tau) = \left| \int_{-\infty}^{\infty} E_{sig}(t,\tau) e^{-i\omega t} dt \right|^2 \tag{3.2}$$

where $E_{sig}(t,\tau) = E(t)E(t-\tau)$ for SHG-FROG and τ is the delay between pulses. A visualization of the basic layout of a FROG is shown in Fig. 3.3(a). A depiction of E_{sig} is shown in Fig. 3.3(b).

Additionally, given:

$$E_{sig}(t,\tau) = \int_{-\infty}^{\infty} \hat{E}_{sig}(t,\Omega) e^{-j\Omega\tau} d\Omega \tag{3.3}$$

implying:

$$I_{FROG}(\omega,\tau) = \left| \int_{-\infty}^{\infty}\int_{-\infty}^{\infty} \hat{E}_{sig}(t,\Omega) e^{-i\omega t - j\Omega\tau} dt d\Omega \right|^2 \tag{3.4}$$

Inverting equation (3.4) is known as the 2D-phase retrieval problem. The solution can be obtained iteratively by providing an initial guess for $E(t)$ and generating $E_{sig}(t,\tau)$. The guess is transformed into the frequency domain and an intensity constraint is imposed by using $I_{FROG}(\omega,\tau)$ before being transformed back into the time domain. A new estimate for $E(t)$ is generated. The process continues until the rms error between the measured and calculated FROG traces is minimized to an acceptable level. More information of the FROG inversion algorithm can be found in refs. [62–64].

The speed at which a solution is determined is entirely based on how good of a guess can be generated per iteration of the algorithm. One of the most robust and successful additions to the FROG inversion algorithm is the method of generalized projections [63] where two sets of pulses are found and the solution is the intersection of the two sets. On each iteration, the

sets are alternated between minimizing the distance between the two sets, until a solution converges. One set is all $E_{sig}(t,\tau)$ satisfying the nonlinear material response and the other is the set of all complex functions with a magnitude $I_{FROG}(\omega,\tau)$.

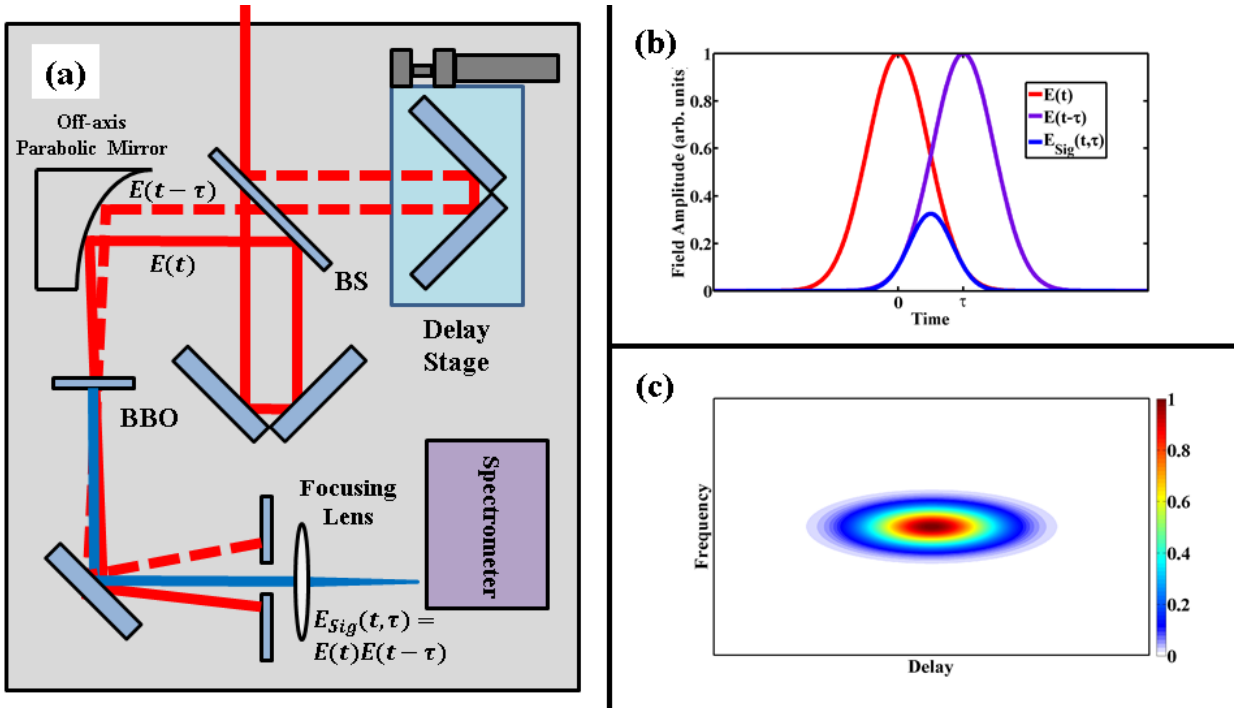

Figure 3.3: (a) A diagram showing the basic layout of the HITS FROG, a SHG-type pulse characterization device with the ability to measure and characterize femtosecond laser pulses with center wavelengths of 700 - 2600 nm and pulse durations as short as 20 fs. Visualization of the (b) overlap of two laser pulses of an SHG FROG and (c) an example spectrogram.

All laser pulses used in the experiments in this thesis were measured and characterized with a home-built FROG that has the ability to measure pulses with center wavelengths of 700 - 2600 nm and pulse durations as short as 20 fs. Credit for the construction of the FROG is given to S. Zigo, D. Wilson, X. Ren, and C. Trallero-Herrero. As seen in Fig 3.3(a), the input beam is separated into two different paths with a beam splitter designed for the center wavelength of the pulse being measured. In order for the original pulse and its copy to completely overlap in time, the two beam paths must be the same exact length. The path for the transmissive beam has a fixed length and the path for the reflected beam has a linear translation stage with 0.5 μm precision. This allows for the FROG measurement to have delay steps in time of about 1.33 fs. Since the fundamental idea behind the FROG is

to self reference, the optical paths are designed such that each arm of the FROG has the same amount of optical material as the other. To be more precise, each beam interacts with the beam splitter twice, once reflecting/transmitting and then vice versa before focusing onto a 10μm type-I barium borate (BBO) crystal for second harmonic generation (SHG). The focusing is performed with an off-axis parabolic mirror (f = 15 cm) and the beams are aligned such that they focus non-collinearly in the crystal. This allows for the separation of the input beams and the nonlinear output without the use of filtering optics. The crystal is thin enough such that phase matching remains acceptable without co-propagating beams.

The nonlinear output from the crystal, is coupled into a commercially purchased fiber optic spectrometer. A spectrum is saved for every delay step in order to build the necessary spectrogram. The main advantage of the home-built device is its adaptability to a large range of spectral wavelengths that are encountered in our experiments. For example, the 790 nm pulses are measured with a different spectrometer than the NIR idler pulses (2000+ nm) produced by the OPA. The resulting spectrograms are run through a pulse retrieval software (FROG 3.2.2 by Femtosoft Technologies 2006) which reconstructs the measured pulses completely and provides both the temporal and spectral pulse information, characterized by both phase and amplitude.

3.1.4 Carrier Envelope Phase Stabilization and Locking

Another important feature of HITS is its ability to stabilize and lock the carrier envelope phase (CEP) of the laser pulses it produces. Consequently, the OPA output is also CEP stable. Although this feature was never utilized in the main experiments presented in this thesis, future experiments will rely on it. A detailed description of what CEP is, how it is locked, and how stabilizing it will benefit future experiments is located in section 8.3.

3.2 Experimental Apparatus

3.2.1 Time-of-Flight Mass Spectroscopy

We have performed experiments using an ion time-of-flight mass spectrometer (TOFMS). A diagram of a basic TOFMS is shown in Fig. 3.4. The light is focused into the chamber using a plano-convex lens and ions are created in a homogeneous gas sample. The ions are repelled toward a micro-channel plate (MCP) detector and guided by an electrostatic lens system before traveling in a field-free drift tube. See Fig 3.4 for a basic layout of a TOFMS. With a background base pressure of $\approx 10^{-9}$ torr, the chamber is flooded with a particular species, in vapor form, to high pressures within the safe operating conditions of the MCP (about 10^{-6} to 10^{-5} torr). When detected, the ion signal is amplified by the MCP and converted into a time-dependent voltage which is detected using a fast oscilloscope (see section 3.2.2). Each ion has a unique arrival time dependent on its mass and charge:

$$t \propto \sqrt{\frac{m}{q}} \tag{3.5}$$

where t is the arrival time of the ion to the MCP, m is the species mass, and q is the atomic charge of the ion.

The resulting ion spectrum, an example of which is shown in Fig. 3.5, consists of structured peaks corresponding to positively charged atoms, molecules, or fragment molecules. Although most ionization occurs along the laser polarization axis, at the time of creation of the ions, there is a spread of velocity initial conditions resulting in an inherent temporal width at detection. The voltages on the electrostatic lenses can be tuned such that the best possible temporal resolution is achieved. The pressure of the chamber is also set low enough to avoid temporal broadening due to space charge effects and detector saturation. By gating around the arrival time of the species of interest and integrating the signal, the relative ionization yield is obtained.

Additional information regarding specific experimental details and the use of the TOFMS are presented in chapters 4, 5, and 6 for better clarity.

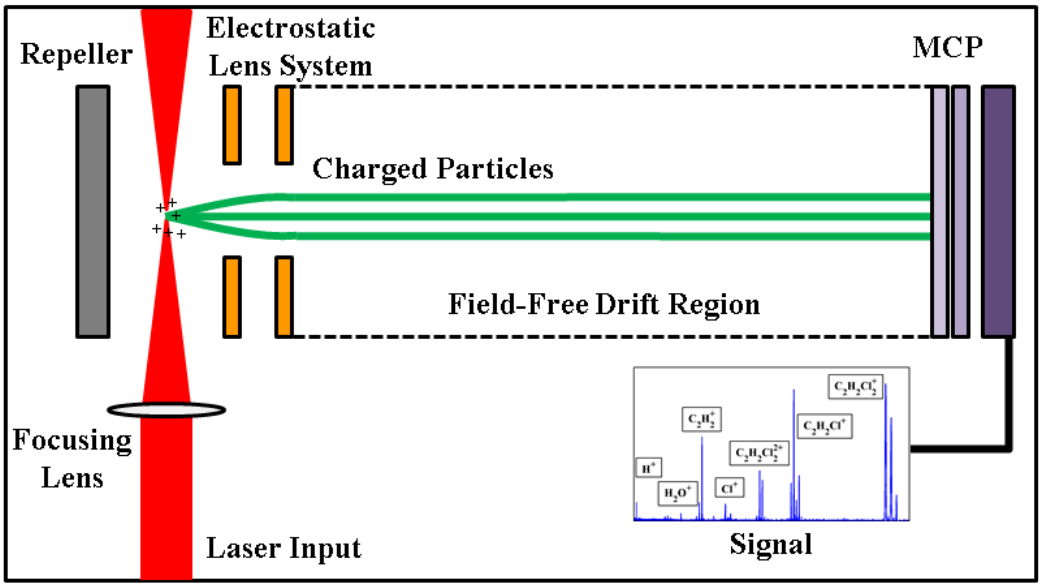

Figure 3.4: A basic layout of a time-of-flight mass spectrometer. After ionization, charged particles are guided via an electrostatic lens system to an MCP detector and converted to a time-dependent voltage.

3.2.2 Single-shot Measurements and Analysis

As described earlier, our strong-field ionization experiments are performed using intense pulsed lasers which operate with a 1 kHz repetition rate. Having the ability to make measurements and record data at the repetition rate of the laser has many advantages both during the experiment and for the post-analysis process. In the following subsections, we explain what was used to make "single-shot" measurements and detail what advantages transpire from making them.

Digitizing the Detector Signal

In the ion-TOF experiments, when an ion impacts the surface of the MCP detector, a cascade of electrons is produced resulting in a brief, but measurable current. This single event can be read as a time-dependent voltage, Gaussian-like and on the order of 1 ns in width. Although the MCP has a detection resolution on the order of 100 picoseconds, the

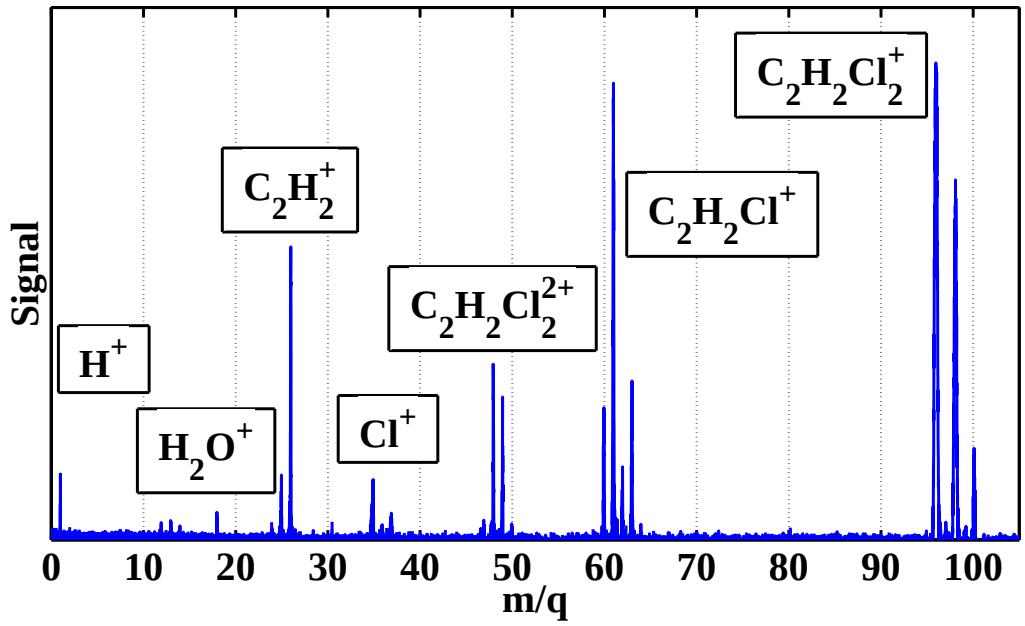

Figure 3.5: An example of an ion time-of-flight spectrum for $C_2H_2Cl_2$. Parent ion m/q values are 96, 98, and 100 due to the two naturally occurring isotopes of chlorine (35 and 37).

single event, nanosecond bin limitation is purely electronic.

There are two common ways to digitize the signal produced by the detected charged particles. One is to use a time-to-digital converter (TDC) which is a device that converts the gaussian-like events into TTL standard pulses for cleaner particle counting. The fast operation repetition rates of the TDC allow for single particle detection with resolution down to the 10's of picoseconds. The main limitation of the TDC is its limited dynamic range. In addition, although the single particle time resolution is excellent, the TDC is unable to differentiate between events that happen simultaneously. Additional information about TDC's and greater detail about their use will be explained in section 7.2.

The second way to digitize the signal is with an analog-to-digital converter. For our experiments, we use a fast digital storage oscilloscope with a sampling rate of 1 Gsample/sec. This corresponds to a minimum time resolution of 1 ns. An oscilloscope differs from a TDC in the sense that it is representing the signal as is, limited by the sampling resolution. With the oscilloscope, we sacrifice time resolution and counting speed for increased voltage resolution. This, in effect, increases our dynamic range and allows us to account for the

occurrence of simultaneous events, realized in an increase in event signal amplitude. In our experiments, this means we can accurately report the ionization yields at higher intensities where a greater number of events per laser shot might occur. Of course, the dynamic range is still limited by detector saturation, the inability for a detector to recover fast enough to register additional particle impacts. Note, however, there should be little difference between the two digitizers in the low intensity regime where count rates are less than one count per laser shot. Additional details about the particular oscilloscopes used in our experiments will be provided in later chapters of this thesis.

In both detection methods, we are able to perform measurements on a "single-shot" basis, meaning we have the ability to record the yield of the detected particles for every single laser pulse without the need to average over many laser pulses. The main advantage to this ability is to be able to determine the statistical error of the measurement much more accurately. In addition, when using the oscilloscope, which is the device used for all of our strong-field experiments, we found that by recording each laser pulse's total raw TOF spectrum we had the most flexibility in post-analysis. By having access to the raw signal, we are able to pinpoint experimental hindrances, such as stray-particle induced background, electronic background signal noise, and time-dependent influences, e.g. pressure and intensity fluctuations. In averaged measurements, time-dependent issues become transparent and can no longer be accounted for correctly in the analysis.

Intensity "Tagging" and Discrimination

In section 2.2, a mathematical description of the intensity dependence of the strong-field ionization yield is shown. In general, strong-field ionization yields are extremely nonlinear as a function of laser intensity. This means that small changes in the intensity can have drastic effects on the measured total average yield of a particular species.

Recall that the laser intensity is directly proportional to the energy of the laser pulse. In our experiments, we monitor the pulse energy with a photodiode since the integrated photodiode signal is proportional to the pulse energy. Using the second channel of our oscilloscope,

we simultaneously record the photodiode signal and the raw TOF signal for every single laser pulse without having to worry about synchronization issues between devices. Each integrated photodiode signal value obtained corresponds to a raw TOF spectrum causing the data to be what we call intensity "tagged".

There are two things that make intensity "tagging" not only beneficial, but essential in most strong-field ionization experiments. The first of which is it can be used as a diagnostic tool both during and after an experiment. For example, if the ionization yields do not follow similar trends as the laser intensity as a function of time, then there might be unresolved experimental issues.

The second use is a process known as intensity discrimination and rebinning. We define discrimination as the removal of a data point whose corresponding intensity is significantly different than that of the intensity mean. In the case of a stable laser with energy fluctuations $< 2\%$, intensity discrimination is almost unnecessary, however, it does protect against brief energy surges in the laser output or simply mistriggering of the electronics. On the other hand, in the case of a less stable laser with energy fluctuations $> 2\%$, intensity discrimination would be wasteful and most likely hurt the overall statistical error of the measurement. When an expected intensity range can no longer be maintained for long periods of time, and intensities are measured on a shot-to-shot basis, the data can be redistributed to be associated with its appropriate intensity range based on the measurement. This is called intensity rebinning.

As an example, we simulate the laser behavior of a typical experiment, see Fig. 3.6. Given a laser with $\sim 1\%$ shot-to-shot noise, we perform an experiment where the intensity of the light is changed by 4% every 2500 laser shots, see Fig. 3.6(a). This is an ideal situation and a histogram of the intensity points, Fig. 3.6(b), clearly shows that the data has roughly normal distributions at four different intensity mean values (90, 94, 98, and 102).

We repeat the simulation, but now, we add a slow intensity drift with maximum deviation of $\sim 10\%$. Shown in Fig. 3.6(c). If we approached the analysis the same as in the ideal case, the statistics would be very poor and the data would not even fall into the bounds of the previously assigned intensity bins centered around the four intensity mean values. Instead,

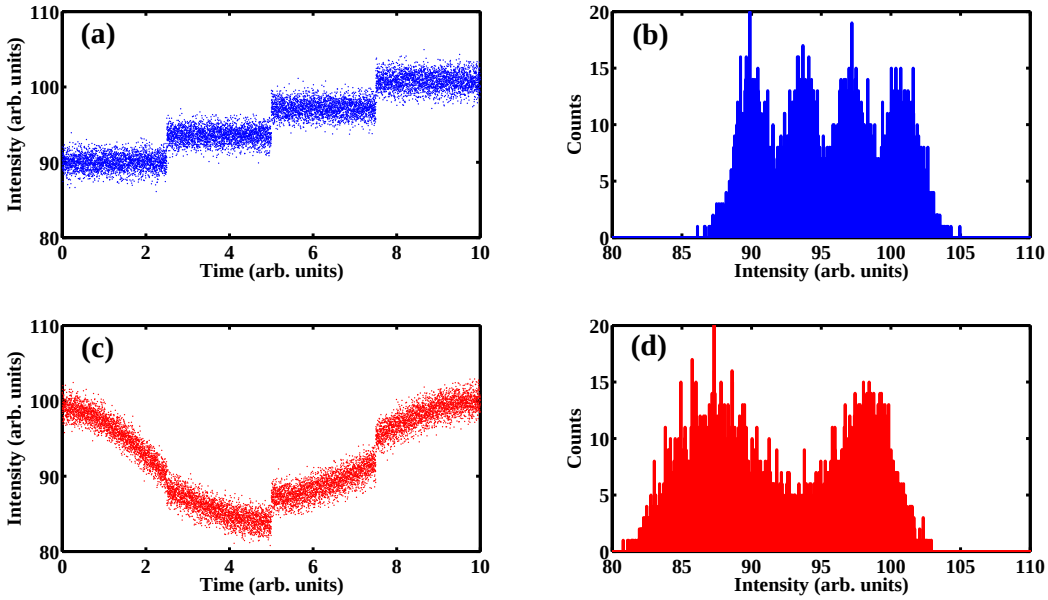

Figure 3.6: A simulation example of how intensity rebinning is utilized in an experiment: (a) Ideal case, (b) Histogram of the ideal case, (c) Slow intensity drift with time case, and (d) Histogram of intensity drift case.

since we have single-shot information, the data can be redistributed to fit into new intensity bins with better statistics centered around new intensity mean values. In Fig. 3.6(d), it is clear that there are two new normal-like distributions of intensity points with mean intensity values at roughly 88 and 98. Additional details and information unique to each experiment regarding intensity discrimination and rebinning can be found in later chapters of this thesis.

Pressure Monitoring and Correction

To account for additional experimental fluctuations, we monitor and correct for pressure variations, so that each yield is considered pressure (density) independent. For our experiments, which can have data acquisition times on the order of hours, we found that the pressure would drift over time. The pressure measurement itself is not performed at a single-shot rate because the change in pressure is very slow compared to the repetition rate of the laser, therefore, we take a pressure reading every 400 - 4000 laser shots. A Bayard-Alpert ionization gauge (BAG), a hot-cathode type gauge, and a Granville-Phillips 330 Ionization Gauge

Controller with an accuracy of 3% are used. The gauge provides a current proportional to the absolute pressure. The absolute pressure is determined by:

$$P = \frac{I_c}{S_{N_2} R_g I_e} \tag{3.6}$$

where I_c is the ion current, S_{N_2} is the sensitivity factor for N_2, I_e is the electron current, and R_g is the relative sensitivity factor. R_g is based on the electron scattering cross section of the particular species. In the experiments presented in this thesis, R_g for the samples used are not available. However, for impact electrons in the range of 50 - 150 eV, we argue no experimental data shows that for each isomeric pair, defined in sections 5.2.3 and 6.2.2, the cross section is nearly identical. Our assumption is based on reported studies of comparative cross sections for different molecular isomers in the same energy range [65–67]. Taking all these factors into consideration we assume that the pressure measurements for each pair are calibrated within 10% or less.

3.3 Summary

In this chapter we introduced the intense pulsed lasers used in the strong-field ionization experiments presented in this thesis. Although the exact conditions of the light sources used for each experiment will be given in greater detail in later chapters, we encourage the reader to keep the basic characteristics of the lasers in mind as they continue through this thesis.

We also gave a brief overview of experimental apparatus used to perform the strong-field ionization experiments presented in this thesis. We hope that the reader has gained a base understanding of how ion yield measurements are made and how the use of fast measurement techniques allow for a deeper understanding of the measurement. A common theme throughout this thesis, at least from an experimental point of view, is the benefits of keeping track of experimentally variable parameters, such as chamber pressure and laser intensity, and understanding the influence they can have on the experimental results if not monitored closely and accounted for.

In the next chapter, we will stress the importance of intensity in all strong-field ionization studies and why it is imperative to accurately determine the intensity used in our experiments. We will also introduce a method for mapping our integrated photodiode values to laser peak intensities.

Chapter 4

Intensity Calibration

We commence this chapter with a brief overview of gaussian optics and define what is actually meant when we refer to intensity in a focused laser beam. We then outline one of the most common ways to measure intensity experimentally, spot-size measurement, and the main shortcomings of that particular method. In order to reduce the error of an intensity measurement for each experiment, we introduce a different method where we calibrate the intensity via ionization. We end the chapter with a practical example of the intensity calibration to show how the method can be used as a tool to illuminate possible experimental and theoretical issues.

4.1 Understanding Intensity

As alluded to in previous chapters, the intensity is one of the most important parameters in strong-field physics. Defined as the power transferred per unit area, commonly with units W/cm^2 in strong-field physics, the intensity of the field is often times the most tunable variable in a laboratory setting. Intensity is linked to the electric field strength.

Taking a look at the fundamentals of gaussian optics, we define the beam radius at any point along z:

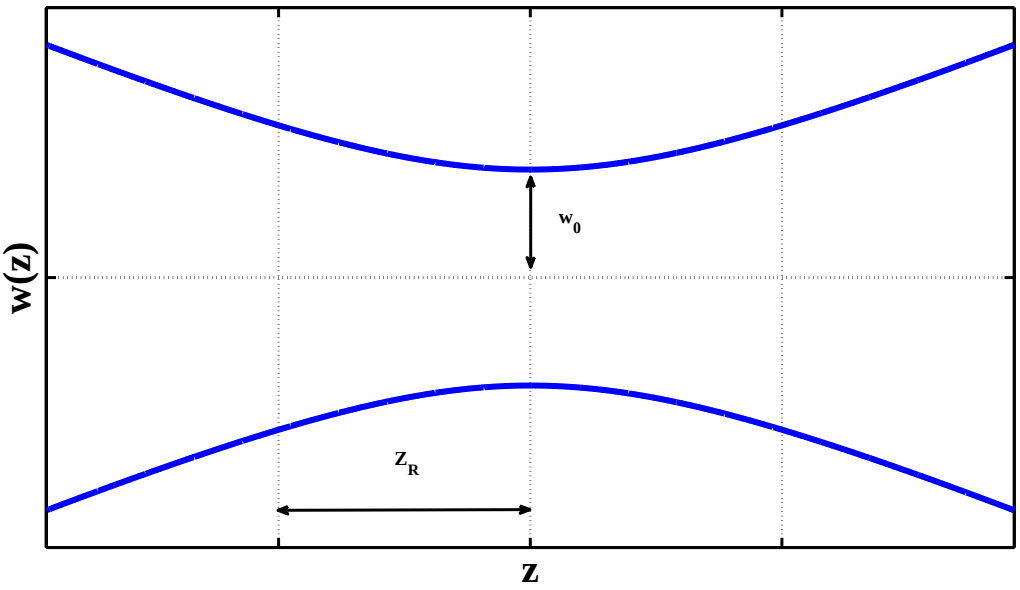

Figure 4.1: A visualization of a gaussian beam: Beam radius as a function position, indicating the minimum beam waist radius, w_0, and the Rayleigh range, z_R.

$$w(z) = w_0\sqrt{1 + \left(\frac{z}{z_R}\right)^2} \tag{4.1}$$

where w_0 is the minimum beam waist radius ($1/e^2$) and z_R is the Rayleigh range defined as $z_R = \frac{\pi w_0^2}{\lambda}$ and λ is the center wavelength of the laser.

Assuming a symmetric beam along the z-axis, the intensity of a gaussian beam is:

$$I(r, z, t) = I_0 \exp\left[- \frac{r^2}{w_0^2[1 + (\frac{z}{z_R})^2]} - \frac{4 \ln 2 t^2}{\tau_{FWHM}^2} \right] \tag{4.2}$$

where z is the propagation axis, r is the radial axis, t is time, τ_{FWHM} is the laser FWHM pulse duration, and I_0 is the laser peak intensity at the focus of the beam. For a gaussian beam:

$$I_0 = \frac{4E_0}{\pi w_0^2 \tau_{FWHM}} \sqrt{\frac{\ln 2}{\pi}} \tag{4.3}$$

where E_0 is the pulse energy of the light.

Although, for an experiment, it is often times sufficient to simply identify the intensity

used as the peak intensity at the focus of the laser beam, I_0, the fact that the intensity can be different at different locations of the focal volume (equation (4.2)) can have effects on the physical outcome of a measurement and must be considered when applicable. In section 4.3.1, the reader will see that in strong-field ionization experiments, the contribution from the entire focal volume can significantly influence the measured ionization yield.

4.2 Measuring Intensity: Spot-Size Measurement Method

In this section, we outline a common form of intensity measurement used in many experiments involving lasers. Recall from the previous section, the peak intensity of a gaussian beam depends mainly on three parameters inherent to the laser pulse characteristics and focusing conditions of the beam: the pulse energy, E_0, the pulse duration, τ_{FWHM} , and the minimum beam waist w_0. As described in section 3.2.2, the pulse energy can be determined by monitoring the laser output with a power meter or a calibrated photodiode. In the case of single shot analysis with a photodiode, the statistical error of the measurement is on the order of a couple percent for a stable laser. The pulse duration measurement is performed with a FROG and was described in section 3.1.3. If performed properly, the typical error of a FROG measurement for nearly FTL pulses is on the order of a femtosecond. The only remaining parameter is the beam waist which can be determined through a method known as a spot-size measurement.

4.2.1 Determining the Minimum Beam Waist

Experimentally we extract the beam waist of the focusing gaussian beam by imaging the beam profile along the propagation axis of the light. The logical question to ask is why not simply image the beam exactly at the focus and report the minimum beam waist from that measurement? Unfortunately, for most affordable low-noise scientific grade cameras, the minimum pixel size is on the order of 2-3 μm. This gives rise to the possibility of a large amount of error (on the order of 50%) in the measurement since it is common to have beam

waists on the order of 10 - 20 μm in strong-field experiments.

In order to reduce the error and have a more successful measurement, the beam must be imaged through the entire Rayleigh range of the beam, along the propagation, z, axis, see Fig 4.1. Since we are restricting ourselves to gaussian profiles, each image is fit to a gaussian function in both transverse, x and y, axes. Each spot-size as a function of z, $w(z)$, is extracted from the FWHM of the fit. For each transverse axis, we fit the extracted spot-sizes to equation (4.1) using a least-squares fitting to determine the appropriate minimum beam waist, w_0.

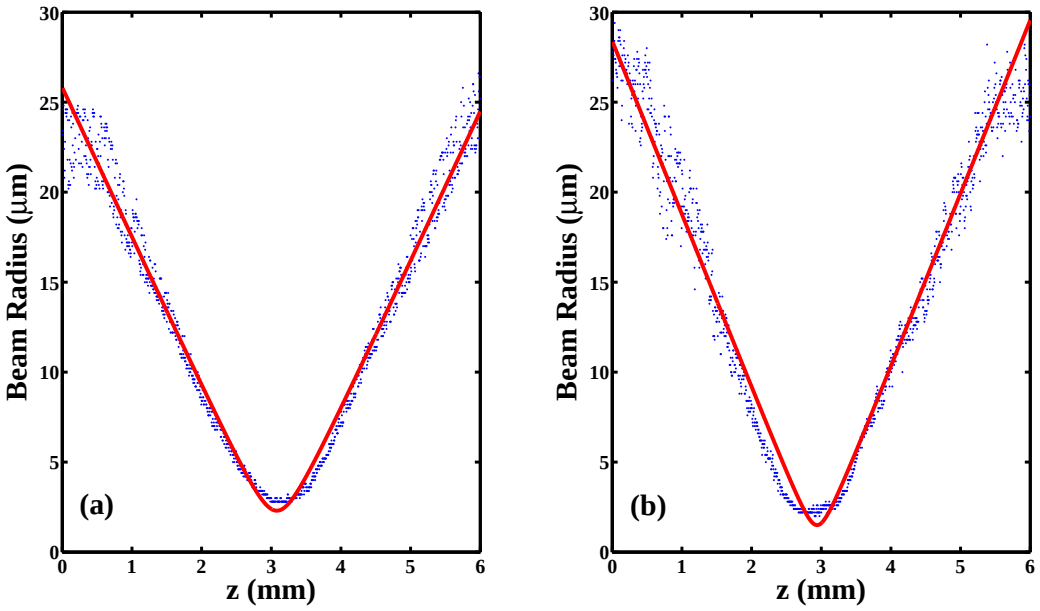

Figure 4.2: An example of a spot-size measurement, w_0. The one dimensional beam profile of a focusing gaussian beam is visualized as w_0 as a function of the propagation distance, z.

As an example, we show the results of a spot-size measurement in Fig 4.2. The laser parameters are similar to those described in chapter 5, 790 nm center wavelength, 1.5 cm input diameter, and 15 cm focusing lens. A low-noise CMOS camera (Mightex SME-B050-U) with pixel size 2.2 μm was used with an automatic linear translation stage (minimum step size of 1 μm) to image the beam profile along the propagation axis. Through the fitting procedure, a beam waist of 2.3 μm was found for the x-axis (4.2(a)) and 1.5 μm for the y-axis (4.2(b)).

Through this example, we highlight some of the shortcomings of the spot-size measurement method for ultimately determining the intensity used in an experiment. The main limitation of the measurement is the physical pixel size of the camera detector, however, limited dynamic range also plays a role. As is shown in Fig. 4.2, near the minimum of the beam profile in both x- and y-axis, the values become more uniform as a result of the minimum pixel resolution of the camera. Related to that issue is the fitting procedure for the theoretical beam profile and which points should be used. The smaller beam radii are limited by the camera resolution and larger radii are limited by the noise of the camera detector. This causes the measurement to be unreliable. Finally, the spot size measurement is an external measurement, the meaning of which will be introduced in the following section.

4.3 Measuring Intensity: Ionization Measurement Method

In the previous section, we outlined a common method for determining the peak intensity of a focused laser beam in an experiment. It was pointed out in that section that one of the contributions to error in the measurement was the fact that it is an external measurement, meaning the spot-size measurement is technically made under different conditions than the actual experiment and outside of the vacuum chamber, quite literally. In this section, however, we outline a different method for determining the intensity used in an experiment and consider it to be superior to the spot-size method. This different method uses ionization yield measurements of noble gases and the well-known theoretical yields as a function of pulse energy to determine the intensity used in an experiment. The measurement is being performed internally, inside of the vacuum chamber, under the same conditions as the experiment and using the same equipment. It is important to note that we do not claim that calibrating intensity based on ionization is a "brand new" method. In fact, the basic idea we are about to present is similar to the one presented in [68], but in a full gaussian volume, where the ion yield from a calibration gas as a function of pulse energy is fit to theory. In addition, however, through the intensity calibration procedure, we introduce ways to gain insight about the ionization experiments being performed through the fitting analysis between

experiment and theory.

4.3.1 Experimental and Theoretical Ionization Yields

As discussed in section 2.2, the strong-field ionization of atoms is relatively well understood. The easiest atoms to work with and often times the most studied are the chemically inert noble gases. Our goal is to measure the ionization yield of the parent ion of one of the noble gases as a function of laser pulse energy and compare it to the trusted theoretical yields as a function of intensity, thereby finding a factor to convert the measured pulse energy in an experiment to an intensity. As described in section 3.2.1, the yields of the atomic ions are measured using a TOFMS. The energy per pulse is systematically varied and data is collected over a large range of intensities. How this is accomplished will be left for explanation in sections 5.2.2 and 6.2.1. In order to execute a successful comparison to theory, it should be noted that the experimental data cannot cover a "featureless" range of intensities. In other words, the intensity range must contain data points in both the multi-photon regime and the tunneling regime so that a change in slope in log scale can be observed as a function of intensity. As discussed in section 3.2.2, the pulse energy is monitored and accounted for on a shot-to-shot basis.

Theoretical atomic ionization rates are determined using a method developed by Yudin and Ivanov [51] termed nonadiabatic tunnel ionization theory (NTI), see section 2.2.2 for additional details. In this case, NTI ionization rates are superior to other commonly used theoretical methods, such as the ADK (Ammosov-Delone-Krainov) model [19] because the calibration is over an intensity range that covers both the multi-photon and tunneling regimes. We comment that we choose to use the NTI theory for its ease of implementation and acknowledge that there are other equally valid and proven methods available, such as the original Perelomov-Popov-Terent'ev (PPT) theory [20–22] and the improved PPT model [23] as shown in [40].

Since our ultimate goal is to compare the theoretical calculations to the experimentally determined yields, some experimental actualities must be accounted for, such as laser pulse

parameters and intensity volume effects. The NTI theory requires knowledge of a fully characterized laser pulse as it takes into account the electric field phase and amplitude in determining the ionization rates. Experimentally, the laser pulse output is characterized by the FROG technique, as described in section 3.1.3 and can directly be used in the theory.

We now outline what is meant by intensity volume effects. Consider the following scenario: say one is given a fixed density of atoms that are exposed to laser radiation with a single intensity and in a fixed volume. The atoms ionize at a particular ionization rate which increases as the intensity increases. Eventually, the intensity will be great enough such that all of the atoms singly ionize each time they are exposed to the radiation. Now we allow the probability that the atoms will doubly ionize after a particular intensity threshold is met. As that probability increases, the number of 2nd ions will increase and the number of first ions will decrease since they are now becoming 2nd ions. This discussion can continue for higher and higher charge states, until the atom is completely stripped of its electrons.

Mathematically, as described in section 2.4.1, the probability of ionization is determined by:

$$\begin{aligned}
&p_0(\infty) = \exp(-\phi_0), \\
&p_1(\infty) \approx \phi_0 \frac{\exp(-\phi_0) - \exp(-\phi_1)}{\phi_1 - \phi_0}, \\
&p_2(\infty) \approx \phi_1 \frac{\exp(-\phi_1) - \exp(-\phi_2)}{\phi_2 - \phi_1}, \\
&\dots \\
&p_{k-1}(\infty) \approx \phi_{k-2} \frac{\exp(-\phi_{k-2}) - \exp(-\phi_{k-1})}{\phi_{k-1} - \phi_{k-2}}, \\
&p_k(\infty) \approx 1 - \exp(-\phi_{k-1})
\end{aligned} \tag{4.4}$$

with

$$\phi_k(t) = \int_{-\infty}^{t} \Gamma_k(t')dt' \tag{4.5}$$

where k is the charge state of the atom, and $\Gamma_k(t)$ is the instantaneous ionization rate at time t. Equation (4.4) was derived from the rate equations for sequential ionization and

is outlined in detail in ref. [58] and section 2.4.1. It should be noted that the ionization rates determined via the NTI theory only took into account ionization up to the 2nd charged state.

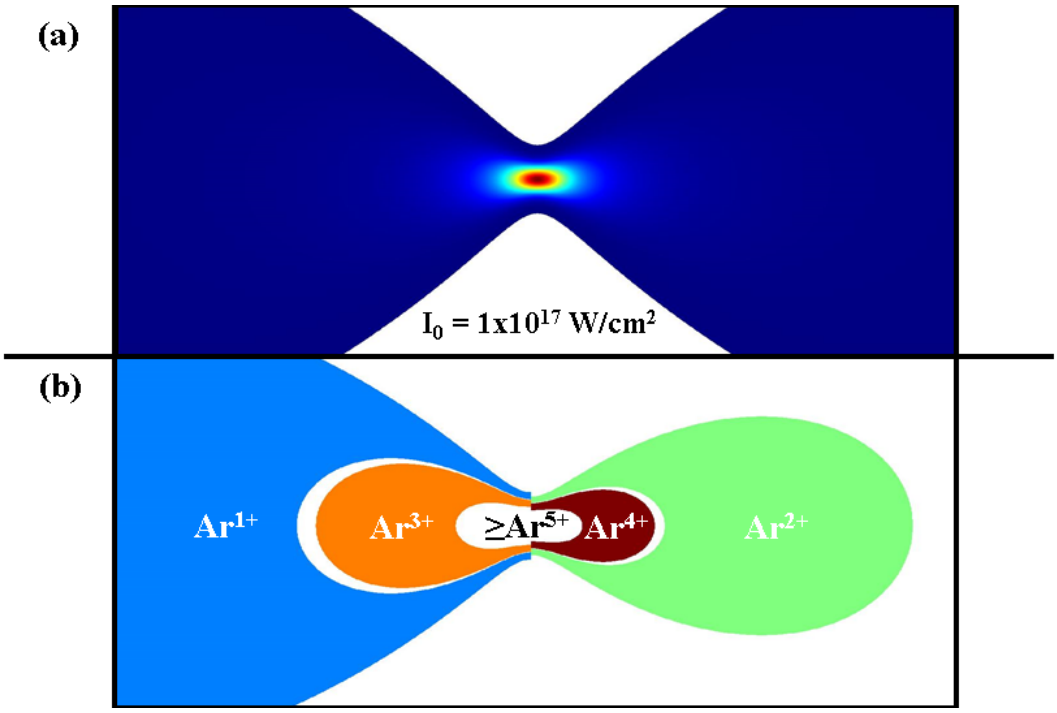

Figure 4.3: A cartoon visualizing how different ions can be created in different parts of a focusing beam due to the nonuniform intensity distribution: (a) A gaussian beam profile with $I_0 = 10^{17} W/cm^2$ (blue = min, red = max), and (b) Ionization volumes bounded by intensity contours related to threshold and saturation intensity values for each ion of argon. Even and odd charge states are separated for visual clarity; however, in actuality, the bounded regions overlap with each other and appear on both sides of the laser focus.

As described earlier in this chapter, the intensity of a focused gaussian beam is not uniform throughout the volume profile of the beam. In fact, as the energy per pulse increases, the intensity profile also changes. Knowing the threshold intensities of the ions being calculated, we can map where in the focus particular ions can originate from. Fig. 4.3, shows a cartoon of such a mapping. The volume of the focused beam can effectively be described in terms of intensity. Although ionization saturation can still occur in the central part of the focus, where high intensities are located, new ions can still be made in the wings of the focus, where intensities are lower. The ionization yield of the first ion will always increase in this scenario even though yield continues to be lost to higher charge states. This phenomenon

is considered an intensity volume effect and in the ionization theory, when the entire focal volume is taken into account over all intensities up to the peak intensity, it is considered volume averaging.

For the theoretical calculations we follow ref. [58] and the equation for the focal volume of a gaussian beam was found in refs. [27, 69]. Again, the difference is that we use the NTI rates. The theoretical ionization yield is:

$$N_{thry}(I_0) = \rho \int_0^{I_0} \frac{dV}{dI} p dI \tag{4.6}$$

and

$$\frac{dV}{dI} = \frac{\pi z_0 \omega_0^2}{3} \frac{2I + I_0}{I^2} \left(\frac{I_0 - I}{I} \right)^{\frac{1}{2}} \tag{4.7}$$

where N_{thry} is the theoretical ionization yield, ρ is the sample density, p is the probability of ionization, V is the focal volume, I is the intensity, I_0 is the peak intensity of the pulse, z_0 is the Rayleigh range, and ω_0 is the focal spot size.

The theoretical model produces the yield, $N_{thry}(I_0)$, as a function of peak laser intensity, I_0, which is then fit to the experimentally measured yield, $N_{exp}(E_{exp})$, as a function of pulse energy, E_{exp}. Since we care only about relative yields, and are interested in calibrating our energy into peak intensity, the actual fitting is done between the functions $N_{exp}(\alpha E_{exp})$ and cN_{thry}, where α is the energy-intensity calibration constant and c is a normalization parameter for the theoretical yield. An example of a completed intensity calibration is shown in Fig.4.4 with theoretical yield calculations using both the NTI and ADK methods. The NTI model result is considered the best calibration, however, the use of two different ionization models will be described in section 4.3.3. Details of the fitting procedure are given in the next subsection.

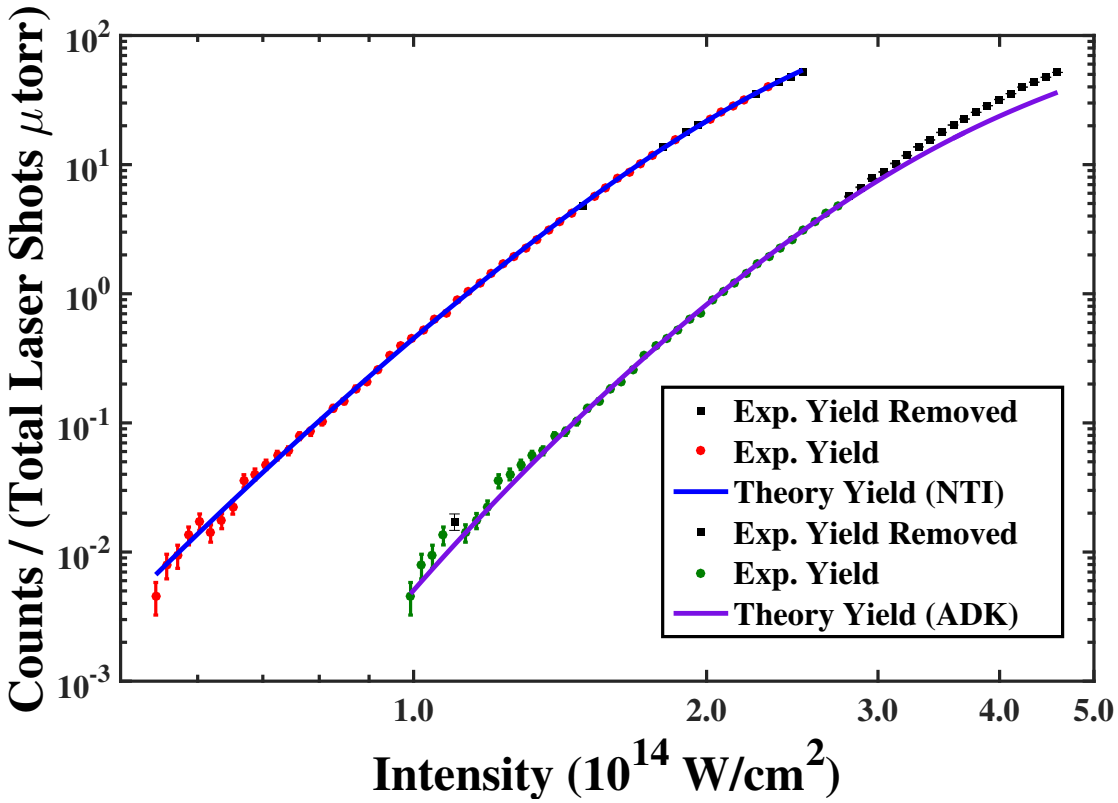

Figure 4.4: The experimental ionization yields as a function of intensity are fit to cycle-averaged, volume averaged, theoretical ionization yield curves generated using NTI and ADK theory. The corresponding calibration constants are $\alpha = 4.5 \times 10^{12} W/cm^2 J$ with 8 points removed for NTI and $\alpha = 8.25 \times 10^{12} W/cm^2 J$ with 20 points removed for ADK. Reproduced from Zigo *et al.* [70].

4.3.2 Robust Fitting Procedure

Since our ionization yield is exponential in nature and the experimental error of the yield is inhomogeneous with greater statistical significance at higher intensity, we utilize the method of weighted exponential least squares fitting [71] to find the correct intensity calibration factor. Unfortunately, even with weight corrections, the least squares method is suspectable to poor fitting due to data outliers. In order to make our intensity calibration method more robust, we combine the weighted least squares with a resistant regression method termed as the least trimmed sum (LTS) of squares method [71]. In this method, the weighted squared residuals are sorted from smallest to largest and a predetermined number of the smallest

residuals are used to determine the best fit. The large residuals are considered data outliers and, therefore, do not contribute to the fit.

The weighted exponential residuals are calculated using the following equation:

$$r_i = \frac{\log(N_{i,exp}(\alpha E_{i,exp})) - \log(cN_{i,thry})}{\sigma_i} \tag{4.8}$$

where N_{exp} and N_{thry} are the experimental and theoretical yield, respectively, and σ is the standard error of the experimental yield. The yield in equation (4.6) is proportional to parameters (pressure, spot size, etc) that are independent of the sample parameters, therefore, c is a scaling factor to adjust the theoretical yield to match the experimental yield. The experimental intensity is proportional to the energy-per-pulse measured, $I_{exp} = \alpha E_{exp}$, making α the intensity calibration factor.

Now we reorder the residuals from smallest to largest. The set $r_1, r_2, ..., r_n$ becomes $r_{(1)}, r_{(2)}, ..., r_{(n)}$ after ordering, and then, through the least squares fitting method, we calculate the weighted root mean square error under the LTS method ($wRMSE_{LTS}$) for every c and α. The smallest $wRMSE_{LTS}$ value indicates the best fit for a given h, where h is the number of experimental yield points used from the original data set.

$$wRMSE_{LTS} = \arg\min_{\alpha,c} \sqrt{\frac{1}{h} \cdot \sum_{i=1}^{h} (r_{(i)})^2} \tag{4.9}$$

Once the α coefficient is determined, it can be used to convert any measured energy-per-pulse to its corresponding peak intensity, assuming the laser pulse characteristics and laser focusing conditions have gone unchanged. At this point, the intensity is considered to be calibrated. In the following subsection, an example of the intensity calibration is shown as it is used in the experiments presented in this thesis and more details involving the fitting process are discussed, such as how to determine if the fit can be trusted.

4.3.3 Intensity Calibration Example

When performing regression analysis, there are four main assumptions that must be satisfied:

1. Linearity

2. Statistical Independence

3. Homoscedasticity

4. Normality

If the the least squares fitting method were performed on the experimental and theoretical data without careful considerations, the fit would be unreliable because assumptions (1), (3), and (4) would be incorrect. To follow, we will explain the steps we take to ensure all four assumptions are satisfied.

Since the yield grows exponentially for most of the intensity range used in the experiment, using an exponential regression method makes the data transformed such that it is treated in a linear manner. Therefore, assumption (1) is now valid. Furthermore, when the measurements in the experiment are performed, the high intensity signals have more counts per laser shot and, therefore, the data does not have the same statistical error for each intensity point. Thus, there is a non-normal distribution of errors for the data set. This violates assumption (4). The solution to this is to use a weighted regression method where the residuals are normalized to the experimental errors.

With three of the four assumptions satisfied, assumption (3) is the only one left unfulfilled. Homoscedasticity is essentially a constant variance of the residuals as a function of the independent variable. The assumption can not be checked to be true without first finding a fit to the data. If a fit is found and it is found that the data set is heteroscedastic, trends are present in the residuals, then the fit is not considered a good fit. If the three other assumptions are valid, then heteroscedasticity can be caused by data outliers and/or a poor model. In our experiment, the theoretical models used are dependent on values that we measure during the experiment, such as pulse duration, sample I_P, and laser central wavelength. We consider the models to be correct within the error of the measured dependent values and under certain conditions that make the model valid. Therefore, data outliers might have a higher influence on how homoscedastic the data set is.

In the remainder of this subsection, we analyze the ramifications of having or not having a good fit through the use of a real example, shown in Fig. 4.4. The following is a detailed intensity calibration from the experiment described in chapter 5. In this example, there were two ionization models used, NTI and ADK. As mentioned earlier, the ADK method is only appropriate when a system is in the tunneling ionization regime. This ultimately hinders the retrieval of an appropriate energy-intensity calibration constant, α. NTI, on the other hand, works quite well due to its accuracy over multiple ionization regimes. An example of the python code used to calculate the theoretical ionization yields, NTI and ADK, and perform the robust fitting procedure can be found in appendix A.1 and A.2.

Calibration with the ADK Ionization Model

In order to determine if the four main assumptions of regression analysis are satisfied, especially homoscedasticity, we look at four different characteristics of the robust fit, shown in Fig. 4.5 and Fig. 4.6 as a function of number of points removed: (i) the standard deviation of the weighted residuals, (ii) the average values of the weighted residuals, (iii) the energy-intensity calibration factor α, and (iv) the index number of the removed point in the intensity array.

A usable energy-intensity calibration factor, α, from equation (4.6), was not achieved with the ADK model. In Fig. 4.5(a), the standard deviation of the weighted residuals does not fall below 2 until after 20 points are removed and never reaches a "steady-state". Similarly, the average values, Fig. 4.5(b), of the residuals never reach a "steady-state", either. This means that the removed points are having large effects on the fit and it is unlikely that homoscedasticity was ever reached.

Additionally, notice how in Fig. 4.6(a), the removed points are grouped together in a particular intensity range, and then, there is a drastic change after 12 points are removed. The removed points remain grouped together, but consist of a different set of data points in a different intensity range. Note, this drastic shift is also reflected in the intensity calibration coefficients shown in Fig. 4.5(c), where an increase of 13% occurs from 12 to 18 data points

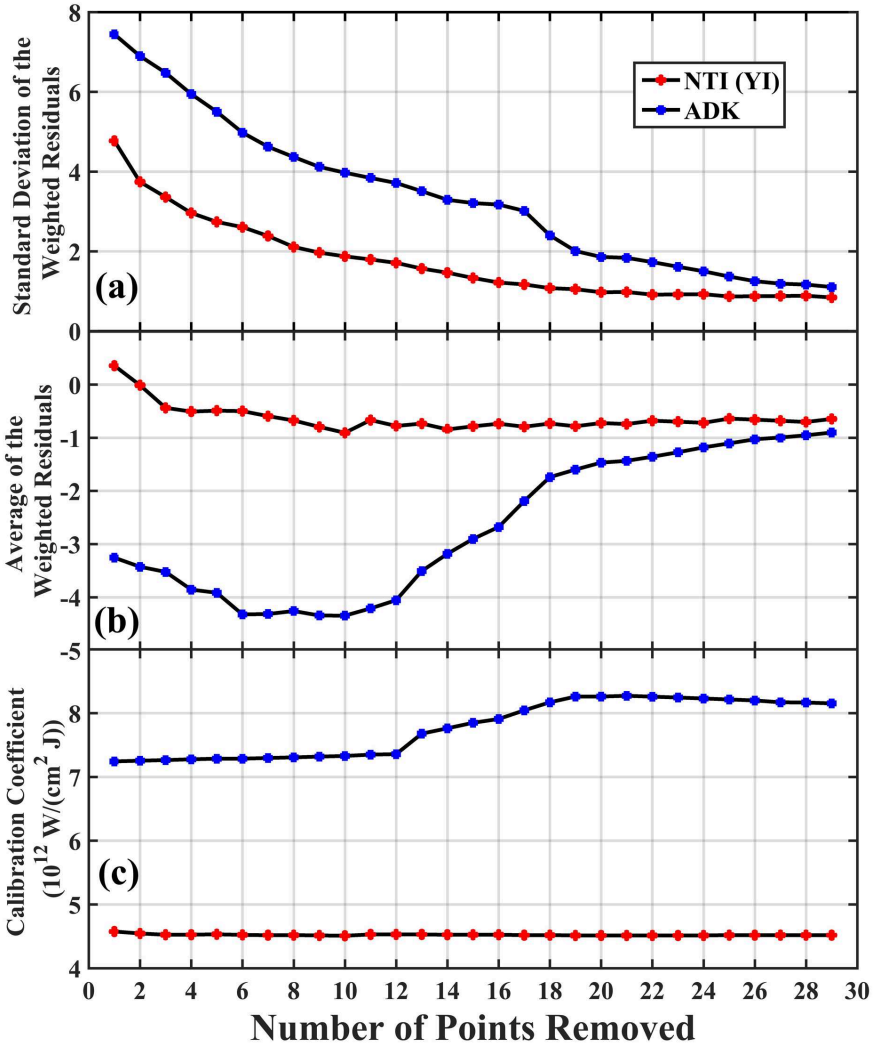

Figure 4.5: The (a) standard deviation of the residuals, (b) average of the residuals, and (c) retrieved intensity calibration coefficients as a function of the number of points removed in the robust fitting procedure using both NTI and ADK ionization methods. Reproduced from the supplementary information of Zigo *et al.* [70].

removed. A visualization of the experimental data and fitted theoretical data is shown in Fig. 4.4 for ADK with 20 points removed.

It is enough to claim these fits as unreliable based on the high standard deviation values of the weighted residuals and the non-constant average values, however, that does not determine the mechanism at fault. In Fig. 4.6(a), the first 12 removed data points of the ADK method are removed from the middle of the intensity range. Past 12, suddenly, removed data points come from the high intensity regime. The fact that the removed points originally came

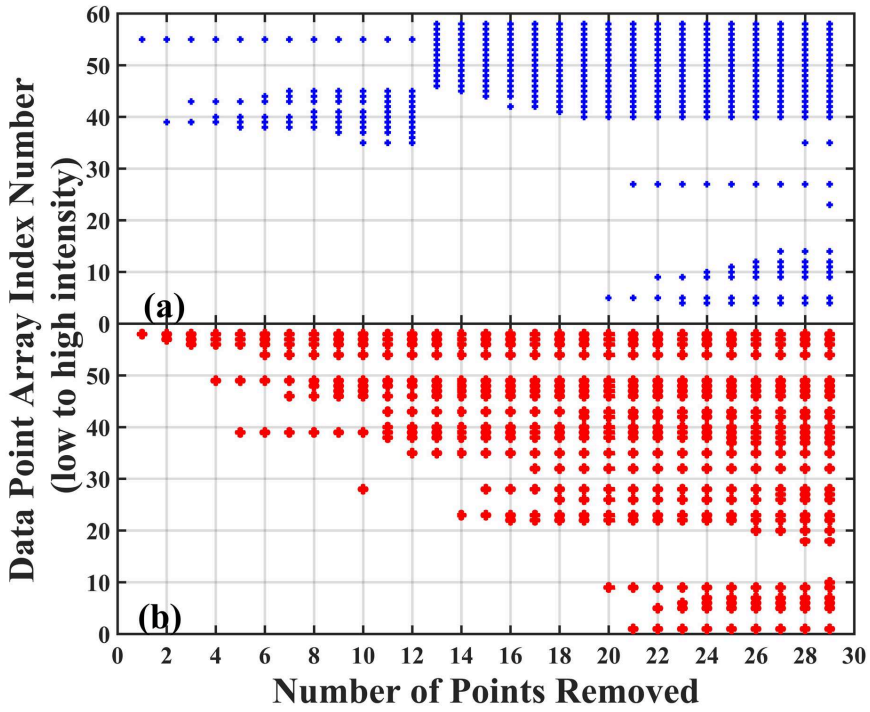

Figure 4.6: A map of which points in the data set were removed as a function of the number of points removed in the robust fitting procedure using (a) ADK theory and (b) NTI theory. Reproduced from the supplementary information of Zigo *et al.* [70].

from the middle intensity regime indicates heteroscedasticity caused by a poor model. It is unlikely that the middle intensity regime would be at fault more than the low intensity regime in terms of a carefully performed experiment. It is clear that the middle residuals were being compensated by both the high and low intensity regimes. Once that was no longer the case, i.e. enough points were removed, the model switched to a different fit that favored the middle intensity regime more. It should be noted that the high intensity regime was anticipated to be favored based on the knowledge that ADK works better in the tunneling regime, $\gamma << 1$. In practice, however, the lower intensity regime was favored. This is due to the small data set and larger experimental error in the low intensity regime which allows more flexibility in the fitting in that regime. One main disadvantage of the robust fitting analysis is that sufficient data points over a large enough intensity range need to be taken in the experiment in order to determine a good fit. Misleading results can be observed if too many points are removed. The absolute break down of the method is when more than half of the points are removed.

Calibration with the Non-adiabatic Tunneling Ionization Model

In this example, where the NTI model is used, we identify a good fit and reliable calibration within the error of both the experiment and theoretical model. The argon experimental ionization yield data set is identical to the one used in the previous subsection where ADK theory was utilized. Again, we look at the characteristics of the robust fit, shown in Fig. 4.5 and Fig. 4.6 as a function of number of points removed in order to determine if the four main assumptions of regression analysis are satisfied.

In Fig. 4.5(b), we reach a "steady-state" average value of ≈ -0.75 in the weighted residuals after the removal of 8 data points. Unfortunately, a "steady-state" alone does not indicate that the fits are now homoscedastic. Note that in order to confirm homoscedasticity, the variance of the residuals must be constant even if more points are removed from the data set. In Fig. 4.5(a), a standard deviation of 2 or lower occurs after 8 data points are removed. Unfortunately, the small data set prevents a constant standard deviation. However, we can infer homoscedasticity based on a "steady-state" of the average residual value, meaning the remaining "would be removed" data points do not significantly contribute to the overall fit and, also, the remaining "would be removed" data points become spread out over the entire data set as shown in Fig. 4.6(b). Note, the point at which homoscedasticity is reached is also reflected in the values of the intensity calibration coefficients, however, much more subtly. In Fig. 4.5(c), the coefficients do change as a function of data points removed, however, the change from all points to "steady-state" is small and on the order of 1%. The coefficient used for this article was $\alpha = 4.5 \times 10^{12}$ resulting from the removal of 8 data points. For a visualization of the experimental data and fitted theoretical data, see Fig. 4.4.

The main advantage of the robust fitting procedure is the insight it gives into the quality of the experiment. In Fig. 4.6(b), the main data points contributing to the misidentification of the true intensity calibration coefficient were data points in the high intensity regime. In this regime, two things occur, detection saturation and yield saturation with volume averaging effects. Although both issues could be contributing, it is more likely that detection saturation is occurring. In the counting method, see 5.2.2, there is the possibility of being

unable to temporally resolve single counts if too many arrive to the detector at similar times per laser shot. This causes an artificial decrease in yield at high intensity which would not be expected to be reflected in any of the ionization models. A volume averaging effect, on the other hand, should be less likely to contribute since the ionization model has already taken that into account. In our intensity calibration model, we do assume a gaussian laser profile. If this is not the case in the actual experiment, then volume yield saturation may influence the ionization yields significantly starting at the incorrect intensity. This would cause the model to also be incorrect at higher intensities.

The discussion and examples of the robust fitting procedure for use in intensity calibration were published in Zigo *et al.* [70], mainly in the supplementary information section.

4.4 Improvements and Outlook

Thus far, our intensity calibration via ionization method was discussed as a superior method to other intensity determining strategies, such as the spot-size measurement or simple regression methods; however, there are still issues. Due to the nonlinearity of the strong-field interaction, the experimental ionization yields as a function of intensity can be rather complex in structure. Error induced by poor statistics, an unstable laser, or systematic measurement errors can produce exponential changes in the ionization yields. Other effects can impact the smoothness of of the yield curve, such as if resonant states are encountered during excitation to the continuum or higher charge states are produced causing saturation effects. Even the focal profile of the laser influences the slopes of the ionization curves, and in our model, we assume a gaussian profile. We can control as many influences as possible to simplify the measurement, but, in the end, the result stands as measured.

In order for the intensity calibration to be successful, within an accuracy of better than 5%, the theory needs to be able to reproduce the experimental result to an acceptable degree of accuracy within the error of the measurement. The question is, what factors about the intensity calibration method have the most influence on the end result? Can an error be assigned to the calibrated intensity?

The attempt to discover the answers to these questions is an active research endeavour within the majority of the Kansas State University James R. Macdonald Laboratory experimental and theory groups. The author of this thesis is an active contributor and collaborator regarding this research project. By focusing their efforts of an intensity calibration using helium as the calibration gas, a full TDSE simulation of the laser-atom interaction can be used as the theoretical comparison. We can pinpoint the weaknesses in the experimental information required to have the TDSE results match the experimental results. Once the experimental limitations have been identified and improved, investigation into more complex gases can be attempted. The inquiry being, how does the single active electron (SAE) influence the theoretical results, since the full TDSE calculation of atoms beyond He is close to impossible with current computational technology? To what degree does the necessary approximation in the theory affect the results of the intensity calibration? In order to move forward, we need an estimate of the theoretical error.

The accurate representation of experimental intensities is a concern of many in the ultrafast community. Other groups have investigated the questions we posed above and it is a growing research interest. Note that in Zhao *et al.* [40], a push for the use of the PPT ionization model was encouraged for intensity determination in strong-field experiments and in Pullen *et al.* [24], laser intensities were measured with 1% accuracy by comparing experimental photoelectron yields of atomic hydrogen to theoretical yields from the a numerical solution to the three-dimensional TDSE.

4.5 Summary

In this chapter, we discussed two very different ways of experimentally determining the peak intensities used in a strong-field ionization experiment. We claim that the method through which ionization itself is used is superior. We show a new method for intensity calibration using a robust fitting procedure. Through the explanation of the intensity calibration method, we call attention to common experimental actualities that influence ion yield studies. Also, the analysis through this method allows one to see where the theory and experiment diverge.

In the following chapters, we will present strong-field ionization experiments where the ionization intensity calibration method using the robust fitting procedure is used. The method was essential to the success of this thesis work.

Chapter 5

Strong-field Ionization of Stereoisomers

In this chapter, we begin our experimental investigation of the strong-field ionization of molecules. With the focus on single ionization only, the chapter presents an experiment where the ionization yields of the parent ion of two isomeric molecules are measured and compared. The ratio of the experimental yields for each isomeric pair is then compared to theory.

5.1 Introduction to Molecular Isomers

An isomer is defined as a molecule that is elementally the same as another molecule, but structurally different. As a consequence, the macroscopic properties (e.g. melting point, boiling point, appearance characteristics) of one isomer compared to the other are different. To start, there are many different types of isomers, see Fig. 5.1, but only two main classifications of isomers, stereoisomers and structural isomers. Each classification is split into many different subclassifications or types, such as diastereomers and enantiomers (chiral) for stereoisomers or chain, position, and functional group for structural isomers.

Another way to think about isomers is through the concept of potential energy surfaces

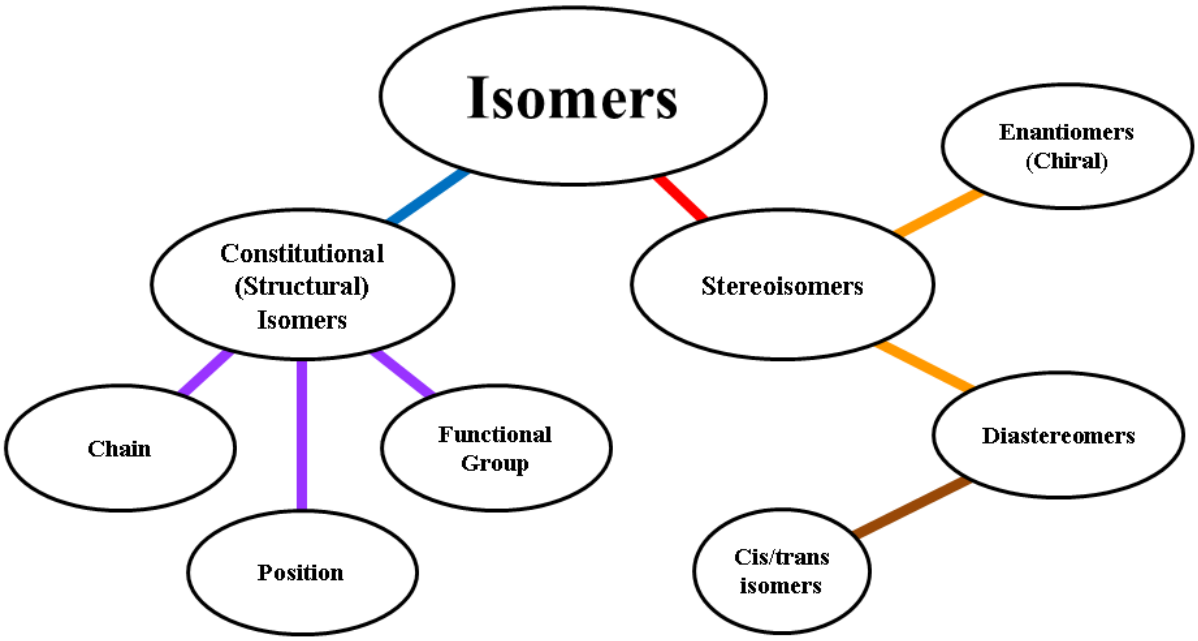

Figure 5.1: The various categories of isomers.

(PES). The simplest example of a PES is that of a diatomic molecule. The potential energy of the system can be described as a function of the bond length between the two atoms of the molecule. There is only one ground state (minimum energy) configuration of the diatomic molecule. As a consequence, the 1-dimensional PES is a continuous curve with a global minimum at the bond length for the ground state geometry of the molecule, see Fig 5.2. In the case of molecular isomers, the molecule has to have at least three elements within its composition and, therefore, additional degrees of freedom are required to describe the PES. In the more than three element case, the PES becomes a hypersurface (multidimensional PES) which is impossible to visualize. Just as with the diatomic case, there is a global minimum of the hypersurface that indicates the absolute ground state of the system. Mathematically:

$$\frac{\partial \boldsymbol{E}}{\partial \boldsymbol{q}_1} = \frac{\partial \boldsymbol{E}}{\partial \boldsymbol{q}_2} = \ldots = 0 \tag{5.1}$$

where $\boldsymbol{E}$ is the potential energy and $\boldsymbol{q}_i$ are geometric parameters, such as bond length and the angle between bonds.

In addition, there are also relative (local) minima that would also satisfy equation (5.1).

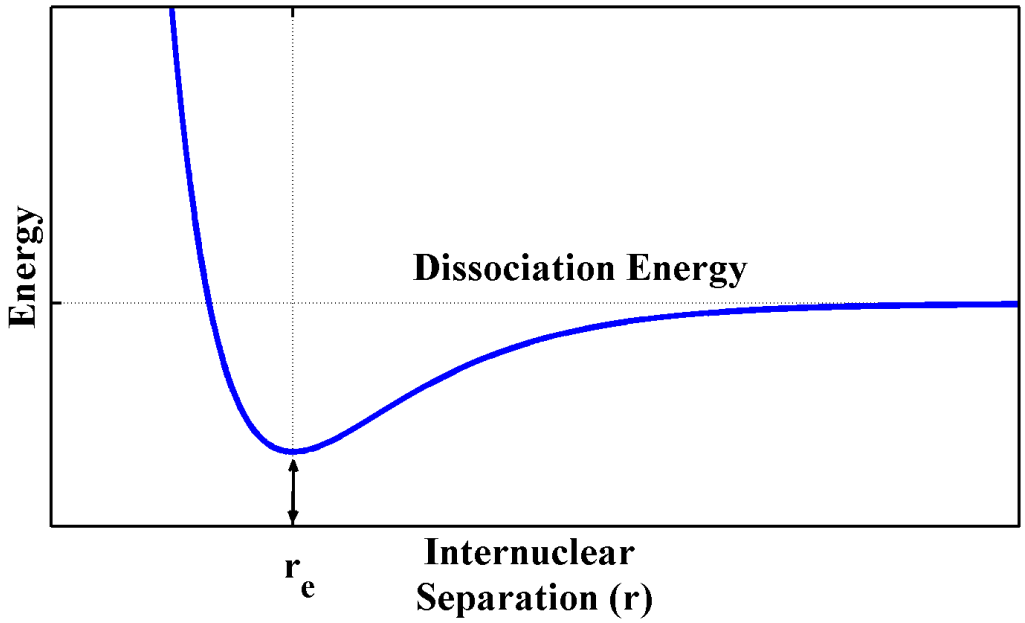

Figure 5.2: The potential energy surface for a diatomic molecule. The minimum indicates the ground state bond length between the two atoms.

Those relative minima are the geometries of the molecule that are isomers to the absolute ground state of the system. See Fig. 5.3 for a visualization of this phenomenon. A more in-depth discussion of PES's can be found in ref. [72].

As is evident by the difference in energy of isomeric ground states, each molecular configuration is different from the others both macroscopically and quantum mechanically. In the following sections and chapters of this thesis, we study the stereoisomers of 1,2-dichloroethylene and 2-butene, Fig. 5.5, where bonds are simply rearranged. Also we study the structural isomers of the hydrocarbons C_4H_6 and C_4H_{10}, Fig. 6.4, where bonds are not only rearranged, but are also replaced by different types (single, double, triple). Further details will be introduced for each molecule in future sections.

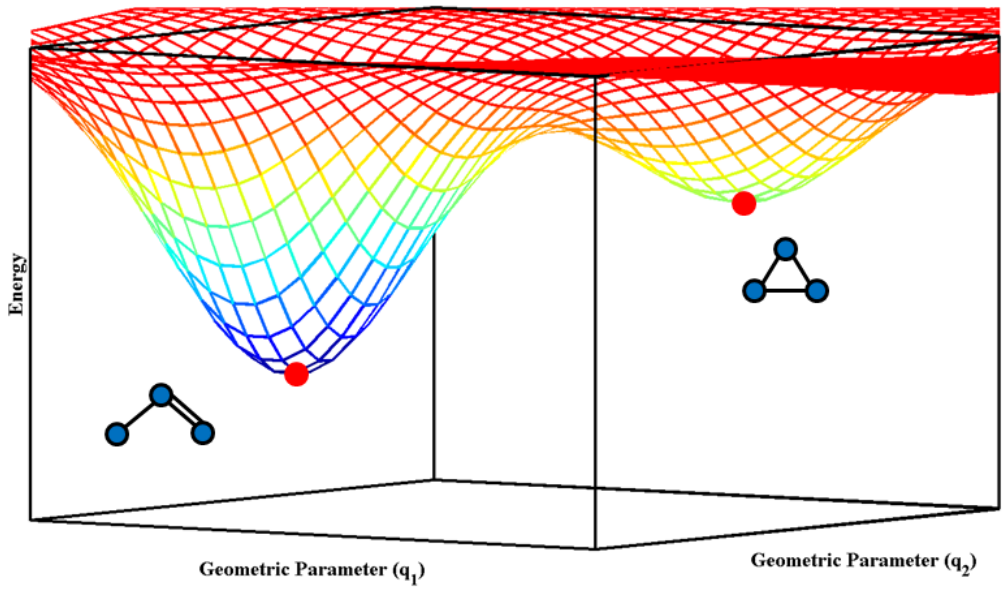

Figure 5.3: The potential energy surface for a polyatomic molecule. The minima indicate the ground state configurations of the elemental set, i.e. isomers

5.2 Experimental Configurations and Details

The main objective of this experiment is to obtain the single ionization yields of molecular isomers as a function of laser intensity. This is achieved through the use of a time-of-flight mass spectrometer (TOFMS), as described in chapter 3.

5.2.1 Motivation: Differential Characterization of Samples

Higher-order Harmonic Generation from Stereoisomers

Although the general motivation of studying isomeric molecules at strong-field intensities remains to better improve the understanding of the impact of structural differences on ionization yields which in turn can help to improve modern theories of molecular ionization, the results of previous studies using higher-order harmonic generation (HHG) to probe the differences between isomeric molecules also help to motivate the study. The HHG process is commonly described by the semi-classical model known as the "three-step model". An

electron tunnel ionizes (strong-field limit) and gains energy in the continuum as it propagates away from the parent atom/molecule. When the laser field changes direction, the electron recombines with the parent atom/molecule and releases the excess energy as a photon, usually in the XUV for 800 nm light. This effect occurs every laser cycle of an intense femtosecond laser pulse and the resulting photons are higher-order harmonics of the laser's center frequency. The resulting HHG spectrum (energy resolved photon signal) can be used as a spectroscopic tool to better understand the electronic structure of atoms and molecules, as mentioned in chapter 1. The average integrated HHG spectrum is considered the HHG yield.

In 2011, Wong *et al.* [41] (see erratum [42]) report the results of an experiment where the HHG yields of two isomeric pairs are measured (the same molecules to be described in section 5.2.3). It was found that there were large differences in the HHG yields when comparing a single pair of isomers, up to a factor of 10, depending on the molecules being studied and the experimental conditions. The suspected cause of the difference in yield was the ionization step of the HHG process. This is something that can be measured and investigated, as will be shown in this chapter.

Strong-field Ionization of Polar Molecules

Within the last decade, targeted experiments studying aligned polar molecules in the presence of a strong electric field were mainly focused on simple molecules, such as CO, OCS, and NO. [73–78] In general, the goal of these experiments is to better understand the effects of a permanent molecular dipole moment on the ionization yields and dynamics of molecules. As will be described in section 5.2.3, the stereoisomer pairs we investigate in this chapter have the property of one being polar and the other non-polar. This allows us to compare the effect of polarity on the single ionization yield of one molecule that is elementally the same as another.

5.2.2 Experimental Setup and Data Acquisition

Our experiment utilizes HITS, see section 3.1.1 with an output of 790 nm central wavelength, $\sim$ 30 fs FWHM pulse duration, and $\sim$ 50 nm bandwidth. The pulse output, which was close to fourier transform limited, was characterized using the home-built SHG-FROG and FROG technique described in section 3.1.3. The maximum energy used was on the order of 200μJ. The beam was irised to about 1.5 cm from an original $1/e^2$ width of 2.2 cm. Shown in Fig. 5.4, the laser light was focused into the spectrometer's interaction region using a fused silica 15 cm plano-convex lens with an anti-reflective coating covering the VIS-NIR spectral range (650 - 1050 nm). The light was polarized parallel to the detector surface. The pulse energy, and consequently the intensity, was controlled via a rotatable half waveplate and a polarizing beam cube. Based on Malus's Law, the intensity as a function of angle is:

$$I(\theta) = I_0 \sin^2(2\theta) \tag{5.2}$$

where I_0 is the maximum intensity at 45° and θ is the angle of the waveplate with respect to the transmission axis of the beam cube. The input light is already linearly polarized before the waveplate. A full depiction of the experimental setup is shown in Fig. 5.4.

Single-shot TOF and photodiode traces were obtained using a fast oscilloscope (picoscope 5203), as described in section 3.2.2. In this particular experiment, the photodiode was placed before the attenuation optics giving single-shot access to pulse energy fluctuations, see Fig. 5.4, but not a direct measurement of the pulse energy from after the interaction region. We found that, on average, the laser energy fluctuated with a $2.15\% - 2.5\%$ single-shot standard deviation over each experiment.

We assign an energy to each data point via an angle-to-energy calibration associated with the $\lambda/2$-waveplate angles. The calibration was performed by measuring the power at a variety of angle positions of the waveplate within the full range of energies and finding the best fit based on those measurements. The fitted model for each experiment had a relative standard error for the forecast of $< 0.5\%$ for all energies used. A combination of the photodiode measurements and the mapping of angle to energy were used to determine the

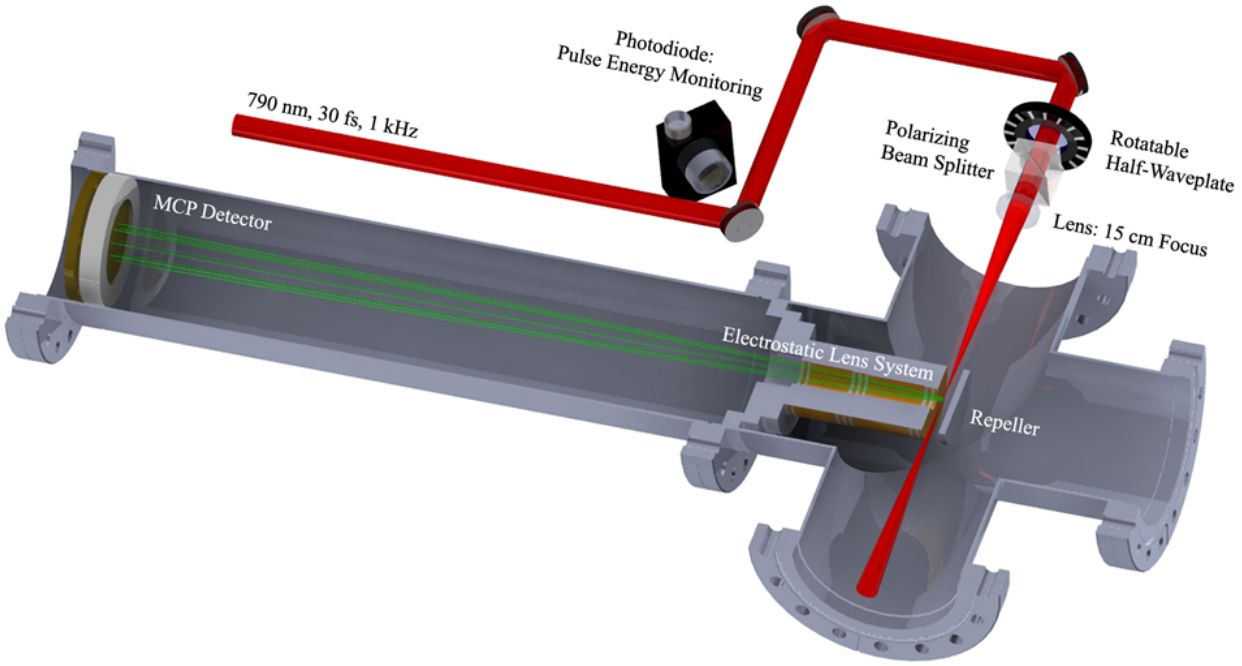

Figure 5.4: Experimental optical setup and time-of-flight mass spectrometer for stereoisomer experiment. The combination of a half-waveplate and polarizing beam cube allows for intensity attenuation control in the interaction region. Adapted from Zigo *et al.* [70].

actual energy used in the experiment. Peak intensities were determined through the use of the intensity calibration method outlined in section 4.3. The calibration gas was argon for this experiment.

The ionization yield is determined, post-experiment, by gating the signal around the expected time of arrival of a particular ion and either integrating the total signal or counting the individual hits on the detector for every laser shot. We found that at low intensity, before saturation, the counting method was best and is how the data is presented in this chapter. An example of the MATLAB code used to analyze the measured TOF yields can be found in appendix A.3.

5.2.3 Samples: Stereoisomers

We look at the ionization yields of the first ion of the isomeric molecules *cis*- and *trans*-1,2-dichloroethylene (1,2-DCE) and *cis*- and *trans*-2-butene (Fig. 5.5(a)-(d)). Both samples were

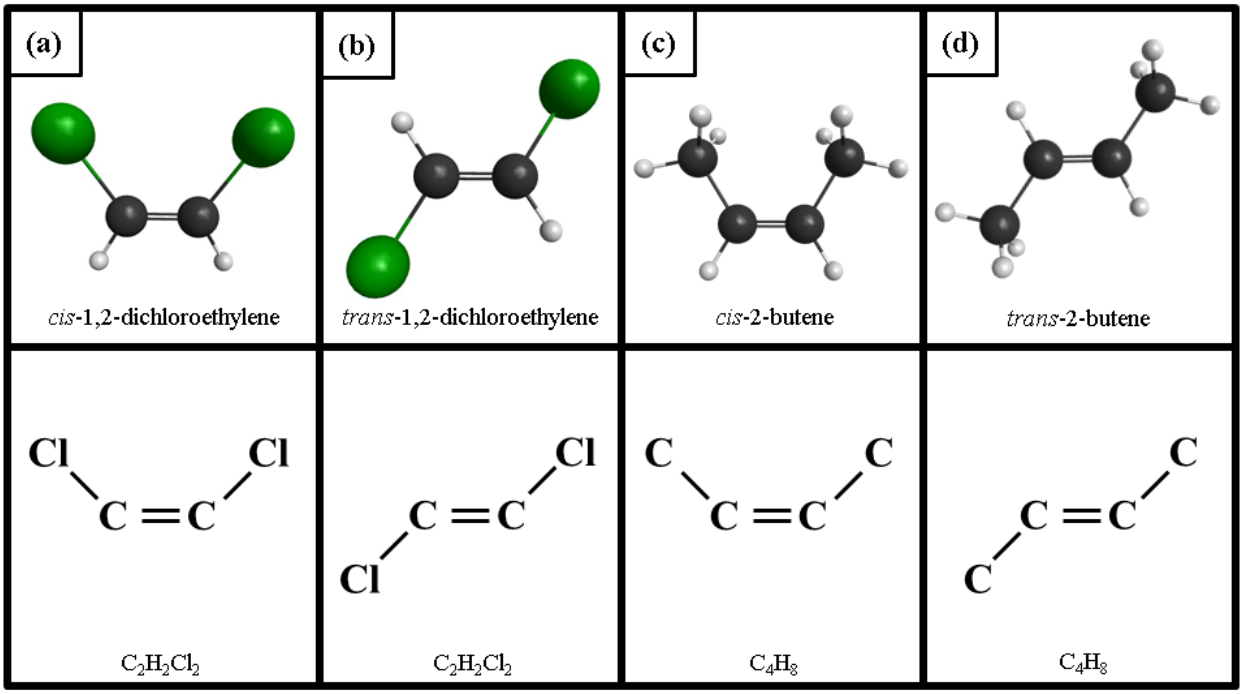

Figure 5.5: Molecular geometries: (a) *cis*- and (b) *trans*-1,2-dichloroethylene, (c) *cis*- and (d) *trans*-2-butene.

purchased from Sigma Aldrich with the following purification: 97% *cis*-1,2-DCE, 98% *trans*-1,2-DCE, and $\geqq$ 99% *cis*- and *trans*-2-butene. These molecules have ionization potentials of, 9.11$\pm$0.01 eV and 9.10$\pm$0.01 eV for *cis*- and *trans*-2-butene and 9.66$\pm$0.01 eV and 9.64$\pm$0.02 eV for *cis*- and *trans*-1,2-DCE respectively [79]. Each isomer was studied separately under identical conditions.

Experimentally, each sample is introduced to the chamber via a gas line ending with a glass capillary with a hollow core diameter of 200μm. The capillary is about 6cm from the interaction region producing a homogeneous gas density throughout the interaction region. The background base pressure is $\approx 10^{-9}$ torr and for an experiment is brought up to a working pressure in the range of about 10^{-7} to 10^{-6} torr depending on the sample. To account for experimental fluctuations, we monitor and correct for pressure variations, so that each yield is considered pressure (density) independent. The method is described in section 3.2.2. For this experiment, the pressure would reduce on average from the initial starting pressure by a factor of 0.5 for 2-butene, and 0.65 for 1,2-DCE. Also note, the samples are randomly

oriented. There is no active attempt to align the samples for any of the experiments shown in this thesis.

The molecules mentioned are two pairs of diastereomers which is signified by both of their prefixes associated with each molecule's name; *cis* indicating "the same side" and *trans* indicating "across from". For example, looking at 1,2-DCE, which is halogenated ethylene with two chlorine atoms, the *cis* configuration has both chlorine on the same side of the molecular axis (the carbon double bond) and the *trans* has one of the chlorine atoms on the opposite side of the molecular axis, but not mirror image of the other chlorine. See Fig. 5.5(a) and (b). As mentioned earlier, the rearrangement of the atoms is in such a way that the types of bonds remain the same. As a result, even though the molecular orbitals are now vastly different between the two molecules, the ground state energy is almost degenerate, differing only on the order of 0.01 eV. This characteristic makes diastereomers excellent candidates to see if large differences can occur in the ionization yields of both molecules in the strong-field limit, since they are both similar to each other.

In addition, due to the symmetries present in the isomeric configurations of both 1,2-DCE and 2-butene, one isomer, *cis*, has a permanent dipole moment and the other, *trans*, has none. This means that the *cis* isomer is polar and the *trans* isomer is nonpolar. We can investigate the influence of polarity on strong-field ionization while simultaneously inquiring about the influence of structural differences. The calculated permanent dipole moment of the "ground state" wavefunction of *cis*-1,2-DCE is -0.75 au and for *cis*-2-butene it is -0.97 au.

5.3 Results

5.3.1 Experimental Results

The ionization yields as a function of intensity for each isomer pair are shown in Fig. 5.6. The intensity range for each isomer was bounded by two phenomena, statistical significance for low intensity and molecular fragmentation for high intensity. Each intensity data point

per sample was determined by an average of $N = 64000$ laser shots and the statistical error was calculated as the standard error.

In Fig. 5.6 and 5.8, the intensity range is extended to show the effects of molecular fragmentation on the yields and the ratio of the yields. Fragmentation analysis, shown in Fig. 5.7, compared the ratio of the fragment ion to the parent ion. Since there is always some nonzero probability that fragmentation will occur, we found that the rate of fragmentation changed at the same rate with respect to intensity as the rate for the parent ion until the saturation intensity was reached. This intensity is clearly determined by the change in slope of the yield ratio (fragment / parent ion) as seen in Fig. 5.7. Note that we only show the fragmentation analysis for *cis*-2-butene, however, we found similar trends for all isomers studied and determined saturation intensities appropriately.

For each pair of isomers (see Fig. 5.5(a)-(d)), we investigated the ratio of the yields (trans / cis) of the first ion of the parent molecule as a function of intensity. The ratios are depicted in Fig. 5.8(a) and Fig. 5.8(b). The ionization yields as a function of intensity for 1,2-DCE, Fig. 5.6(b), are statistically significant in the intensity range 0.12 - $0.26 \times 10^{14} \frac{W}{cm^2}$ before fragmentation. The upper intensity bound is determined by the isomer that fragments at the lower intensity of the pair. The ratio, Fig. 5.8(b), is roughly 1.0 - 1.4 within that intensity range. For this isomeric pair, the *trans*-isomer yield dominates the *cis*-isomer yield. The ratio changes such that the *cis*-isomer yield has a stronger presence at higher intensity compared to lower intensity, however, it never dominates the *trans*-isomer yield. Molecular fragmentation becomes visible at about $0.26 \times 10^{14} \frac{W}{cm^2}$ where the *trans*-isomer fragments before the *cis*-isomer which is visible in the change in slope of the ratio to show a decrease in *trans*-isomer yield contribution. Note, the chlorine in 1,2-DCE has two stable isotopes found in nature, Cl-35 and Cl-37 with 75.76% and 24.24% abundance [80], respectively. This results in three different ionization peaks in the time-of-flight spectra. In this chapter, we only show data for the 35-35 isotope pair.

The ionization yields as a function of intensity for 2-butene, Fig. 5.6(a), are statistically significant in the intensity range 0.10 - $0.32 \times 10^{14} \frac{W}{cm^2}$ before fragmentation. The ratio, Fig. 5.8(a), is roughly 0.4 - 0.7 within that intensity range. For this isomeric pair, the *cis*-isomer

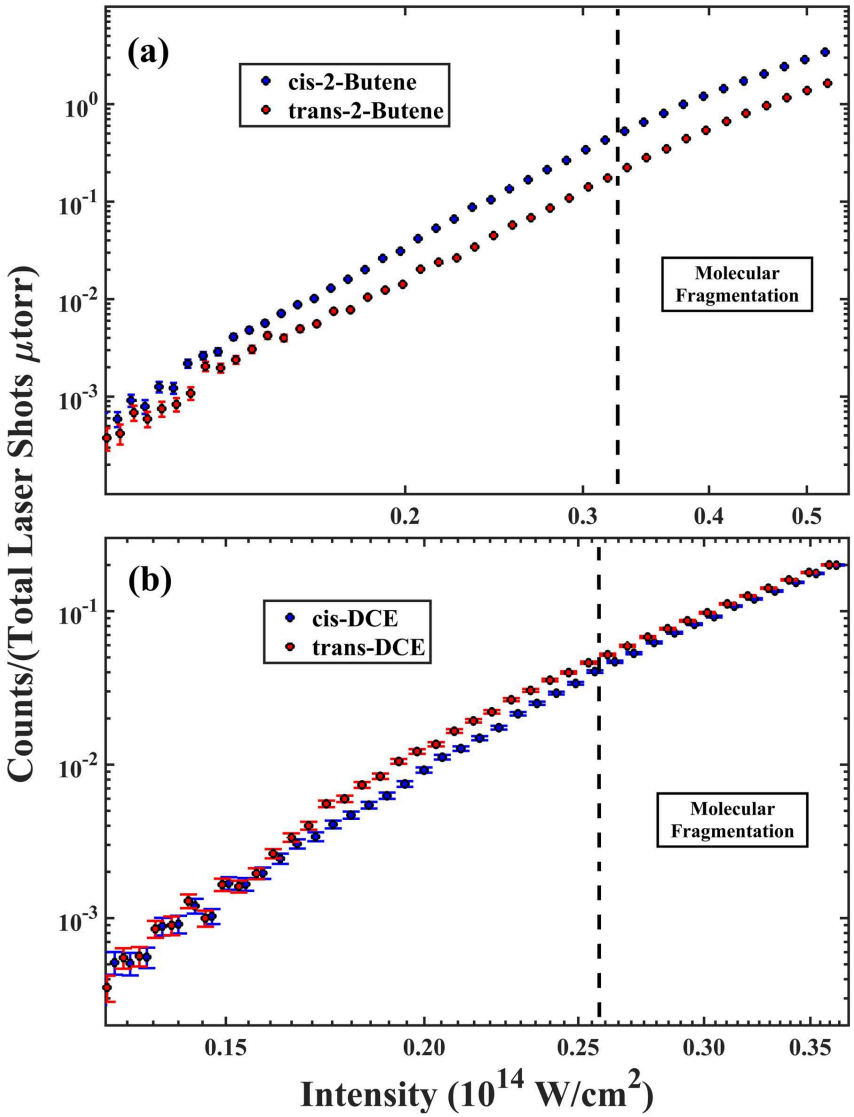

Figure 5.6: Ionization yields of the first ion of (a) 2-butene and (b) 1,2-DCE (35-35 isotope) as a function of intensity (log-log). Adapted from Zigo *et al.* [70].

yield dominates the *trans*-isomer yield. The ratio changes such that the *cis*-isomer yield has a stronger presence at higher intensity compared to lower intensity. Molecular fragmentation becomes visible at about $0.32 \times 10^{14} \frac{W}{cm^2}$ where the *cis*-isomer fragments before the *trans*-isomer which is visible in the change in slope of the ratio to show a decrease in *cis*-isomer yield contribution.

By comparing the two ratios of the two pairs of stereoisomers, we observe that no isomeric structure (cis or trans) dominates compared to the other, therefore we do not observe a

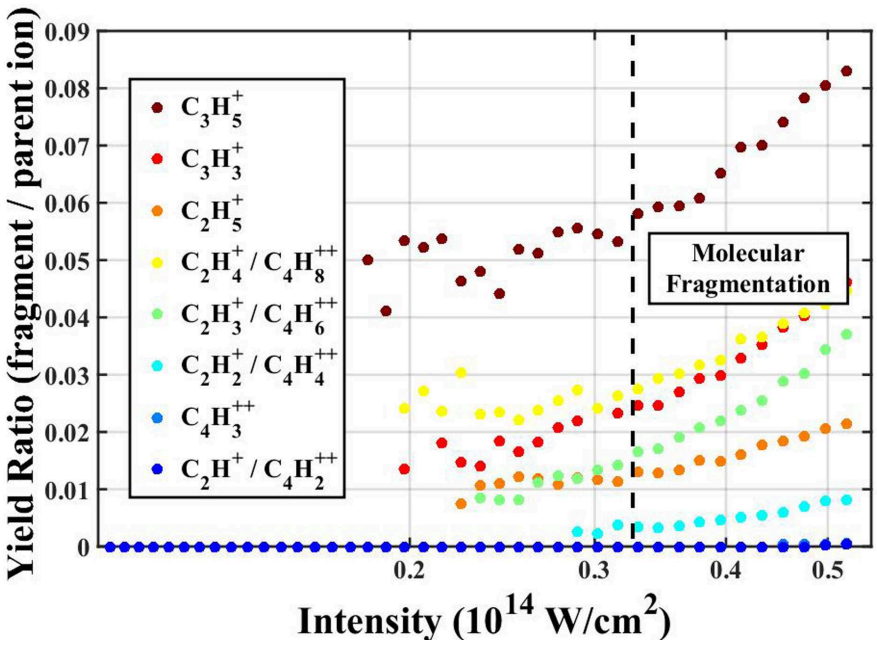

Figure 5.7: Ratio of the ionization yield of a molecular fragment and the parent ion of *cis*-2-butene. Molecular fragmentation is significant beyond $0.32 \times 10^{14} \frac{W}{cm^2}$. Reproduced from Zigo *et al.* [70].

strong influence of molecular polarity on the molecular ionization. In addition, the trend of the ratios before fragmentation are not the same between the two pairs. For 1,2-DCE, there is a positive slope in the ratio in favor of the non-polar *trans*-isomer. 2-butene, however, is the opposite with a negative slope in favor of the polar *cis*-isomer. In both cases, however, the dominating isomer is the first to fragment.

Note that our laser pulse duration was only 30 fs long (FWHM) and at low intensities, we do not expect significant alignment for these relatively heavy molecules. Similarly, we do not expect significant molecular structural rearrangement during this short time period. Further investigations are needed, however, in particular with different laser wavelengths, to rule out possible resonance effects to an excited state.

5.3.2 Theoretical Results

The following theoretical calculations in this section were performed by Anh-Thu Le and the explanation of the theoretical results was published in Zigo *et al.* [70].

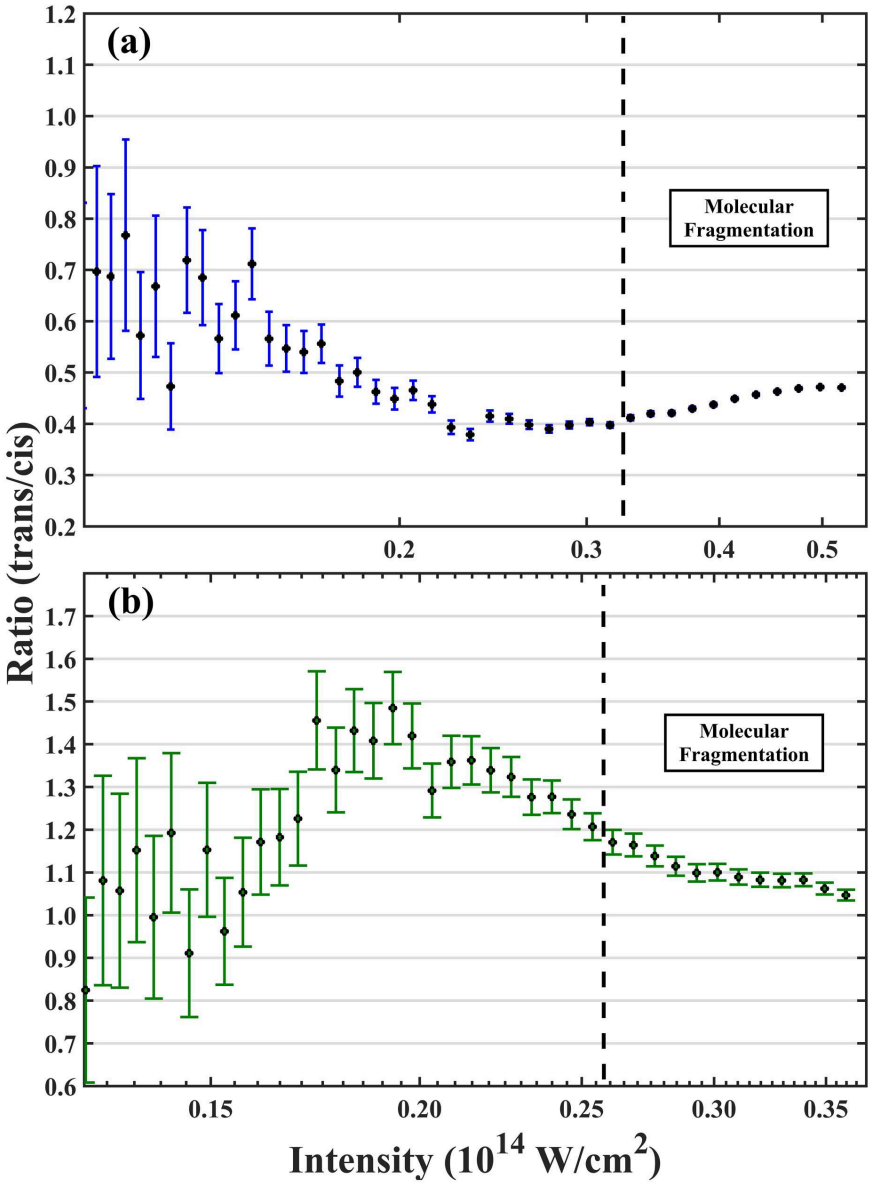

Figure 5.8: Ratio of the yield of the parent ion of the stereoisomers of (a) 2-butene and (b) 1,2-DCE (35-35 isotope) as a function of intensity (semi-log). Adapted from Zigo *et al.* [70].

To simulate the experimental measurement we utilize three different approaches: (i) strong-field approximation (SFA) [15, 56], (ii) molecular tunneling ionization theory (molecular orbital Ammosov-Delone-Krainov, MO-ADK) [34], and (iii) molecular orbital Perelomov-Popov-Terent'ev (MO-PPT) [20, 81], as described in section 2.3. Since the *cis*-isomers are polar molecules, we also extended these calculations to include Stark corrections [32, 73, 74].

In our calculations we use ground-state electronic wavefunctions obtained from the Gaus-

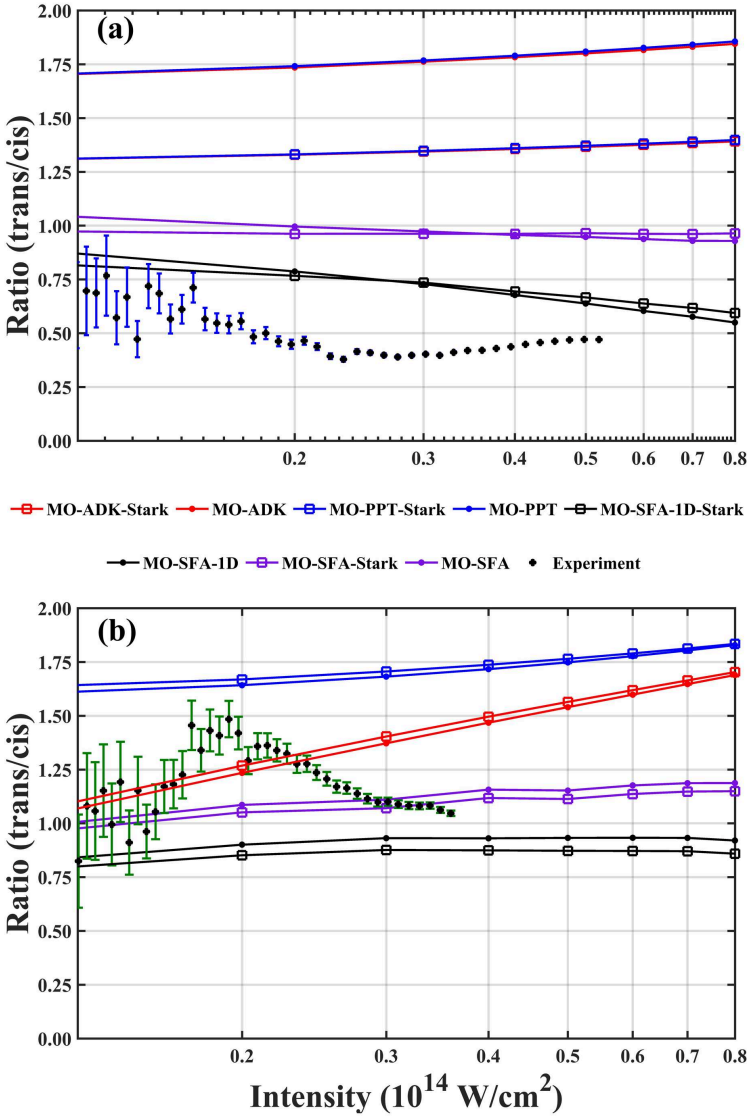

Figure 5.9: Ratio of the yield of the parent ion of the stereoisomers of (a) 2-butene and (b) 1,2-DCE (35-35 isotope) as a function of intensity with theoretical and experimental data (semi-log). Scattered points are experimental results, connected scattered points are theoretical results. Adapted from Zigo *et al.* [70].

sian quantum chemistry code [54] and employ the augmented correlation consistent polarized valence triple-zeta (aug-cc-pVTZ) basis set at the Hartree-Fock level. Within the single-active-electron (SAE) approximation, we take the highest occupied molecular orbital (HOMO) as the "ground state". With these wavefunctions, the SFA calculation was then carried out for each target for different laser parameters integrating over all electron emission directions. The calculations were carried out within the clamped nuclei approximation in

which the nuclei are fixed at their equilibrium positions of the neutral molecule (implying vertical ionization in the 1-D case). The geometry optimizations were performed and the results are consistent with other calculations [79]. The results are shown in Fig. 5.9 for a typical range of the laser intensities. As one can see, the trans/cis intensity ratio for 1,2-DCE is of order 1 ($\pm$50% or so) for both theory and experiment. Note that theoretical results from Wong *et al.* [41] (see Erratum [42]) show somewhat smaller trans/cis ratios (close to 0.5), who used different intensities and/or wavelengths. The SFA trans/cis ratio for 2-butene is also close to 1, while experimental ratio is close to 0.5. Fig. 5.9(a) also reveals that, the agreement between theory and experiments for trans/cis ratio for 2-butene is somewhat improved by considering only electron emission along polarization axis (MO-SFA-1D-Stark), although such trend is not quite clear for 1,2-DCE.

We have also found that the intensity ratios are relatively stable with respect to the different basis sets and methods (Hatree-Fock and density functional (DFT) such as B3LYP) used in Gaussian. The dipoles of the HOMO can change up to 20% depending on the basis sets and methods used, however, the Stark correction within the SFA only slightly changes the ionization yield ratios (square points). Our calculations were done with the permanent dipoles of the active electron "ground-state" wavefunction (i.e. HOMO) of -0.97 au and -0.75 au for *cis*-2-butene and *cis*-1,2-DCE, respectively. For the *trans*-isomers, the dipoles are zero. Note, we did not attempt to go beyond the Hartree-Fock and DFT for strong-field ionization. Most of the theoretical treatments for strong-field ionization have been, so far, limited to the SAE approximation. Going beyond the Hartree-Fock approximation would also mean going beyond the SAE. We note that, so far, only in a few rare cases electron correlation was suspected to contribute to the total ionization.

Within the MO-ADK theory, we first extracted the molecular structure coefficients C_{lm} using the HOMO's obtained from the Gaussian quantum chemistry code. This is done by matching the HOMO with its asymptotic wavefunction [34] at some large distance r_e. As it is well-known, this procedure is not quite satisfactory even with large basis sets which includes diffuse functions, since Gaussian-type orbitals decrease too rapidly at large distances [36]. Therefore, the ionization rate for each isomer obtained from the MO-ADK still changes quite

significantly with distance r_e, even with large basis sets, such as aug-cc-pVTZ and aug-cc-pVQZ. Nevertheless, we found that the trans/cis intensity ratio are relatively stable when $r_e \approx 10$ to 15 au. Our results from MO-ADK for the trans/cis intensity ratio is shown in Fig. 5.9, which is in a relatively good agreement with the SFA results. Here we took $r_e = 10$ and $r_e = 14$ au for 2-butene and 1,2-DCE, respectively. Note that, in general, the validity of the MO-ADK might be questionable at low intensities used in the experiments. We, therefore, also provide here MO-PPT results [81] which is expected to have a much broader range of validity compared to MO-ADK. Overall, SFA results agree better with experiments than both MO-PPT and MO-ADK. The Stark correction does not change the results significantly in all cases.

It should be noted that in the recent papers by Tolstikhin and collaborators [37, 38], an adiabatic expansion in parabolic coordinates approach has been developed to describe ionization process from molecules, including polar molecules. Madsen *et al.* [36] have also shown that quite accurate wavefunctions at asymptotic distances can be obtained from Gaussian with a well-designed basis sets. Unfortunately, both of these approaches are limited to simple molecules so far.

5.4 Summary and Discussion

In this chapter we report the ionization yield of two pairs of stereoisomers, *cis*-, *trans*-1,2-DCE, and *cis*-, *trans*-2-butene, as a function of intensity. The ratio trans/cis as a function of intensity is also reported for each isomeric pair. From a strong-field ionization perspective, because of the similar ionization potentials between the pairs, we would expect very similar yields (yield ratio ≈ 1), especially in this case where the molecules were randomly oriented. Therefore, it is surprising that one isomer dominates its stereoisomer counterpart by a factor on the order of 1.5 - 2. We show that there is no single dominating configuration, *cis*- versus *trans*-isomer. Such lack of dominant configuration suggests that molecular polarity is not a major contributor to the rate at which a molecule ionizes under strong fields.

To provide a marker on the current status of theoretical molecular ionization models,

the measured ionization ratios are compared to theoretically-calculated ionization yield ratios. We consider stark-corrected SFA to be one of the best methods available in terms of calculating molecular ionization rates. However, the experimental results do not match the SFA theory, even within the error of the measurement for all samples studied. Similarly, the MO-ADK and MO-PPT results are a poor fit as well. This is expected for MO-ADK because it is suited for the tunneling regime and our experiments are performed when $\gamma > 1$. MO-PPT, on the other hand, is better suited for a broader range of γ, however, the ratio has the least agreement with the experimental results. Although we can assign yield ratios confidence based on the model, the difference in ratio values between the different theoretical methods, SFA, MO-ADK, and MO-PPT, is large enough to question how well the theory can actually represent the experiment. It should be noted that typical, yet computationally costly corrections were neglected in the molecular calculations. One important omission was focal volume averaging. Also, although many steps were taken to report only the ionization of parent molecular ions prior to fragmentation, the dynamics of such complex polyatomic molecules are not included in the theoretical calculations and might have a large influence on the ionization yield even in the intensity range of our experiment.

It should be pointed out that our results are in disagreement with previous studies [41, 42], where the difference in HHG yield is attributed to differences in ionization yields. The calculated ionization yield ratios were 5 for 2-butene and 2 for 1,2-DCE. The *cis*-isomer dominates in both cases. The authors in [41, 42] do, however, maintain that the angular distributions of the electron for 800 nm, 1300 nm and 1500 nm look qualitatively similar to each other. At 790 nm, we experimentally observed ionization differences that do not support the current explanation for the large yield differences present in the HHG studies, meaning it is likely direct ionization measurements in the near-infrared will yield similar results. Further studies at longer wavelengths are required and were performed, see chapter 6.

Note, the results and conclusions of this chapter were published in Zigo *et al.* [70].

Chapter 6

Wavelength-dependent Study of the Strong-field Ionization of Isomeric Molecules

6.1 Introduction

In this chapter, we continue our study of molecular isomers in the strong-field limit. In this iteration of experiments, we diversify the isomers in which we study by adding structural isomers to the list of samples. The rearrangement of bond types in structural isomers add more prominent changes within the isomeric pairs. Properties such as increased differences between ionization potentials and overall cross-sections allow for a broader investigation of what contributes to strong-field ionization.

In addition, we explore the influence of wavelength on the strong-field ionization yield of isomeric molecules. We utilize femtosecond laser pulses in the NIR, up to 2000 nm, to accomplish this study. As described in chapter 2, when all things in a molecular/atomic system remain the same, going to longer wavelengths will push the system further into the tunneling ionization regime. Recall equation (2.1) and equation (2.2) for the Keldysh parameter and ponderomotive potential, respectively. As the wavelength increases, the ponderomotive

potential increases resulting in a smaller Keldysh parameter. As described in section 2.1.1, $\gamma \ll 1$ is an indication of being in the tunneling ionization regime. To illustrate this point, we plot, Fig. 6.1, the Keldysh parameter of a $I_p = 10$ eV atom as a function of laser peak intensity for various laser center wavelengths. Overall, by varying the samples and parameters of the ionization experiments, we also introduce new examples to be used to improve on current molecular ionization theories.

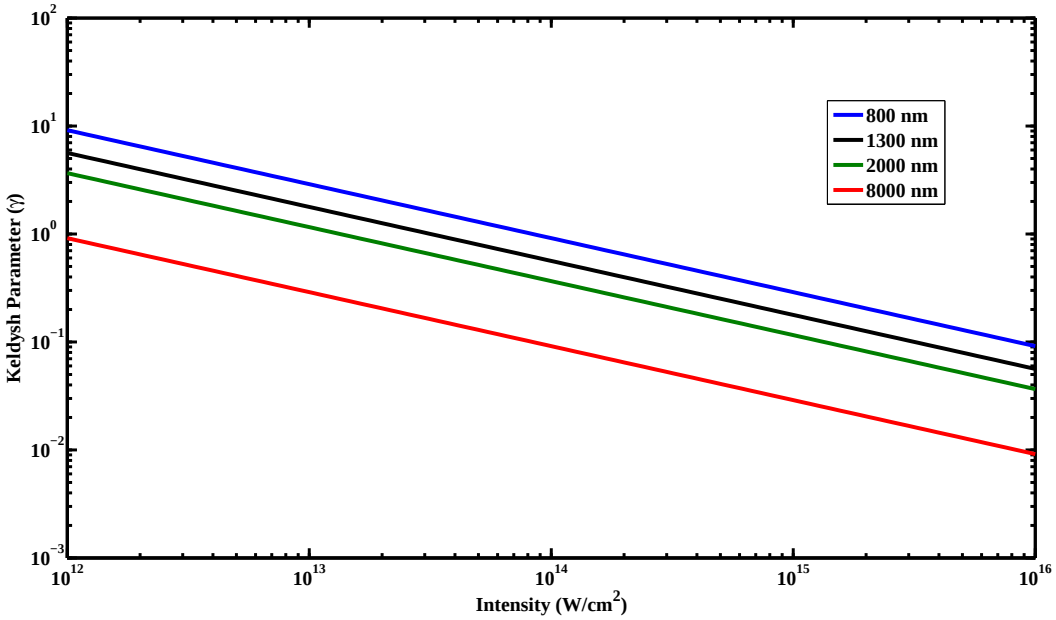

Figure 6.1: The Keldysh parameter of a $I_p = 10$ eV atom as a function of laser peak intensity for various laser center wavelengths.

6.2 Experimental Configurations and Details

As a continuation of the experiments from chapter 5, the wavelength-dependent studies are performed in the same TOFMS as previously described. Some key changes to the experimental setup have been made to improve the accuracy and reliability of the experiment and will be outlined in the following subsection. However, please note, unless otherwise stated, experimental details will be the same as the previous strong-field ionization experiment.

6.2.1 Experimental Setup and Data Acquisition

As before, our experiment utilizes HITS, see section 3.1.1, with an output of 790 nm central wavelength. In addition, we utilize the OPA option of HITS, which gives a tunable NIR source from 1150 - 2600 nm. For these experiments, we generate three separate output pulses, simultaneously: one centered at $\sim$ 790 nm which is split prior to the input of the OPA, referred to as the Ti:sapphire output, one that is centered at $\sim$ 1300 nm, referred to as the signal, and another that is centered at $\sim$ 2000 nm, referred to as the idler. As described in section 3.1.2, the Ti:sapphire output has a bandwidth of $\sim$ 50 nm, $\sim$ 71 nm for the signal, and $\sim$ 147 nm for the idler, which should correspond to the following Fourier transform limited pulse durations, respectively, 25 fs, 35 fs, and 40 fs. In actuality, however, for the following experiments, the pulses are all chirped linearly due to the group velocity dispersion (GVD) caused by propagation through various media (air, optic material, etc.). As a result, the pulse durations become roughly 30 fs, 50 fs, and 100 fs, respectively. The pulses were characterized using the home-built SHG-FROG and FROG technique described in section 3.1.3. It should be noted that we were unable to compensate for the induced dispersion for the experiments.

Table 6.1 summarizes the characteristics of the pulses used in the experiments in this chapter and Fig. 6.2 shows the retrieved spectra. The center wavelength for each pulse was determined by using the spectra in Fig. 6.2 and the following equation:

$$\lambda_c = \frac{1}{s_{total}} \int s(\lambda)\lambda d\lambda \tag{6.1}$$

where λ is the wavelength, s is the spectral amplitude, and $s_{total} = \int s(\lambda)d\lambda$.

It should be noted that the experiments using the pulses depicted in Fig. 6.2(a) were performed a few months before the ones depicted in Fig. 6.2(b). The variations in the pulse characteristics are a result of slightly different tunings of HITS and the OPA.

Similar to the experiment in chapter 5 for the Ti:sapphire output, the maximum energy used was on the order of 200μJ. The beam was irised to about 1.5 cm from an original $1/e^2$ width of 2.2 cm. The OPA outputs, on the other hand, have much smaller $1/e^2$ widths

λ_c (nm)	τ_{FWHM} (fs)	FROG error (%)	Samples Used
790	30	0.3	C_4H_6, C_4H_8, C_4H_{10}
1340	50	1.3	C_4H_6, C_4H_8, C_4H_{10}
1300	41	0.9	$C_2H_2Cl_2$
2000	100	0.9	C_4H_6, C_4H_8, C_4H_{10}, $C_2H_2Cl_2$

Table 6.1: Pulse characteristics after FROG retrieval.

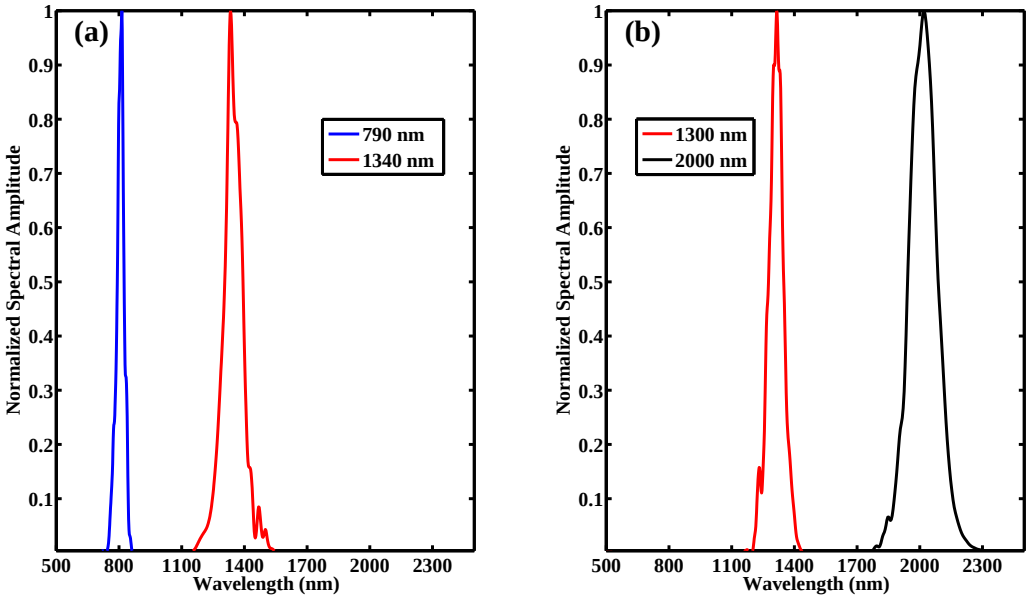

Figure 6.2: FROG retrieved normalized spectra for the experimental laser outputs.

on the order of 0.8 cm and, therefore, did not need to be irised. The maximum energy available prior to the chamber was on the order of 300 - 400 μJ for both the signal and the idler. As will become evident, it is essential to maintain the same alignment for each of the pulses used in the experiment in order to have successful comparison of the ionization yields of each isomeric pair. As a result, many optical elements were shared between the different outputs in order to maintain consistency and reduce alignment error as each output is switched between. The laser light was focused into the spectrometer's interaction region using an uncoated calcium fluoride (CaF_2) 15 cm plano-convex lens. CaF_2 was chosen for its low GVD in the NIR. Due to the differences between the beam sizes and center wavelengths, the different outputs did not necessarily focus the same, therefore, the lens was also placed on a linear translation stage (with micron precision) so that the focal position of each beam

could be adjusted to the center of the interaction region of the spectrometer.

Recall that in the previous experiment, section 5.2.2, the pulse energy, and consequently the intensity, was controlled via a rotatable half waveplate and a polarizing beam cube. In the case of working with a variety of pulses centered throughout the NIR, the use of a beam cube becomes unrealistic. Firstly, the thickness of the material of the cube would induce a considerable amount of chirp to the pulses which we have already stated that we are unable to compensate for. Secondly, different cubes might need to be used for each of the outputs which would induce additional error into the repeatability of laser alignment. As a solution to this issue, the intensity control scheme was changed to the much more robust half-waveplate with grazing incidence on germanium plates technique [82]. The basic idea behind this technique is the polarization of the linearly polarized output light is controlled by a half-waveplate. The light then reflects off two consecutive optical quality germanium plates aligned for incidence at Brewster's angle, ($\theta_B \approx 78\,\text{deg}$ - $76\,\text{deg}$ for 0.8 - 2μm). The polarization component perpendicular to the surface of the germanium (p-polarized) is absorbed/transmitted and the parallel component (s-polarized) is reflected. By adjusting the polarization of the input light, waveplate angle, θ, the pulse energy is attenuated just as in the beam cube technique, equation (5.2) from section 5.2.2. The added benefit of the grazing incidence technique is that the light never travels through any material besides the waveplate and air, therefore eliminating unnecessary GVD. This technique is also universal in the wavelength range of the experiment and is only limited by the transmission efficiency of germanium for the wavelength used. In general, the extinction ratio is relatively flat for the wavelength ranges NIR to LWIR, and drastically worsens in the VIS. For our experiments, the germanium plates were aligned such that the output light was polarized parallel to the detector surface. The use of separate half-waveplates made to accommodate each pulse output's bandwidth was unavoidable. A full depiction of the experimental setup is shown in Fig. 6.3.

Single-shot TOF and photodiode traces were obtained using a fast oscilloscope (picoscope 5244A), as described in section 3.2.2. It should be noted that this is a different oscilloscope than used previously, see chapter 5. This oscilloscope allows for 8, 12, 14, and 15-bit voltage resolution out of a 16-bit total voltage range for 2-channel operation. There is a trade-off

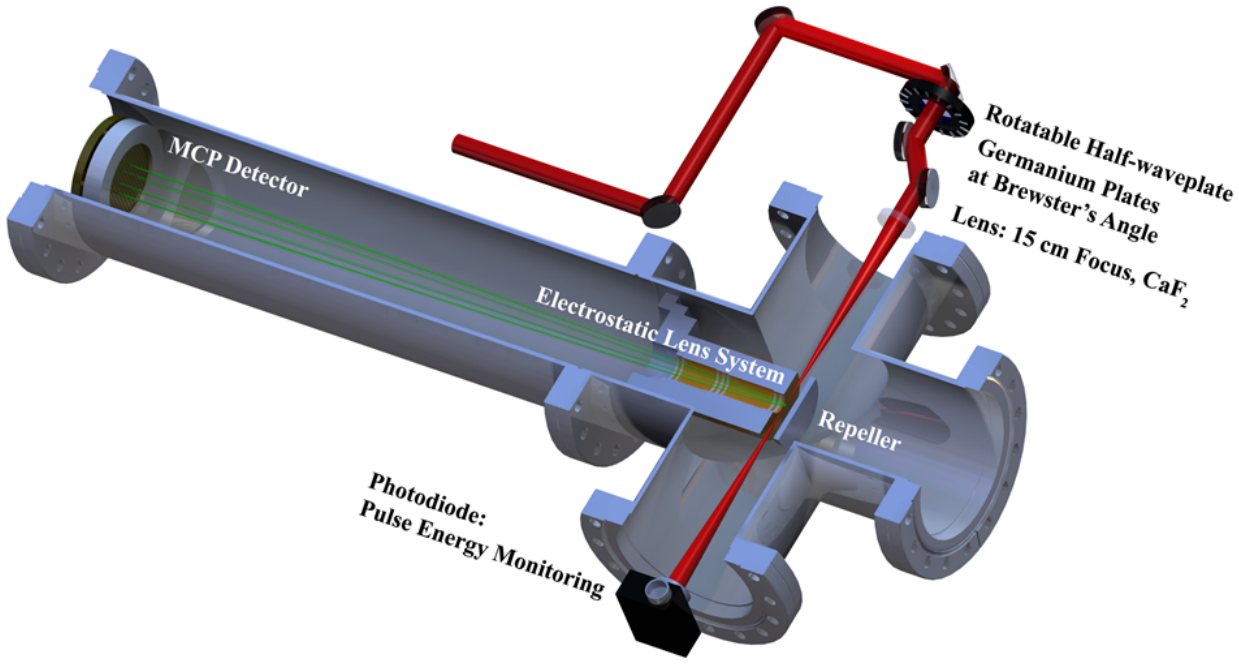

Figure 6.3: Experimental optical setup and time-of-flight mass spectrometer for wavelength-dependent isomer ionization experiment.

between voltage resolution and temporal resolution: an increase in one is a decrease in the other. For the following experiments, we chose 12-bit resolution resulting in a minimum temporal resolution of 4 ns. Due to the low count rate per laser shot at low intensities where single ionization is most prevalent, the loss of temporal resolution is acceptable. Additionally, the increased voltage resolution allows for better distinction between electronic background noise and legitimate ion counts.

Contrasting the previous experiment, the photodiode was placed after the interaction region of the TOF chamber giving single-shot access to pulse energy values and fluctuations, see Fig. 6.3. This is superior to the previous placement as now it directly reflects the input energy on a pulse to pulse basis. Due to the nature of the nonlinear process associated with the generation of the IR light from the OPA, fluctuations in the 790 nm output are exaggerated in the OPA output. Inherently, the OPA output is less stable. Fortunately, having single-shot access allows for intensity discrimination as described in section 3.2.2. Although the experiment is run based on the assumption that there is some waveplate angle-

to-energy calibration, as described in section 5.2.2, the actual calibration does not matter since the integrated photodiode signal values will be used as a means to "rebin" the data such that like intensity data points contribute to the same yield data points. This redistribution of data allows for a more accurate representation of the ionization yield measurements. An example of the MATLAB code used "rebin" intensity values can be found in appendix A.4.

The experimental measurements presented in this chapter were performed over a series of many days with single wavelength, single sample data sets requiring on the order of 4-6 hours of data acquisition time. Naturally, the stability of HITS and OPA outputs were variable throughout with standard deviation errors of $\geq 5\%$ for any given waveplate angle. After redistribution of the integrated photodiode signal values, average intensity data points fell into the range of $0.9\% - 2.7\%$ standard deviation error. We found that this was the case for all of the experiments in this chapter. It should be noted that the same photodiode is used in all cases of the experiment regardless of center wavelength and the photodiode is only operated within the linear response region of the total voltage range.

Peak intensities were determined through the use of the intensity calibration method outlined in section 4.3. The calibration gas was either argon or krypton for this experiment depending on the light source being used. The use of krypton, which has a lower I_p than argon, was due to the energy restrictions of the idler. Since the focusing conditions and photodiode response are different for each light source, a separate intensity calibration was performed for each of the outputs, Ti:sapphire, signal, and idler.

As described previously, ionization yield is determined, post-experiment, by gating the signal around the expected time of arrival of a particular ion and either integrating the total signal or counting the individual hits on the detector for every laser shot. Again, we found that at low intensity, before saturation, the counting method was best. An example of the MATLAB code used to analyze the measured TOF yields can be found in appendix A.3.

6.2.2 Samples: Structural Isomers and Stereoisomers

For the following experiments, we look at the ionization yields of the first ion of various isomeric molecules. As was introduced in the previous experiment in section 5.2.3, the stereoisomers, *cis*- and *trans*-1,2-dichloroethylene (1,2-DCE) and *cis*- and *trans*-2-butene (Fig. 6.4(a)-(d)) are studied at longer wavelengths.

In addition, we add two new isomeric pairs (C_4H_6 and C_4H_{10}) to our investigation, resulting in four new samples, 1,3-butadiene, 1-butyne, butane, and isobutane (Fig. 6.4 (e)-(h)). The two new pairs of samples were purchased from Sigma Aldrich with a purity of $\geq 99\%$ except for 1-butyne which has a purity of $\geq 98\%$. Each isomer is studied separately under identical conditions.

The isomeric pairs, 1,3-butadiene, 1-butyne, and butane, isobutane are considered structural isomers. This means that the rearrangement of atoms also involves the changing of bond types. For example, in the 1,3-butadiene and 1-butyne pair, 1,3-butadiene is considered a conjugated diene, meaning it has two carbon double bonds and results in a zig-zag like structure in the carbon chain. 1-butyne, on the other hand, is an alkyne meaning it has a carbon triple bond followed by a carbon single bond and results in a linear shape for at least four atoms along the axis of the triple bond. Compared to the stereoisomers, this strong difference in structure results in a large change in the relative ground state energy of each isomer, meaning the difference in ionization potential, ΔI_p is significantly different. For 1,3-butadiene and 1-butyne, ΔI_p is on the order of 1 eV and for butane and isobutane, ΔI_p is on the order of 0.1 eV. Specifically, I_p for 1,3-butadiene, 1-butyne, butane, and isobutane are 9.07, 10.18, 10.53, and 10.68 eV, respectively [79].

Although these additional samples were originally chosen for their structural isomer type relationship, the pairs also exhibit the polar and non-polar characteristics of the stereoisomer samples. This was a nice coincidence. 1,3-butadiene and butane are non-polar molecules due to their symmetries and 1-butyne and isobutane are both polar molecules.

It should be noted that the samples were introduced to the TOFMS in the same way as the previous experiment, see section 5.2.2. The pressure in the chamber was monitored

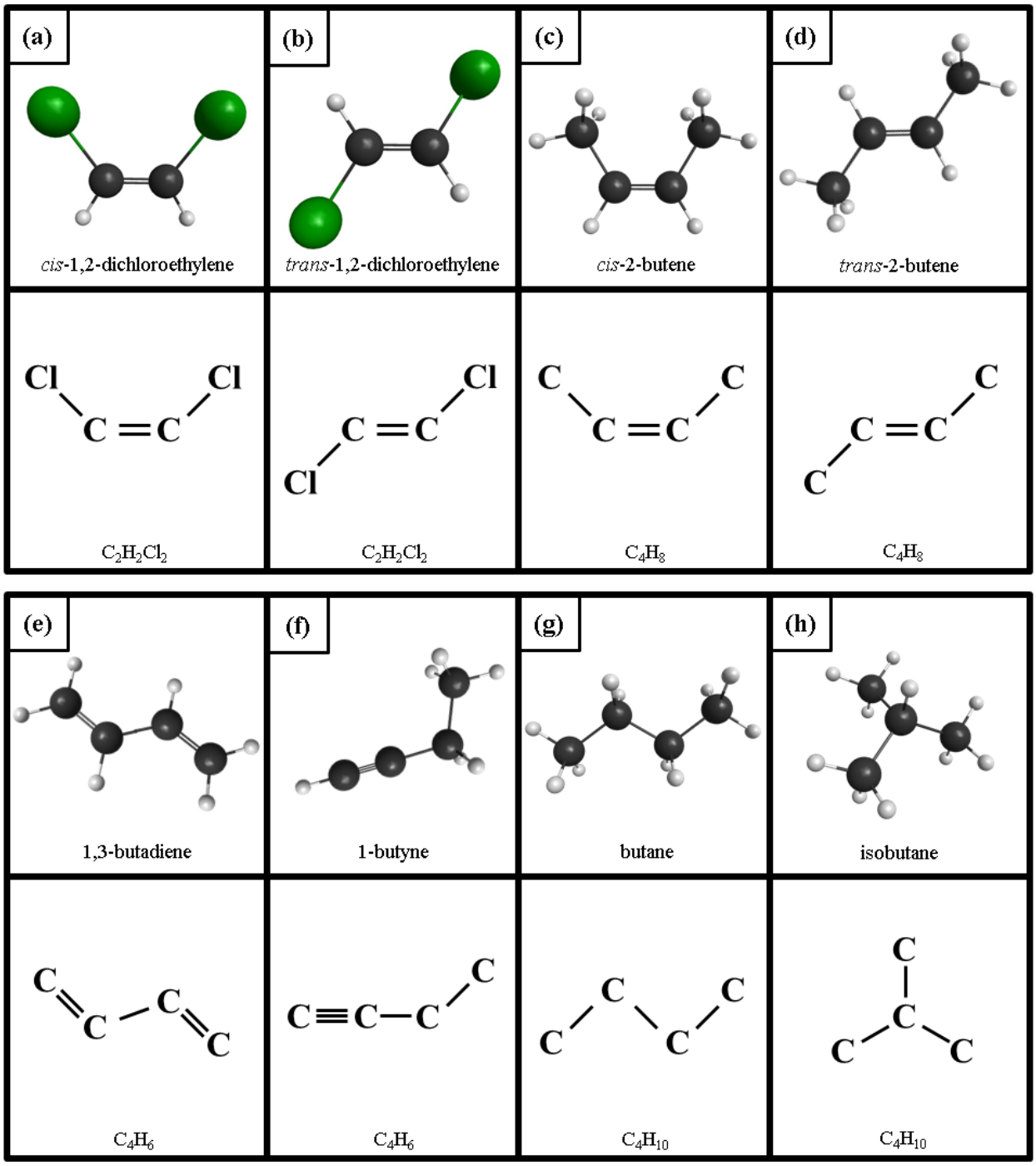

Figure 6.4: Molecular geometries: (a) *cis*- and (b) *trans*-1,2-dichloroethylene, (c) *cis*- and (d) *trans*-2-butene, (e) 1,3-butadiene, (f) 1-butyne, (g) butane, and (h) isobutane.

and recorded throughout all data taking of the following experiments as described in section 3.2.2. The molecules continue to be randomly oriented without any attempt to align them.

6.3 Results and Discussion

6.3.1 Experimental Results

We study the trends of strong-field ionization as a function of intensity on four different pairs of isomeric molecules. In each experiment, data was taken in successive scans over the targeted intensity range with overall more time spent taking data at the lower intensities where count rates are lower. After redistribution of the data points from the intensity discrimination procedure, the number of laser shots per data point was in the range of 55k - 120k laser shots. Our laser pulse durations were 30 - 100 fs long (FWHM) and at low intensities, we do not expect significant alignment for these relatively heavy molecules. Similarly, we do not expect significant molecular structural rearrangement during these short time periods.

C_4H_6: 1,3-butadiene and 1-butyne

First we start with C_4H_6. For 790 nm, the measured ionization yield becomes statistically significant, a standard error of $\leq 20\%$, for 1,3-butadiene at an intensity of 0.29×10^{14} W/cm^2, and begins to fragment significantly at 0.5×10^{14} W/cm^2, see Fig. 6.5. We consider this the experimental intensity range for single ionization of the molecule. Saturation due to molecular fragmentation is determined by looking at the ratios of the yield of the main fragmentation channels and the yield of the parent ion (fragment / parent ion). The entire process of the fragmentation analysis is outlined and demonstrated in section 5.3.1. The structure in the intensity yield plots are a product of three things, multi-photon resonance, fragmentation, and detection saturation. We show the full range of the measurement in order to emphasize this point, see Fig. 6.5. Similarly, for 1340 nm, the intensity range is 0.19 - 0.4×10^{14} W/cm^2, and for 2000 nm, 0.15 - 0.4×10^{14} W/cm^2. Additionally, now looking at

1-butyne, see Fig 6.5, for 790 nm the intensity range is 0.29 - 0.35 $\times 10^{14}$ W/cm^2, for 1340 nm, 0.19 - 0.4 $\times 10^{14}$ W/cm^2, and for 2000 nm, 0.17 - 0.4 $\times 10^{14}$ W/cm^2.

In Fig 6.6 we compare the ionization yields of the parent ion of both C_4H_6 isomers by plotting the ratio 1,3-butadiene / 1-butyne as a function of intensity. For 790 nm, the ratio is roughly 2.1 - 2.7 before fragmentation, for 1340 nm, it is 2 - 3, and for 2000 nm, it is 2.8 - 3.7. This pair has a ΔI_p on the order of 1 eV. As a result, we suggest that the large difference in ionization yield is heavily dominated by the difference in ionization potential, as described by Keldysh [15]. Additionally, looking at the ratios as a function of wavelength, we see that as the photon energy decreases, the more 1,3-butadiene is favored over 1-butyne. Taking into consideration the error of the measurement, the change is not extremely significant, but it does exist.

C_4H_8: *trans*- and *cis*-2-butene

Next we investigate C_4H_8. For 790 nm, the intensity range for *trans*-2-butene is 0.16 - 0.3 $\times 10^{14}$ W/cm^2, see Fig. 6.7. Similarly, for 1340 nm, the intensity range is 0.14 - 0.25 $\times$ 10^{14} W/cm^2, and for 2000 nm, 0.09 - 0.35 $\times 10^{14}$ W/cm^2. Additionally, now looking at *cis*-2-butene, see Fig 6.7(b), for 790 nm the intensity range is 0.15 - 0.3 $\times 10^{14}$ W/cm^2, for 1340 nm, 0.11 - 0.35 $\times 10^{14}$ W/cm^2, and for 2000 nm, 0.09 - 0.35 $\times 10^{14}$ W/cm^2. In Fig 6.8 we compare the ionization yields of the parent ion of both C_4H_8 isomers by plotting the ratio *trans*-2-butene / *cis*-2-butene as a function of intensity. For 790 nm, the ratio is roughly 0.65 - 0.9 before fragmentation, for 1340 nm, it is 0.9 - 1.15, and for 2000 nm, it is 0.75 - 1. This pair has a ΔI_p on the order of 0.01 eV. As a result, we would expect the ionization yields to basically be the same, a ratio of ≈ 1. However, we see the *cis*-isomer dominating for the majority of intensities and wavelengths studied. With that said, we do see a drastic change in the 1340 nm case where in the intensity range of 0.17 - 0.25 $\times 10^{14}$ W/cm^2 the *trans*-isomer dominates which could be the result of a intensity dependent physical process, such as a stark shift though an excited state resonance.

C_4H_{10}: butane and isobutane

Next, we investigate C_4H_{10}. However, before we can present the results, we need to comment on the tendency of C_4H_{10} to fragment very easily. Starting from the statistically significant yield cutoff intensity for both butane and isobutane, we found that the ratio fragment / parent ion for the most probable fragmentation channel, was on the order of 1 - 3. This extremely contrasts the typical ratio values we have seen in the other samples studied of roughly ≤ 0.09. Even though there is an over abundance of fragmentation, we are still able to observe a steady ratio before a sudden change in slope, our condition for determining saturation. Based on these observations, it is very likely that the cation of both butane and isobutane are ions with shorter lifetimes than that of the drift time of the TOFMS. Although we can no longer claim the experiment measures the single ionization yield of the parent ion before fragmentation, we approach the analysis the same as with the other molecules in order to gain some insight about these unique molecules.

For 790 nm, the intensity range for butane is 0.2 - 0.25 $\times$ 10^{14} W/cm^2, see Fig. 6.9. Similarly, for 1340 nm, the intensity range is 0.2 - 0.35 $\times$ 10^{14} W/cm^2, and for 2000 nm, 0.27 - 0.4 $\times$ 10^{14} W/cm^2. Additionally, now looking at isobutane, see Fig 6.9, for 790 nm the intensity range is 0.25 - 0.35 $\times$ 10^{14} W/cm^2, for 1340 nm, 0.18 - 0.35 $\times$ 10^{14} W/cm^2, and for 2000 nm, 0.3 - 0.5 $\times$ 10^{14} W/cm^2. In Fig 6.10 we compare the ionization yields of the parent ion of both C_4H_{10} isomers by plotting the ratio butane / isobutane as a function of intensity. For 790 nm, the ratio is roughly 0.8 - 1 before fragmentation, for 1340 nm, it is 1 - 1.5, and for 2000 nm, it is 1.15 - 1.4. This pair has a ΔI_p on the order of 0.1 eV. As a result, we would expect the ionization yields to be similar with a slight favor for the isomer with lower I_p, butane in this case. However, we see that the dominant isomer is completely dependent on the wavelength. Looking at the ratios as a function of wavelength, we see that as the photon energy decreases, the dominant isomer switches from isobutane to butane with the ratio at unity for 1340 nm.

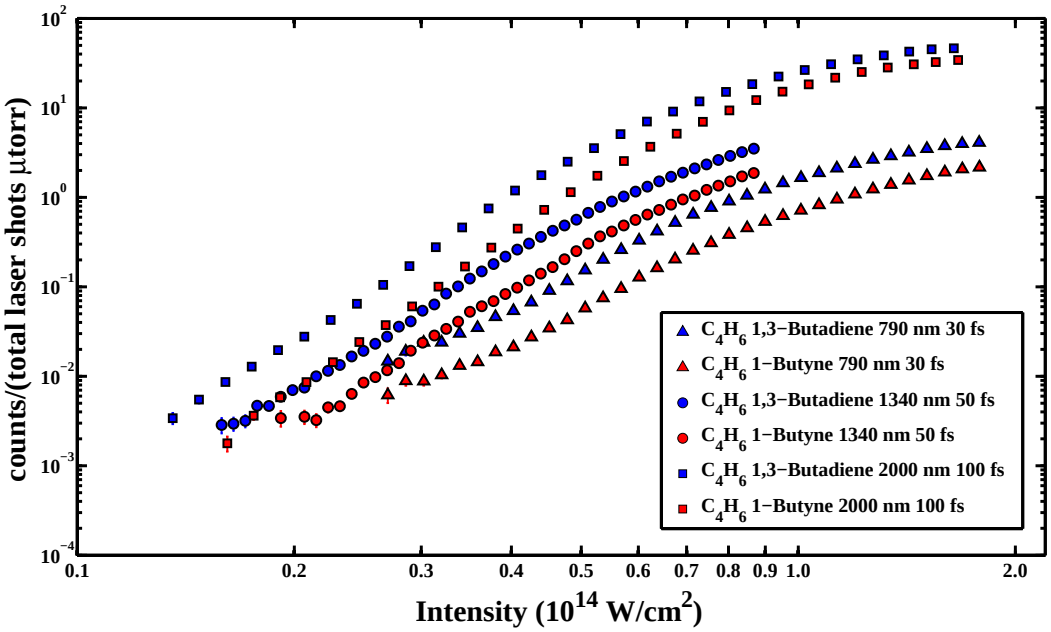

Figure 6.5: The pressure corrected ionization yield of the parent ion of C_4H_6 as a function of intensity. Three different pulse conditions are presented in the graph: (Triangle, 790 nm, 30 fs), (Circle, 1340 nm, 50 fs), and (Square, 2000 nm, 100 fs). Samples: C_4H_6: 1,3-butadiene (blue) and 1-butyne (red).

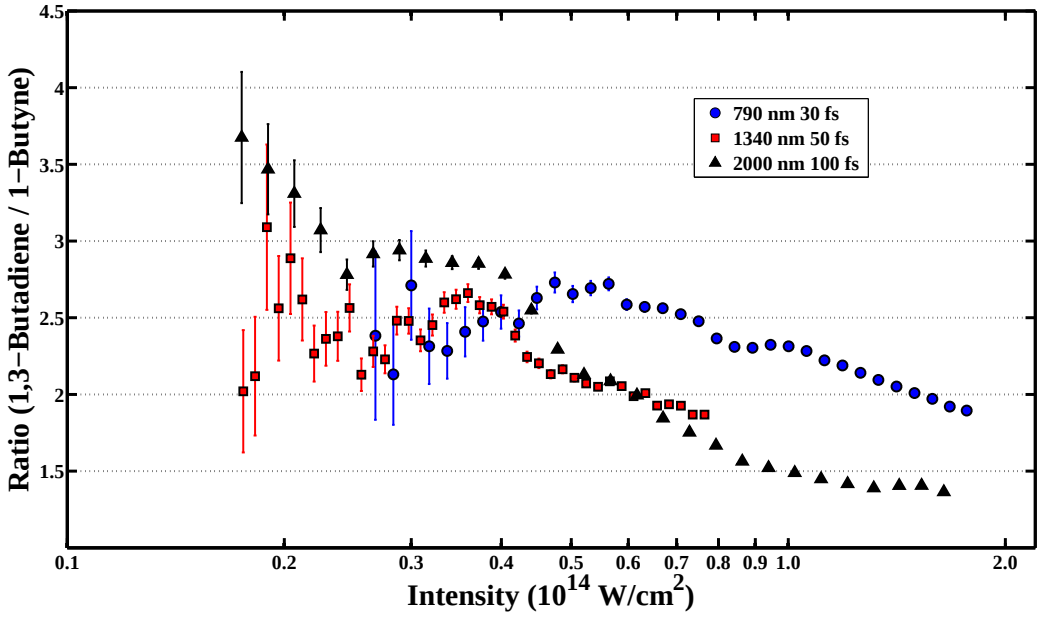

Figure 6.6: The ratio of the pressure corrected ionization yield of the parent ion of C_4H_6, 1,3-butadiene / 1-butyne. Three different pulse conditions are presented in the graph: (blue, circle, 790 nm, 30 fs), (red, square, 1340 nm, 50 fs), and (black, triangle, 2000 nm, 100 fs).

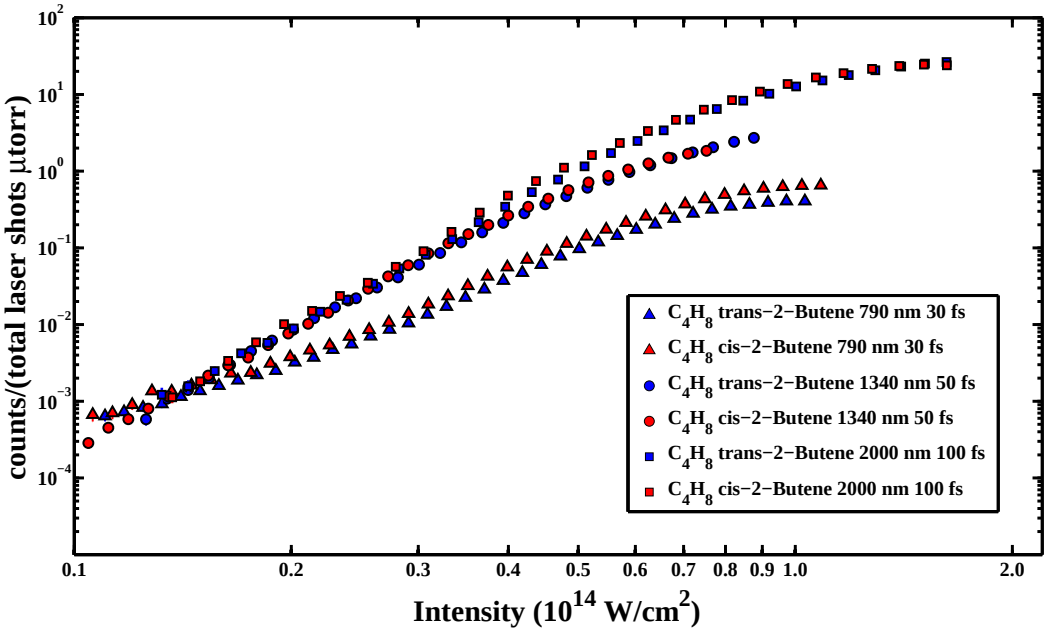

Figure 6.7: The pressure corrected ionization yield of the parent ion of C_4H_8 as a function of intensity. Three different pulse conditions are presented in the graph: (Triangle, 790 nm, 30 fs), (Circle, 1340 nm, 50 fs), and (Square, 2000 nm, 100 fs). Samples: C_4H_8: *trans*-2-butene (blue) and *cis*-2-butene (red).

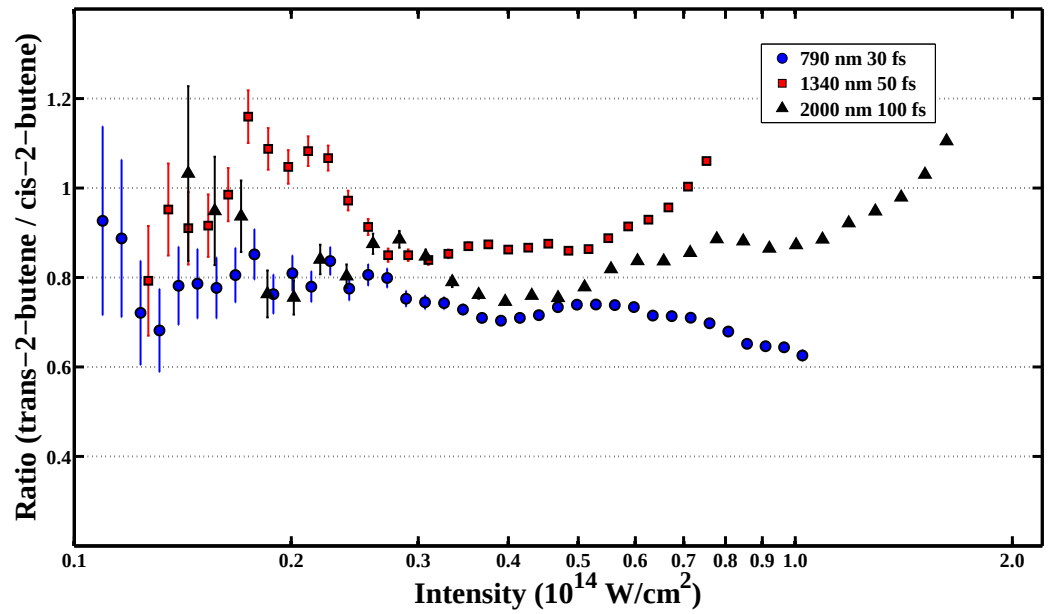

Figure 6.8: The ratio of the pressure corrected ionization yield of the parent ion of C_4H_8, *trans*-2-butene / *cis*-2-butene. Three different pulse conditions are presented in the graph: (blue, circle, 790 nm, 30 fs), (red, square, 1340 nm, 50 fs), and (black, triangle, 2000 nm, 100 fs).

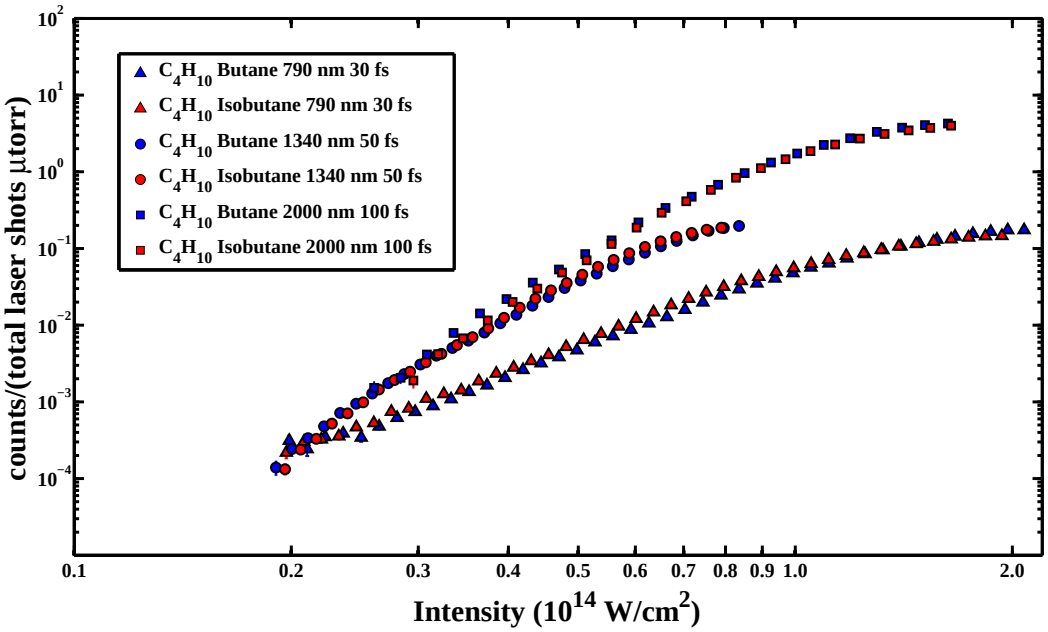

Figure 6.9: The pressure corrected ionization yield of the parent ion of C_4H_{10} as a function of intensity. Three different pulse conditions are presented in the graph: (Triangle, 790 nm, 30 fs), (Circle, 1340 nm, 50 fs), and (Square, 2000 nm, 100 fs). Samples: C_4H_{10}: butane (blue) and isobutane (red).

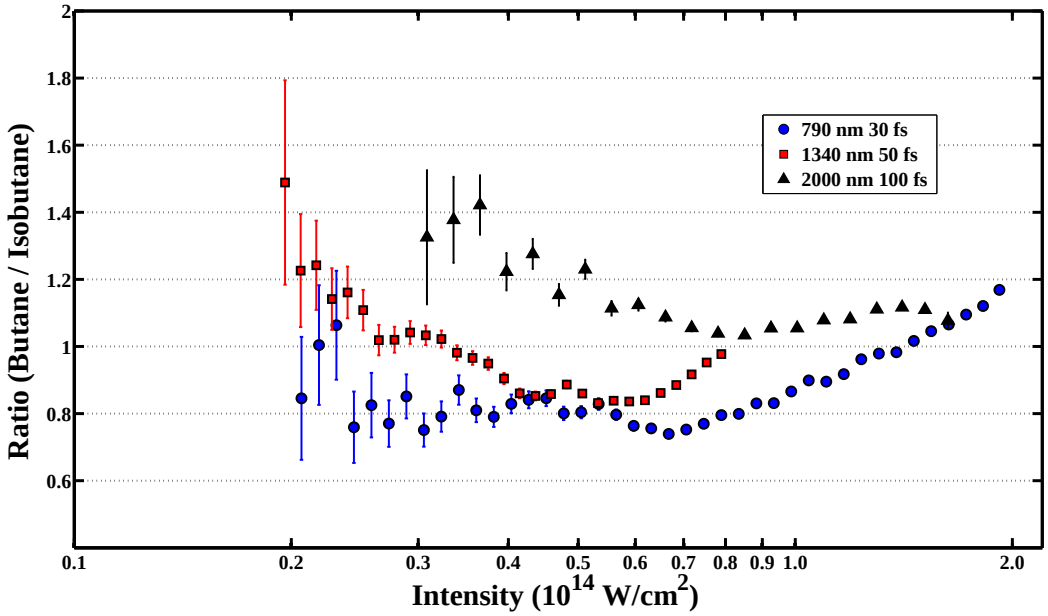

Figure 6.10: The ratio of the pressure corrected ionization yield of the parent ion of C_4H_{10}, butane / isobutane. Three different pulse conditions are presented in the graph: (blue, circle, 790 nm, 30 fs), (red, square, 1340 nm, 50 fs), and (black, triangle, 2000 nm, 100 fs).

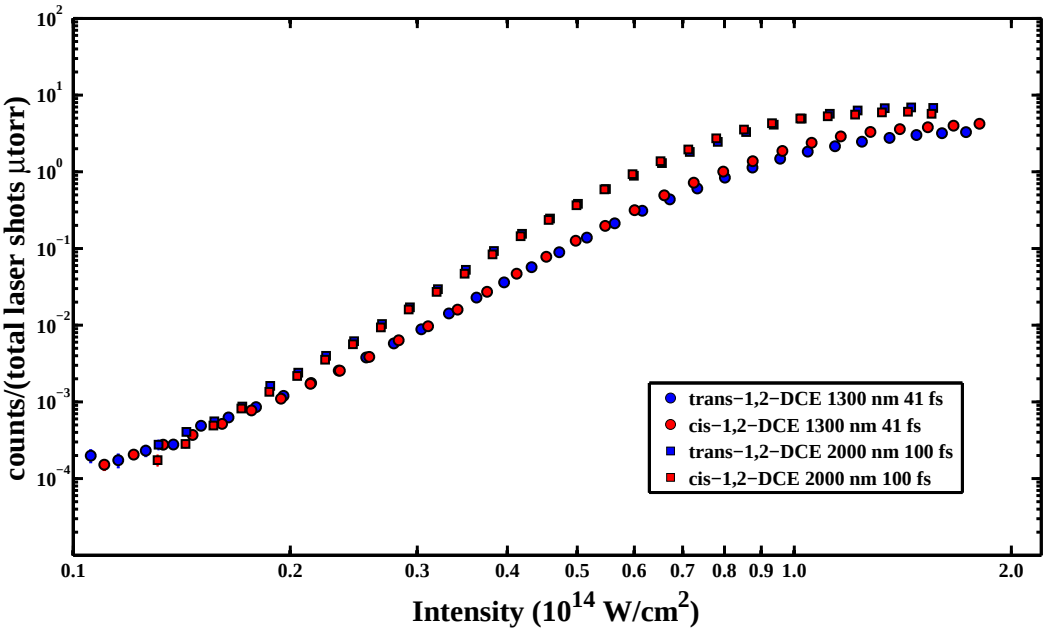

Figure 6.11: The pressure corrected ionization yield of the parent ion of $C_2H_2Cl_2$ as a function of intensity. Two different pulse conditions are presented in the graph: (Circle, 1300 nm, 41 fs), and (Square, 2000 nm, 100 fs). Samples: $C_2H_2Cl_2$: *trans*-1,2-DCE (blue) and *cis*-1,2-DCE (red).

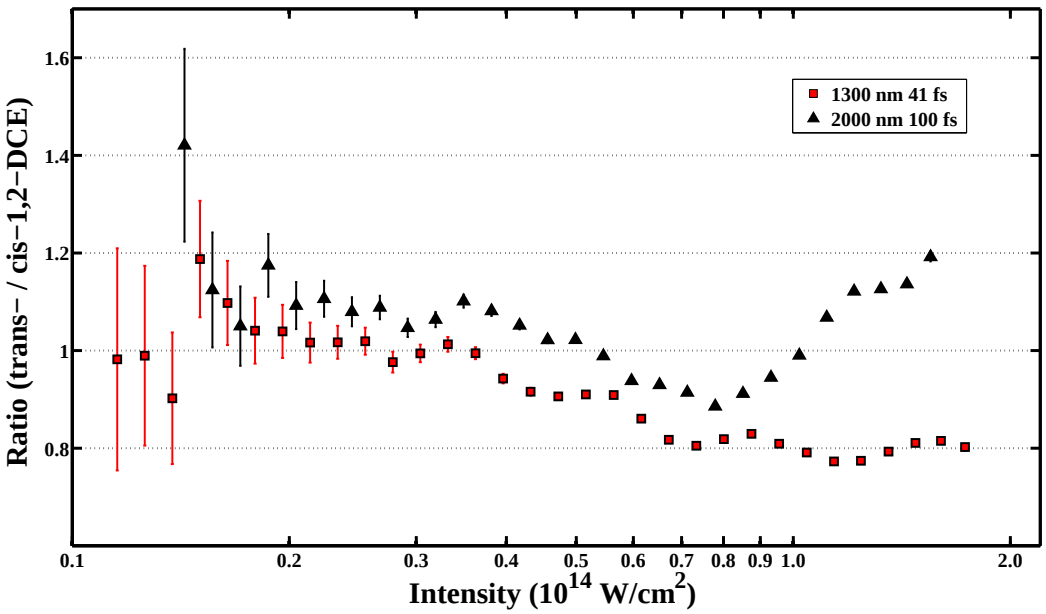

Figure 6.12: The ratio of the pressure corrected ionization yield of the parent ion of $C_2H_2Cl_2$, *trans*-1,2-DCE / *cis*-1,2-DCE. Two different pulse conditions are presented in the graph: (red, square, 1300 nm, 41 fs), and (black, triangle, 2000 nm, 100 fs).

$C_2H_2Cl_2$: *trans*- and *cis*-1,2-dichloroethylene

Next, we investigate $C_2H_2Cl_2$. For 1300 nm, the intensity range for *trans*-1,2-dichloroethylene is 0.11 - 0.3 $\times$ 10^{14} W/cm^2, see Fig. 6.11. Similarly, for 2000 nm, the intensity range is 0.14 - 0.35 $\times$ 10^{14} W/cm^2. Additionally, now looking at *cis*-1,2-dichloroethylene, see Fig 6.11, for 1300 nm the intensity range is 0.11 - 0.35 $\times$ 10^{14} W/cm^2, and for 2000 nm, 0.14 - 0.3 $\times$ 10^{14} W/cm^2. In Fig 6.12 we compare the ionization yields of the parent ion of both $C_2H_2Cl_2$ isomers by plotting the ratio *trans*- / *cis*-1,2-dichloroethylene as a function of intensity. For 1300 nm, the ratio is roughly 1.1 - 1.4 before fragmentation, and for 2000 nm, it is 0.9 - 1.2. This pair has a ΔI_p on the order of 0.01 eV. As a result, we would expect the ionization yields to be close to unity, which is what is observed at 1300 nm. There is a slight shift to a more dominant trans-isomer at 2000 nm. Looking back at chapter 5 in Fig. 5.9, we concluded that the trans-isomer was also dominating at 790 nm (ratio $\sim$ 1.4). Although it was technically under different experimental conditions, it is still valid to make the comparison.

6.3.2 Summary and Discussion

In this chapter, we presented the results of strong-field ionization experiments on 4 different pairs of isomeric molecules in the wavelength range of 790 - 2000 nm. We have successfully measured the single ionization yields, before fragmentation or saturation, of the parent ions of each of the molecules as a function of intensity. As a result, we have generated new markers to be used in consideration for the comparison or advancement of current molecular ionization theories.

One of the main conclusions of the experiment discussed in chapter 5 was that the differences in ionization yield of the isomeric pairs of 2-butene and 1,2-DCE were not comparable to the measured HHG yields of the same molecular pairs measured in Wong *et al.* [41, 42]. One of the unanswered questions from that study was the wavelength dependence of the ionization yields. It was suggested that the since the angular distributions of the electron are similar in the range 800 - 1500 nm, there should not be a large difference in the ionization

yields. In the experiments shown in this chapter, 790 - 2000 nm, we found this to be the case for 1,2-DCE and 2-butene. The changes in the ionization ratios were a maximum of 0.4 in favor of the *trans*-isomer at around 0.2×10^{14} W/cm^2, but for different wavelengths, 790 nm for 1,2-DCE and 1340 nm for 2-butene. The wavelength dependent change for a single wavelength rather than a gradual change through the full wavelength range suggests there might be some other mechanism involved, such as a resonance effect.

Continuing the discussion of wavelength dependence in the ionization yield ratios of isomeric molecules, we see that in the case of C_4H_6, there is a similar change in the ionization ratio to 1,2-DCE and 2-butene ($\sim$ 0.4) for a single wavelength, 2000 nm, in favor of 1,3-butadiene. It would appear that the wavelength dependent changes in the ionization yield ratio is independent of the common ratio values, $\sim$ 0.8 for 2-butene, $\sim$ 1.1 for 1,2-DCE, and $\sim$ 2.5 for C_4H_6. Focusing on the isomer type differences, stereo vs. structural, recall section 5.1, the wavelength dependent changes might not be influenced by the bond differences in a molecule. In the case of C_4H_{10}, there appears to be a transition of favor for butane as the photon energy decreases, however, due to the concerns of fragmentation at the lowest intensities of the measurement, further investigation is required.

In the stereoisomers studied, 1,2-DCE and 2-butene, the ionization potential differences, ΔI_p, were on the order of 0.01 eV. This led to the conclusion in chapter 5 that in the case of small ΔI_p, significant differences in the ionization yields of the isomeric pairs are present, therefore, strong-field ionization is not only influenced by its ionization potential. To compliment this statement, the ionization yield ratio of C_4H_6, with a ΔI_p on the order of 1 eV, is in the range of 2.5 - 3. The dominant isomer is 1,3-butadiene which has the lower I_p of the two. In this case, we suggest that the influence of ionization potential on the strong-field ionization yield is quite powerful and if the difference is large enough, it will mask the influence of other possible effects, such as multi-photon resonance effects or molecular polarity. Since the ground state energy of a molecule is heavily determined by the geometric structure of a molecule, we claim that based on our measurements, structural/bond type changes compared to simple bond rearrangement can have large influences on the strong-field ionization yield of a molecule. In order to strengthen this claim, we have performed

an experiment in the weak field limit, where single photon ionization occurs and ionization yields are mainly dependent on the photoionization cross-section, see chapter 7.

As a closing remark for this set of experiments presented in this chapter, the strong-field single ionization of molecules as a function of intensity is a complex problem. The experimental trends are easily influenced by fundamental properties of each molecular system. As a result, one of the main limitations of the measurements presented was the influence of the fragmentation of molecules at high intensities. In order to study strong-field ionization beyond this limit, other experimental techniques and measurements will have to be explored beyond ion-TOFMS.

Chapter 7

Ionization Study of Isomeric Molecules in the Weak-field Limit

7.1 Introduction

Thus far, we have introduced ionization studies in the strong-field limit only. The motivation derived itself originally as a comparison to large experimental higher-order harmonic generation (HHG) yield discrepancies between molecular isomer pairs. HHG is a strong-field effect based on both ionization and electron recombination. Therefore, it is only natural to study the strong-field ionization of molecular isomers directly. As was concluded in the chapters 5 and 6, depending on the molecules being studied, the differences between the strong-field ionization yields of the parent ions of isomeric pairs can be as great as a factor of 3.5. This begs the question, are the differences in ionization yield purely a consequence of being in the strong-field limit?

We answer this question by performing ionization experiments in the weak-field limit. In this chapter, we measure the total ionization yields of the same hydrocarbon isomeric pairs from earlier in this thesis, Fig. 6.4(c)-(h), as a function of photon energy. This is photoionization with VUV radiation produced from a synchrotron source. Although the comparison is not direct with total ionization yield (weak-field limit) vs parent ion yield

(strong-field limit), the results give insight into the differences between the two limits.

7.2 Experimental Configurations and Details

The experiments were performed at beamline 10.0.1.3 of the Advanced Light Source (ALS), a synchrotron facility at Lawrence Berkeley National Laboratory (LBNL). Although the ALS is capable of producing photons deep in the XUV, our experiments were limited to the photon energy range of 20 - 45 eV (62 - 27.5 nm) with a bandwidth on the order of 10 meV, ensuring that our studies remain in the valence orbitals of our molecular targets. Fig. 7.1 shows a diagram of the XUV beam path. The beam is focused through an entrance slit and the photon energy is chosen through the use of a grating. The beam profile and flux are controlled by the entrance slit before the grating and an exit slit after the grating with openings on the order of a few microns. Each slit opening remained constant for the duration of the experiment.

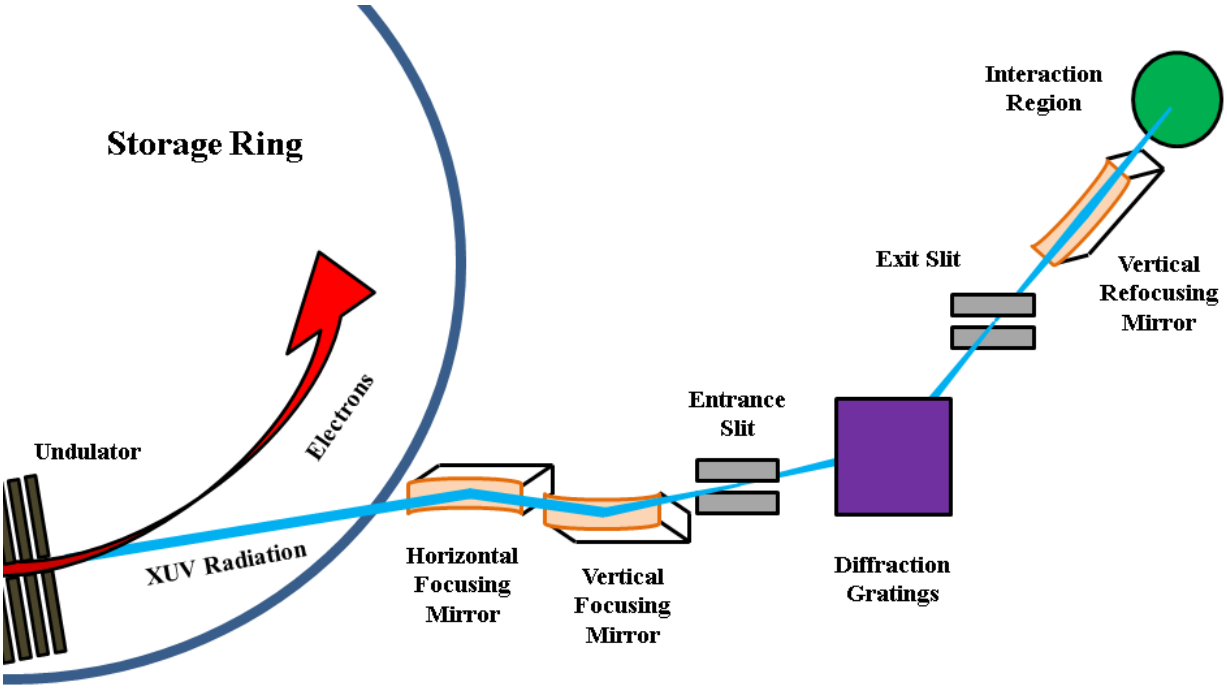

Figure 7.1: Diagram of Beamline 10.0.1.3 at Lawrence Berkeley National Laboratory's Advanced Light Source.

After the exit slit, the beam is loosely refocused into the interaction region of a double-sided velocity map imaging (VMI) spectrometer. See Fig. 7.2 for a visualization of the experimental setup and VMI spectrometer. Gas phase samples are ionized and the resulting ions and electrons are detected by two pairs of microchannel plate detectors (MCP's) and delayline detectors. The signals are processed by a constant fraction discriminator (CFD) and recorded by a multi-hit time-to-digital converter (TDC) as described in U. Ablikim *et al.* [83]. The arrival time of the ions are determined by the arrival of the first electron of each event which allows for the identification of each ion based on its mass and charge. Data is collected for a predetermined amount of time and the total ion count is recorded.

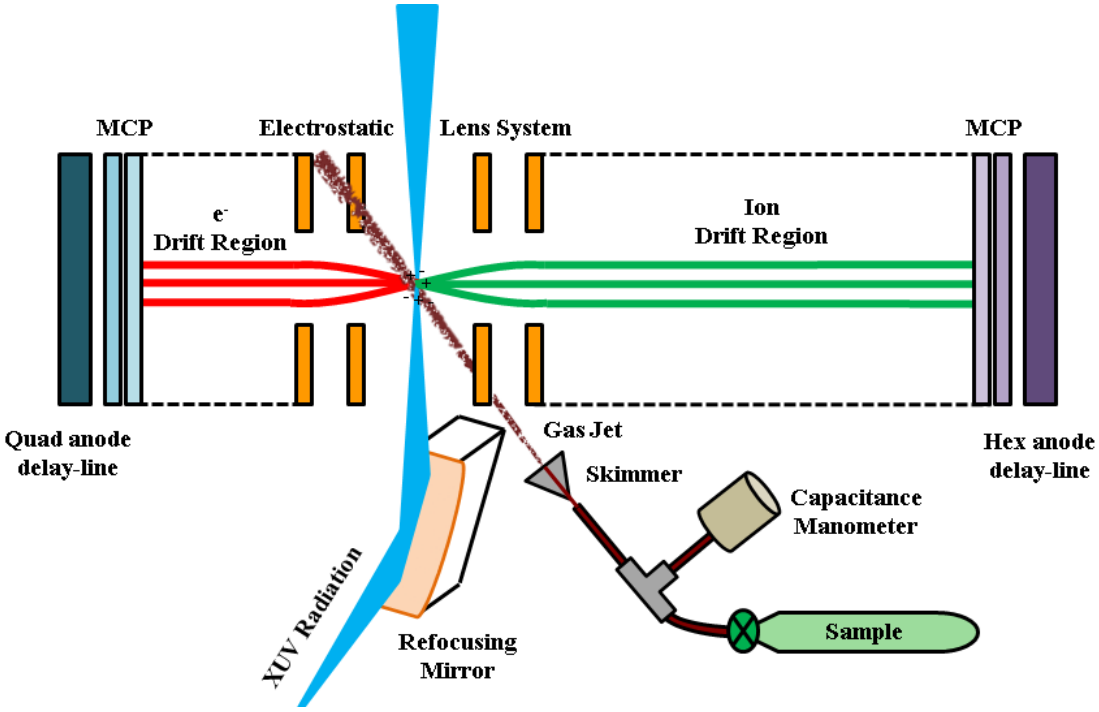

Figure 7.2: The experimental setup for the ionization experiments in the weak-field limit, featuring a double-sided VMI spectrometer.

The gas samples are introduced through a gas line with a 500 micron skimmer entering the main vacuum chamber, the location of the interaction region. The density of the resulting gas jet after the skimmer may not be accurately reflected by the main chamber hot-cathode BAG ionization gauge. Since the absolute density is not important for our measurement, but rather, the changes over time, we monitor the pressure of the gas line, before the skimmer,

more reliably than in the main chamber. The pressure of the gas line is directly proportional to the density of the resulting gas jet. The pressure is monitored using an MKS Baratron capacitance manometer with a resolution of 0.1 mtorr in a range of 0.1 - 1000 mtorr. The main advantage to using a capacitance manometer is that it is gas independent, which is ideal for the comparison between different isomers.

Contrasting with the strong-field experiments, where the intensity of the light in the interaction region can have non-linear effects on the ionization yield, in the weak-field limit, the intensity of the XUV light has a linear effect on the ionization yield. In order to have a reference of the fluctuations of the flux of the XUV light as a function of time, neon is introduced to the main vacuum chamber through a separate leak-valve from the main gas jet resulting in a mixed gas sample of neon and isomer in the interaction region of the spectrometer. The neon pressure is maintained at a constant value for the duration of the measurements. The ionization yield of Ne^+ is collected simultaneously with the rest of the ions related to the samples of interest. The total ionization yield of the neon is used as a normalization value to correct for intensity fluctuations during the experiments. The photoionization cross-section of neon changes as a function of photon energy in the XUV, therefore, we correct the neon yield by dividing by the cross-section. The values used were, in units of cross-section / Mb, roughly 5.9, 7.83, 8.85, 8.93, 8.68, and 8.27 for 20, 25, 30, 35, 40, and 45 eV photons, respectively. Cross-section values were found in ref. [48].

For the following experiments, we focus only on the hydrocarbons, C_4H_6, C_4H_8, and C_4H_{10}, resulting in the isomer pairs, 1,3-butadiene and 1-butyne, *cis*- and *trans*-2-butene, and butane and isobutane, respectively. The details of the samples are presented in sections 5.2.3 and 6.2.2.

7.3 Results and Discussion

7.3.1 Experimental Results

We study the trends of single photon ionization as a function of photon energy on three different pairs of isomeric molecules. The total pressure and neon yield corrected ionization yields and the ratios of those yield pairs are plotted in Fig. 7.3, 7.4, and 7.5. All of the molecules were studied under identical experimental conditions in the photon energy range of 20 - 45 eV in steps of 5 eV. This energy range is above the carbon K-edge and all ionization electrons are valence electrons. Note that each yield measurement was taken over a 5 minute interval. The error reported is a propagation of error of the yield counting statistics error, pressure standard deviation error, and neon yield counting statistics error. In terms of the yield counting error, the number of counts increased as the photon energy increased.

For all three pairs of isomers, we find their pressure and neon yield corrected total ionization yield ratios to be close to 1 (within 20%), which is what we would expect considering the compositional similarities, however, the structures in each pair do differ and we do see that one molecule is almost always favored in each pair within the error of the measurement. First we investigate C_4H_6. The yield ratio, 1,3-butadiene / 1-butyne, (Fig. 7.3b), is in the range 1.0 - 1.1. Within the error of the measurement, neither isomer dominates. For C_4H_8, the yield ratio, *trans*-2-butene / *cis*-2-butene, (Fig. 7.4b), is in the range 0.95 - 1.12. Within the error of the measurement, the *trans*-isomer dominates. Finally we investigate C_4H_{10} and the yield ratio, butane / isobutane, (Fig. 7.5b), is in the range 0.85 - 0.98. Within the error of the measurement, the ratio increases as a function of increasing photon energy with isobutane as the dominant isomer, but it comes closer to unity at the high end of the energy range.

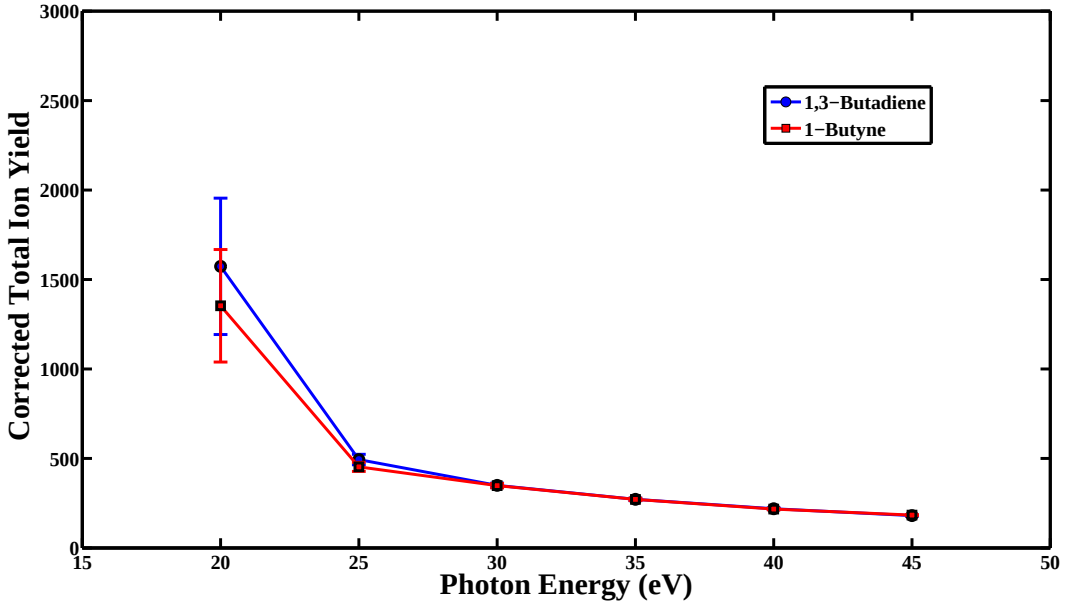

(a) The pressure and neon yield corrected total ionization yield of C_4H_6 as a function of photon energy. Samples: C_4H_6: 1,3-butadiene (blue circles) and 1-butyne (red squares).

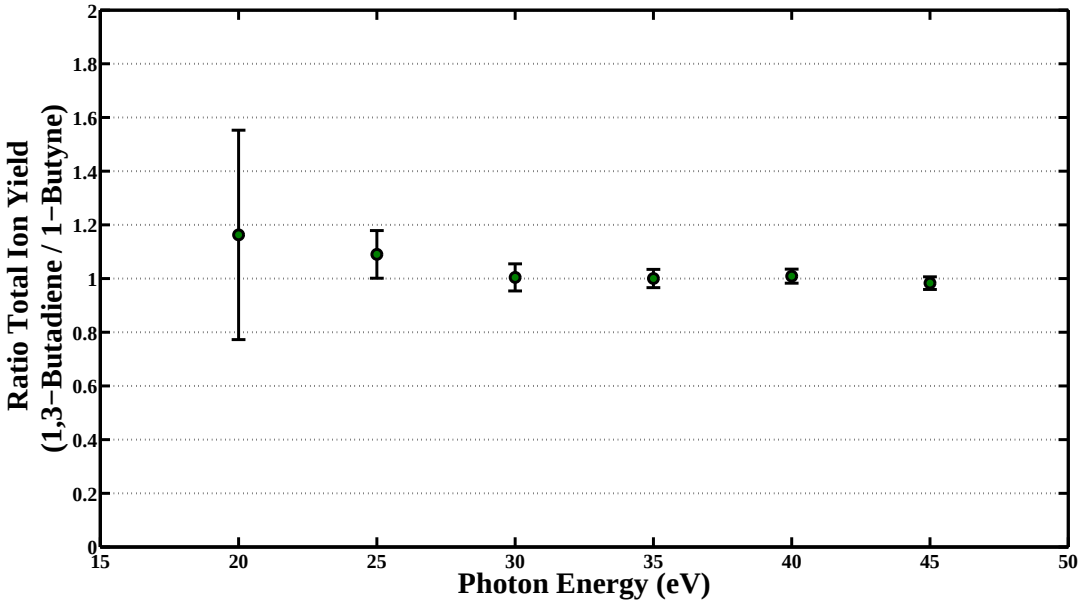

(b) The ratio of the pressure and neon yield corrected total ionization yield of C_4H_6 (1,3-butadiene / 1-butyne) as a function of photon energy.

Figure 7.3: The total ionization yields of C_4H_6 and their ratio.

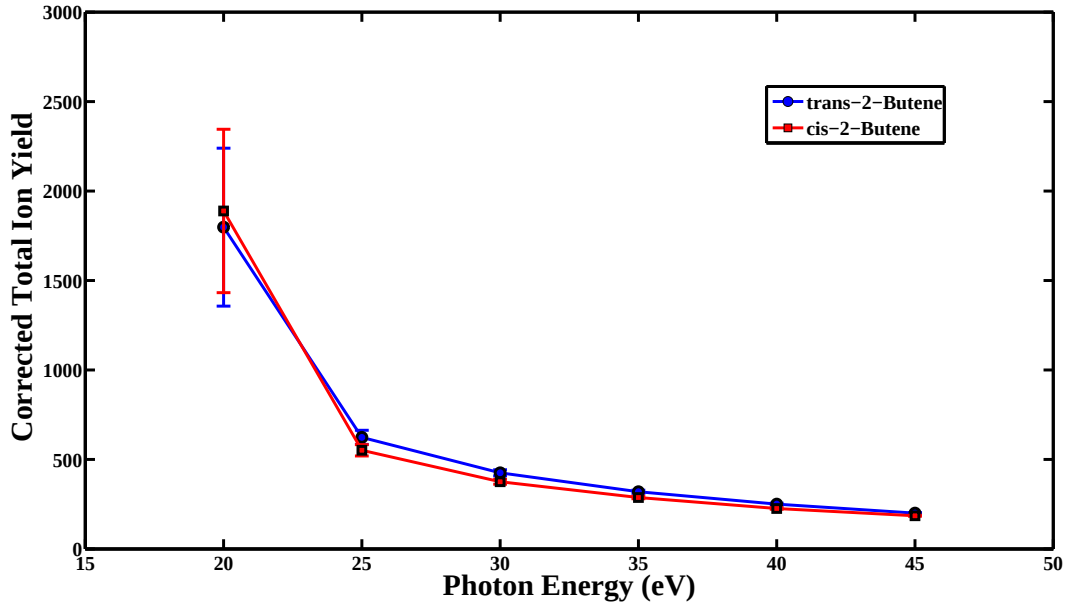

(a) The pressure and neon yield corrected total ionization yield of C_4H_8 as a function of photon energy. Samples: C_4H_8: *trans*-2-butene (blue circles) and *cis*-2-butene (red squares).

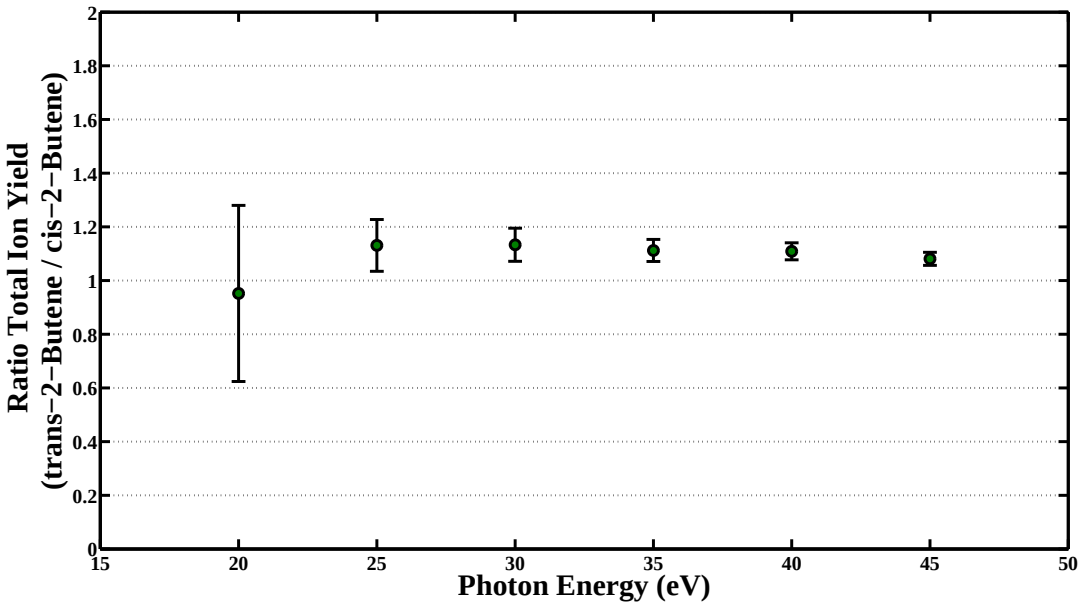

(b) The ratio of the pressure and neon yield corrected total ionization yield of C_4H_8 (*trans*-2-butene / *cis*-2-butene) as a function of photon energy.

Figure 7.4: The total ionization yields of C_4H_8 and their ratio.

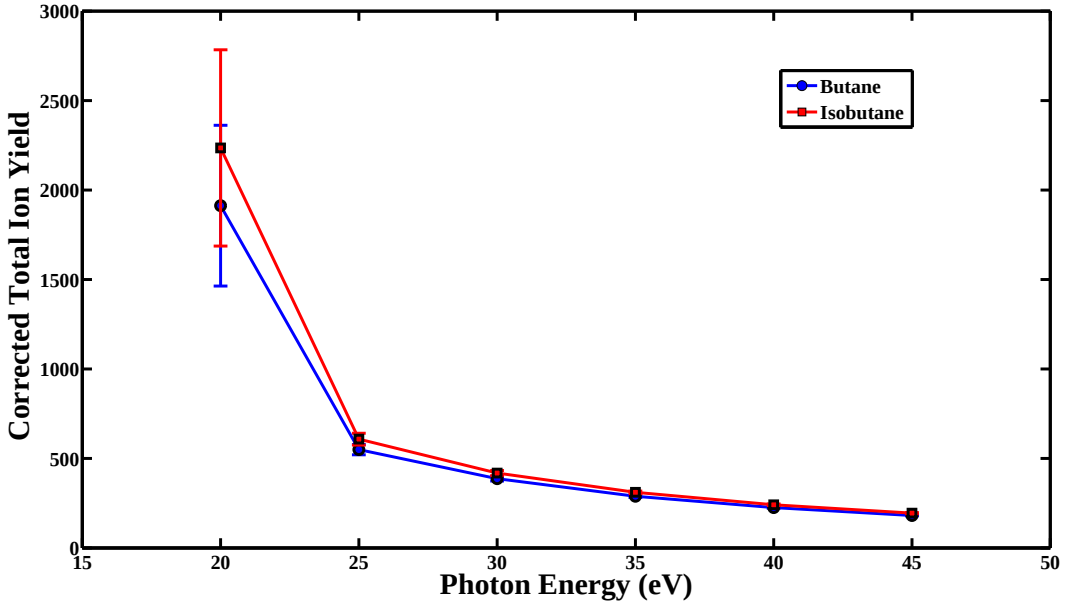

(a) The pressure and neon yield corrected total ionization yield of C_4H_{10} as a function of photon energy. Samples: C_4H_{10}: butane (blue circles) and isobutane (red squares).

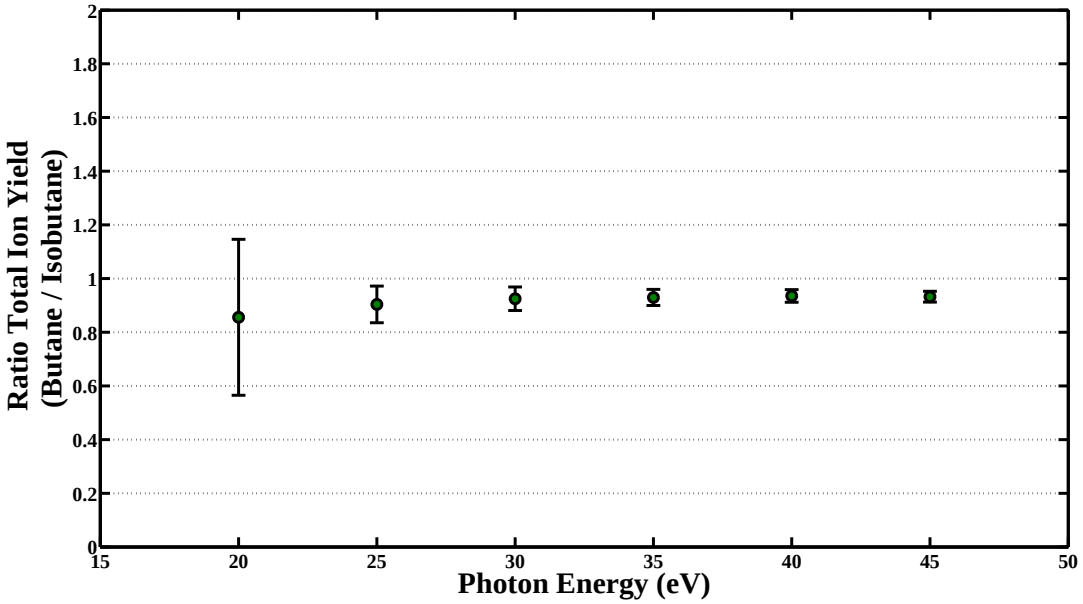

(b) The ratio of the pressure and neon yield corrected total ionization yield of C_4H_{10} (butane / isobutane) as a function of photon energy.

Figure 7.5: The total ionization yields of C_4H_{10} and their ratio.

7.4 Summary, Discussion, and Outlook

In this chapter, we measured the total ionization yield of three pairs of isomeric molecules in the weak-field limit. Overall, we see relatively flat ratios as a function of photon energy for all isomer pairs studied. Between the two different pairs with discernable ionization potential differences, C_4H_8 and C_4H_{10}, there is no trend as to whether the molecule with lower ionization potential always dominates the molecule with the higher. This is expected since we are in the weak-field limit where single photon ionization occurs. The targets are not susceptible to intermediate excitation states since all photon energies are above the molecular ionization potentials of the molecules studied in this paper.

By measuring the total ionization yield, we see that the photoionization cross-sections of the isomeric pairs are similar to each other. This indicates that measurements concerning the differences of similarly composed molecules are not as sensitive as the measurements made in the strong-field limit. Although we do not claim a direct comparison to the results of the experiments in chapters 5 and 6, since the measurements are different, total vs. parent ion yield, the strong-field measurements are influenced greater by the photon energy and ground-states of the molecules studied.

The experiments performed in this chapter were a collaboration between the research groups of Daniel Rolles and Carlos Trallero of Kansas State University. Although the author of this thesis was the project lead, the experiment would not have been successful without the help of U. Ablikim, S. Augustin, B. Kaderiya, R. Obaid, I. Dumitriu, K. Schnorr, T. Osipov, D. Rolles, and C. A. Trallero-Herrero.

The measurements presented in this chapter are considered complete. The total ionization yield ratios were statistically significant enough to answer our questions regarding the differences between weak- and strong-field photoionization. With that said, there are still plenty of interesting phenomena to look into regarding weak-field spectroscopy of isomeric molecules. Most notably would be to look at and compare the different break-up channels of each isomeric pair as a function of photon energy. Similar work has already been investigated by U. Ablikim *et al.* [83].

Chapter 8

Outlook and Other Research Project Results

In this chapter, we discuss the current works in progress that the author of this thesis was either a project lead or a strong collaborator. In the following sections, each project will be introduced and the main contributions of the thesis author will be highlighted.

Maintaining the theme of the study of isomeric molecules in the strong-field limit, in this chapter, we touch on three different extensions of the strong-field ionization experiments shown in previous chapters, first of which is the extension into photoelectron spectroscopy. A velocity map imaging (VMI) spectrometer can be used to better understand the energy structures of the isometric molecules through the use of a NIR pump - XUV probe technique. Second, we extend our wavelength-dependent studies further into the IR. By generating femtosecond pulses in the long-wave infrared (LWIR), and achieving intensities in the high 10^{13} W/cm^2, strong-field ionization yields can be compared between isomeric molecules as demonstrated previously in this thesis. The push into the LWIR ensures the systems are in the pure tunneling regime. Finally, we return to the capabilities of HITS and describe its carrier envelope phase (CEP) locking feature and its future use in few-cycle, CEP dependent experiments.

8.1 Strong-field Photoelectron Spectroscopy

In this section, we present preliminary construction of detection equipment and experimental techniques to be used in future strong-field spectroscopy experiments. Complementing our previous experiments, chapters 5, 6, and 7, where only ion yields were measured, the measurement of photoelectrons will give insight into the energy structure of the molecular systems. In addition, using the short time duration of the laser pulses as an ultra-fast "camera shutter", we can look at the photoelectrons as a function of delay from initial excitation, giving insight into the dynamics of the molecular systems.

8.1.1 Velocity Map Imaging Spectrometer

The velocity map imaging (VMI) spectrometer was constructed to be used to measure the photoelectron spectra of atoms and molecules. The original design is described in Kling *et al.* [84] and termed a "thick lens" VMI (TL-VMI). This particular design, with -10 keV repeller voltage, can accommodate up to 360 eV electrons with a calculated resolution, $\Delta E/E$, of $\gtrsim 1\%$. The original parts were ordered and organized by Felix Spitzer. The complete construction, and any modifications thereafter, were performed and planned by the author of this thesis. A 3D model of the spectrometer can be found in Fig. 8.1, provided by Al Rankin.

8.1.2 Modifications and Current Status

Imaging Detector

After construction, the VMI spectrometer was tested using the 790 nm output of HITS with a transform limited pulse duration of ~ 30 fs. The light was focused into the interaction region of the VMI using a 2", 50 cm plano-convex lens. The test gas was argon. As described in section 2.1.1, a common consequence of multiphoton ionization is above-threshold ionization (ATI). A VMI can be used to resolve the different energy separated electrons emitted during the ATI process. In Fig. 8.2, preliminary results are shown of the 2D projection of the 3D

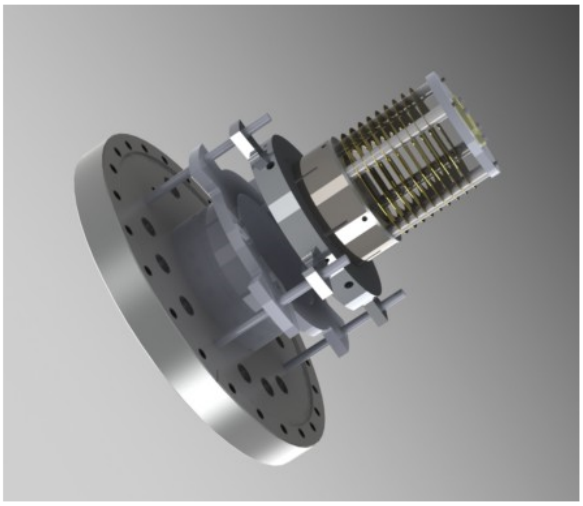

Figure 8.1: Thick lens VMI spectrometer.

momentum distribution of the photoelectrons in the strong-field limit.

The asymmetric shape and uneven distribution of yield in the preliminary results is primarily due to the use of an old MCP and phosphor screen taken from another experimental setup. The inefficient regions of the detector are vertical stripes spread out perpendicular to the laser polarization access. New MCP plates and a phosphor screen were purchased to replace the old detector. They were installed and the VMI is ready for further testing.

Lens Voltage Control and Optimization

The VMI design was modified from its original design. The lens system is composed of 9 different electrostatic lenses and a repeller, schematic shown in Fig 8.3(a). Lenses 3-9 are usually connected in vacuum with resistors in series to form a voltage dividing circuit. There are equal potential drops starting from the voltage on lens 3 to ground on lens 9. In our design, however, we have individual external control of each of the electrostatic lenses.

Although the original design is well characterized using the charged particle flight simulator, SIMION (version 8, Scientific Instrument Services)[85], we anticipate that small correc-

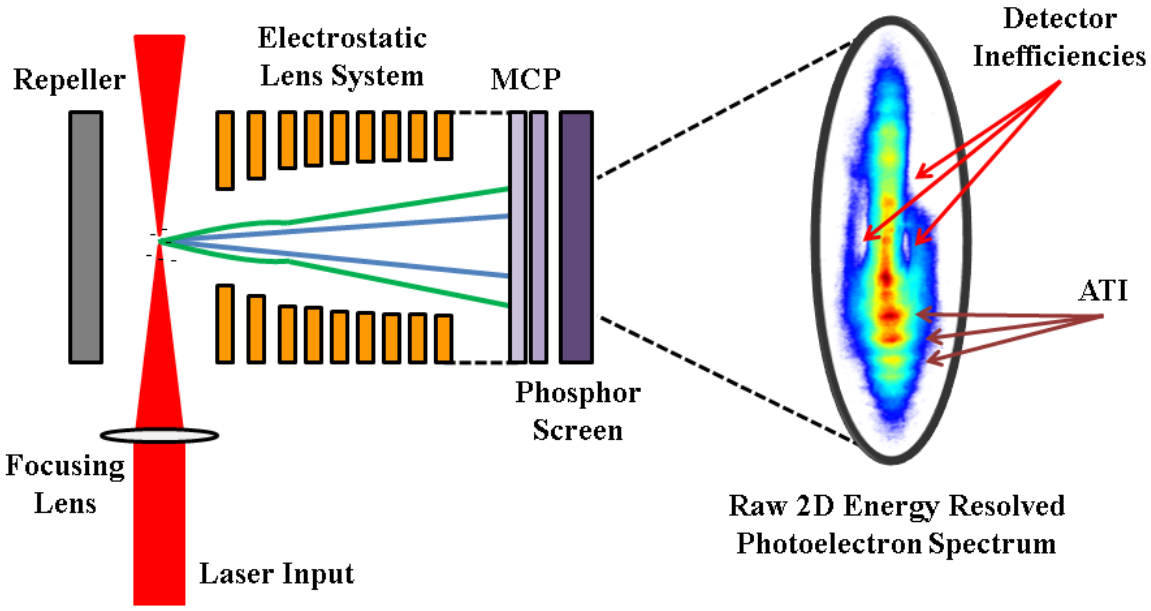

Figure 8.2: Preliminary results showing the measured photoelectron spectrum of argon in an intensity regime where ATI occurs.

tions to each lens potential might determine an overall lens configuration that promotes the best electron energy resolution possible. Taking a theoretical/simulation approach, we have written a simple sequential search algorithm, to be used in SIMION, that cycles through a series of predetermined lens configurations looking for the one that minimizes the variance of a group of flown, energy identical particles on the detector, i.e. minimizing the energy resolution of that group of particles. The code is written in the programming language LUA, however it is read and incorporated with the SIMION software. A sample of the program can be found in appendix A.5.

As an example, we flew 2 groups of 30 particles with a cross pattern spread evenly over ±1 mm about the interaction region, Fig. 8.3(b). The initial electron energies for each group were 3 and 20 eV all with a starting momentum parallel to the MCP detector (up in Fig. 8.3). A fixed repeller voltage (-1000 V) was applied and 3 lenses (V1, V2, V3) were varied sequentially. The following step sizes and ranges were used for the voltages of the three lenses: V1, V2: 1000 - 800 V with 20 V step size and V3: 1000 - 0 V with 100 V step

size. In this example, we also employ the use of a voltage divider for the remaining lenses (4 - 9) based on the voltage applied to lens 3. After the initial optimal voltage configuration was determined, an additional search was implemented with 100 V ranges, centered on the original results. All step sizes were changed to 2 V. It should be noted that the program is scalable and the use of only 3 variable lenses was to save on calculation time. In general, sequential search algorithms scale poorly with increased number of free variables. In the future, the use of more sophisticated search algorithms should be used, such as a genetic algorithm [86] which is best used for systems with a large phase space. In Fig. 8.3, we see the results of the simulation. With the following "standard" voltage configuration, V0: -1000 V, V1: -933 V, V2: -866 V, V3: -800 V, we obtain an average variance of the two energies of 0.0008293. After the sequential search, the best voltage configuration was found, V0: -1000 V, V1: -960 V, V2: -820 V, V3: -800 V, shown in Fig. 8.3(a) with variance of 0.0007576.

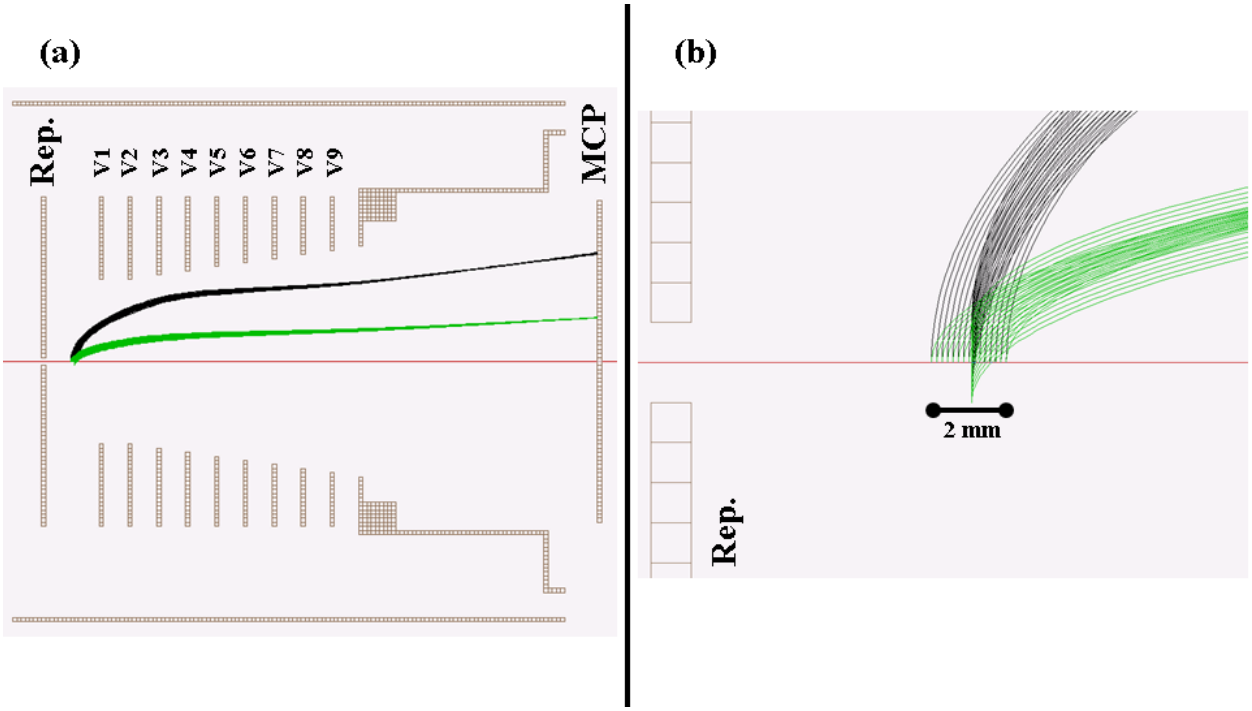

Figure 8.3: (a) SIMION simulation of minimization of electron energy resolution through the use of a sequential search algorithm. (b) Initial flight conditions: Cross pattern 2 x 2 mm, 3 eV (green) and 20 eV (black) parallel to the detector surface.

The SIMION simulations are proof of concept. We anticipate unique experimental issues in the real VMI where user errors are prevalent. By having control of the entire array of

lenses, similar search techniques can be tested in a real experiment. Of course, dynamic equipment errors, such as laser energy fluctuations, must be accounted for. This makes the real application much more complicated. As a continuation of the optimization techniques shown here, extension into optimization of electron energy resolution in time-of-flight experiments was discussed in the master's thesis of Pratap Timilsina (Kansas State University 2016).

In the simulations, the initial momentum conditions of the flown electrons were chosen such that they represent the momentum distribution only parallel to the MCP detector. The VMI spectrometer essentially projects the 3D momentum distribution onto a 2D plane. The prepared electrons, parallel to the detector, are the same as a projection or simply a slice of the 3D distribution. In order to accurately simulate a real experiment, electrons would need to be flown in all directions, mimicking a real 3D momentum distribution. Under those conditions, the minimization of energy resolution is more appropriately handled after an Abel transformation of the 2D projected image measured by the spectrometer's detector. The 3D slice of the momentum distribution of an electron of single energy is what represents the true energy resolution of the spectrometer. The inversion process will not be explained in this thesis, however, a reference for a simple computational approach can be found in ref. [87] which uses the inversion approach known as pBasex.

8.1.3 Proposed NIR-XUV Pump-Probe Experiment and Outlook

Thus far, this thesis has introduced spectroscopic measurements that focus on structure rather than dynamics. The staple experiment for studying the dynamics of molecules with femtosecond laser pulses is one that utilizes the "pump-probe" technique. The basic idea is that a "pump" pulse dresses the system. This could be excitation of electronic, rotational, or vibrational states of a molecular system. Then, sometime later, after the system has had time to evolve, a "probe" pulse extracts an observable, usually a photoelectron. Although this "pump-probe" technique is utilized in all fields of laser spectroscopy, the advantage to using ultra-fast pulses is that information can be extracted faster than the time scale of the

dynamic that is being studied.

We propose that the NIR light sources described in this thesis be used to excite molecular systems and an XUV source be used to photoionize the molecules. Photoelectron spectra, measured with the VMI spectrometer described earlier, will be obtained as a function of delay between NIR and XUV pulses. In the context of the isomeric molecules studied in this thesis, the differences between ionization from the ground state and an excited state could be explored. Also, do we see similar differences between isomers? On a deeper level, if there is no difference, why? Is one isomer more susceptible to isomerization than the other, therefore, convoluting the comparison?

XUV Light Source

In addition to the continued testing of the VMI spectrometer, the generation of the XUV light will require development. As an outlook, there are two approaches that could be taken. The first would be to generate the 4th harmonic of the 800nm Ti:sapphire output, as a starting point. Starting with the fundamental, ω, this would require a series of nonlinear crystals to either mix two 2ω pulses or mix 3ω and the fundamental. Unfortunately, the 4th harmonic of 800 nm is only 200 nm, which equates to photons on the order of 6 eV, so a 2-photon transition in the best case scenario for the isomeric molecules we are studying.

Another approach is the use of the XUV output from the HHG process. In this case, we guarantee single photon ionization. The struggle, however, is to obtain sufficient flux of the generated XUV. It is the continued pursuit of the ultra-fast community to enhance the HHG yield output as much as possible. For our proposed experiments, the common approach is to use a semi-infinite gas cell to generate harmonics from the 800 nm Ti:sapphire output. Typically, however, the use of an aluminum filter is required to separate the 800 nm light from the XUV light. This results in significant losses of the XUV. In an attempt to circumvent the use of a physical filter, we propose the use of a self filtering optical technique. The use of a long focal length lens will be replaced by the combination of a lens and an axicon (a cone-shaped lens) to generate and focus bessel beams through a semi-infinite gas cell. The unique

focusing properties of an axicon generates low-order bessel modes in the near-field and high-order modes in the far-field. Essentially, the far-field mode is shaped like a doughnut. The majority of the energy is far from the center axis. Therefore, the beam is self filtering. The characterization of the focusing bessel modes generated from the lens-axicon combination with femtosecond laser pulses and the generation of harmonics from its combination is an active and ongoing research development project led by Adam Summers and Jan Troß. The author of this thesis contributed to the initial characterization studies published in Summers *et al.* [88].

8.2 Strong-field Ionization with Long-wave Infrared Femtosecond Laser Pulses

As described in chapter 6, the use of intense femtosecond laser pulses in the infrared for strong-field spectroscopic studies is a growing topic of interest. High pulse energy, NIR femtosecond light sources are becoming more common with the scalability of Ti:sapphire lasers to high energy output and OPA additions. Other laser systems, such as optical parametric chirp pulse amplified (OPCPA) lasers or high-energy fiber lasers can also be used to the same end.

Going further into the infrared, $\gtrsim 3\mu m$, while still maintaining short pulses and high energy output remains a challenge. In this section, an experimental collaboration is introduced between Carlos Trallero's and Artem Rudenko's research groups (Kansas State University). The goal of the experiment is to highlight a tunable laser source in the long-wave infrared (LWIR 5500 - 8500 nm) with enough energy to perform strong-field spectroscopy experiments. The development of the LWIR source was led by Derrek Wilson and the strong-field spectroscopy was led by the author of this thesis and Adam Summers.

8.2.1 Long-wave Infrared Source

The generation of the LWIR light is achieved through difference frequency generation (DFG) of the HITS OPA signal and idler light, introduced in section 3.1.2. Similar to the OPG process described in section 3.1.2, DFG is a nonlinear effect resultant of a 2 wave mixing process in a $\chi^{(2)}$ nonlinear medium. The energy conservation equation is $\omega_1 - \omega_2 = \omega_3$ where ω_1 is the frequency of the OPA signal and ω_2 is the frequency of the OPA idler. The two input sources propagate co-linearly for maximum spatial overlap through an uncoated $AgGaS_2$(I) crystal (Newlight Photonics, $1 \times 1 \times 0.1$cm). Temporal overlap of the signal and idler is performed by a micrometer driven manual linear translation stage which allows for a delay in time (on the fs level) to be introduced to one of the two OPA outputs. The tunability of the output is signal, 1360 - 1450 nm and idler 1900 - 1760 nm ($\sim$6 mJ combined input), resulting in 5.5 - 8.5 μm DFG output, 80 - 40μJ of pulse energy, respectively. Germanium is used as a filtering optic in order to eliminate any residual OPA light. The pulses were characterized using the cross-correlation FROG (XFROG) technique [89], not described in detail in this thesis, which is a similar technique to the standard SHG FROG from section 3.1.3; however, instead of self gating, a known pulse is used to gate the LWIR pulse. In our case, we use the HITS output, 790 nm, pulse as the gate. XFROG measurements retrieved a pulse duration of $\sim$80 fs. Additional and greater detail about the LWIR generation process will be covered in future publications, including the theses of Derrek Wilson and Adam Summers.

8.2.2 Preliminary Results: SFI of Noble Gases with LWIR

The ionization of inert atomic gases (noble gases) in the strong-field limit for Keldysh parameter, $\gamma \approx 1$, is relatively well understood theoretically and confirmed experimentally. This was discussed in chapter 2. It was also described that as the wavelength increases, γ decreases, and the system is dominated by tunneling ionization. In this subsection, we describe an experiment with two goals: i) Is the output of the LWIR source energetic enough to generate intensities required for strong-field ionization? and ii) Does the ionization yield

of the noble gases conform to the known theories of SFI in the tunneling regime?

Experimental Setup and Results

The ionization experiments were performed in a "thick lens" VMI spectrometer (provided by Artem Rudenko's group) in ion time-of-flight operation (2 kV repeller, 80 V on the voltage divided e-lens system). Note the design of the VMI is almost identical to the one described in section 8.1.1 which originated from [84]. The LWIR output was back focused in the interaction region of the spectrometer using a f = 5 cm silver coated concave mirror, resulting in intensities in the range of $10^{13} - 10^{14}$ W/cm^2 (determined through a spot size measurement). With a background pressure of 3×10^{-8} torr, gas samples were introduced to the vacuum system as an effusive jet with pressures on the order of 10^{-6} torr. TOF spectra were recorded using a fast oscilloscope, described in chapter 6.

The following gases were tested, Xe, Kr, Ar, Ne, and He, with corresponding ionization potentials of approximately 12.13, 14.00 , 15.76, 21.56, and 24.59 eV, respectively. Each gas was tested separately, but under the same laser conditions. Raw calibrated TOF traces are presented in Fig. 8.4(a). The integrated signal ionization yields of the parent ions of the noble gases is presented in Fig. 8.4(b). Each yield is normalized to the yield of Xe^+ and pressure corrected. From the TOF traces we conclude that at the maximum intensity achieved by the focusing LWIR source, we were able to at least singly ionize all of the samples tested. In addition, we identify up to Xe^{3+}, Kr^{2+}, Ar^{2+}, and Ne^{2+}.

Discussion

In terms of the goals of the experiment, we successfully ionized atomic samples in the strong-field limit using femtosecond pulses centered in the LWIR. This shows that strong-field spectroscopic studies can be performed with this particular light source. However, we question our preliminary results. If we assume tunneling ionization only, which should be a valid assumption when working with the LWIR, we can calculate the probability of ionization of the atomic samples using the ADK ionization model, see section 2.2.3, specifically equations

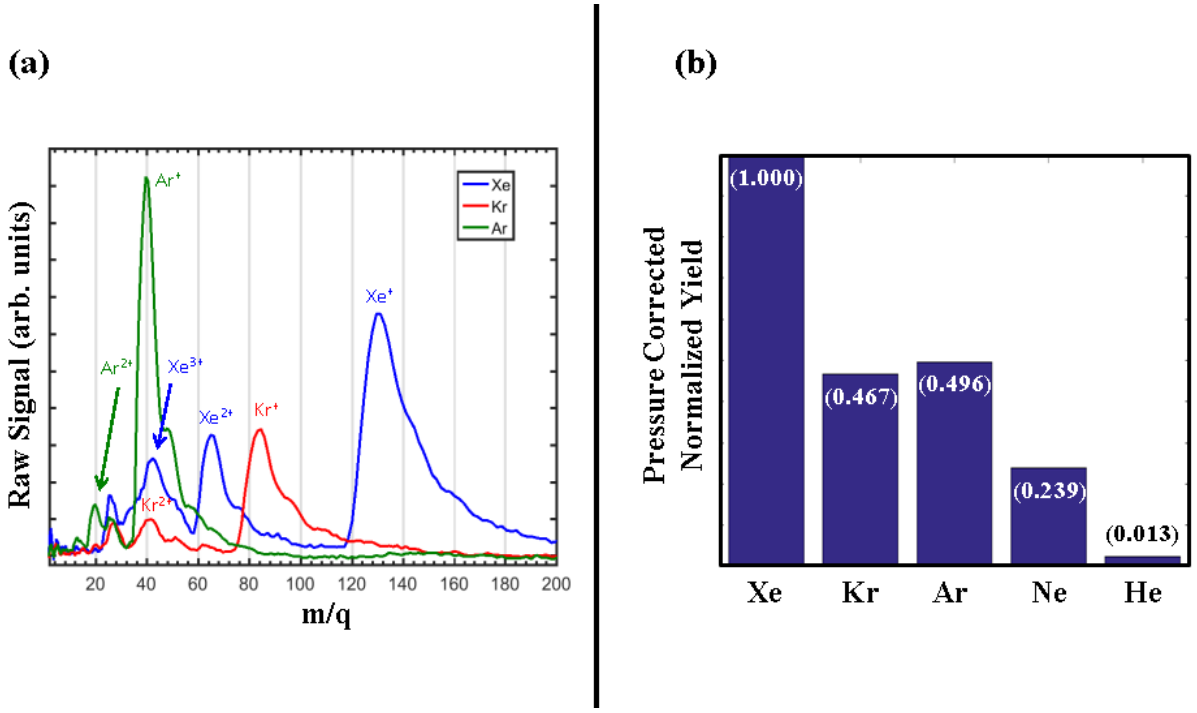

Figure 8.4: Preliminary results showing (a) the measured raw calibrated time-of-flight spectra of Xe, Kr, and Ar after being ionized by femtosecond pulses in the LWIR ($\sim 8.5\mu$m). (b) The pressure corrected integrated signal ionization yield of the parent ion of Xe, Kr, Ar, Ne, and He, normalized to the Xe yield.

(2.36) and (2.37). In Fig. 8.5, the probability of ionization of Xe, Kr, Ar, Ne, and He as a function of intensity is calculated using ADK and plotted with the pulse conditions of our experiment, 80 fs at 8.5μm. We see that the probability of ionization for Xe is 8 orders of magnitude higher than that of the He for an intensity of 10^{14} W/cm^2. This is not surprising considering the large difference in ionization potential, about 12.6 eV.

Since we do see the ionization of both Xe and He under the same experimental conditions, there must be some other physics at play, in addition to our naive tunneling only assumption. This suggests that the tunneling picture breaks down at high intensities in the LWIR. Furthermore, we measure multiple charge states of the noble gases despite its low probability of sequential tunnel ionization. This suggests that there may be other phenomena occurring, such as electron re-collision resulting in non-sequential ionization.

The experiment will be repeated in the future to confirm our observations.

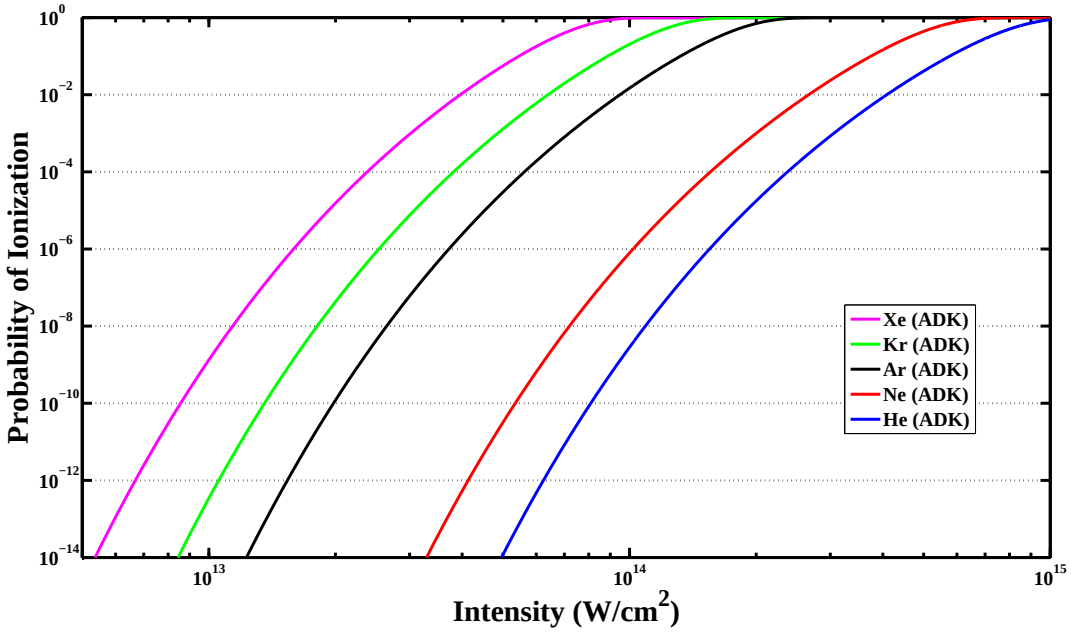

Figure 8.5: The calculated probability of single ionization of Xe, Kr, Ar, Ne, and He as a function of intensity using the ADK ionization model at 8.5μm with 80 fs pulse duration.

8.3 HITS Features: Carrier-envelope Phase Locking

As a continuation of chapter 3, we return to our discussion of the capabilities of the HITS laser. In addition to the 20 mJ output at 790 nm, it was shown in Langdon *et al.* [59] that the HITS laser can be carrier-envelope (CE) phase stabilized to a single-shot noise value of 300 mrad RMS over 9 hours, a time duration long enough to perform strong-field experiments. The CE phase is defined as the offset of the peak of the electric field oscillation with respect to the $t = 0$ pulse envelope. The CE phase of a laser pulse becomes important when working with few-cycle pulses, where changes to the electric field are more apparent. In general, having phase control allows for spectroscopic studies of phase dependent processes, which were theorized or observed in strong-field phenomena, such as photoionization, ATI, HHG, etc. [90–94] In addition, CE-phase control is essential for synthesizing new laser pulses with the ultimate goal of achieving sub-cycle waveforms [95].

8.3.1 Carrier-envelope Phase

The CE phase, ϕ_{CE}, appears in the equation for the electric field of a transform-limited laser pulse like so:

$$E(t) = E_0(t)\cos(\omega_c t + \phi_{CE}) \tag{8.1}$$

where E_0 is the amplitude of the electric field envelope and ω_c is the center frequency of the laser pulse.

In Fig. 8.6, examples of a few-cycle pulse with a CE-phase shift and a multi-cycle pulse are shown. A phase shift in a few-cycle pulse is more apparent than in a long, multi-cycle pulse.

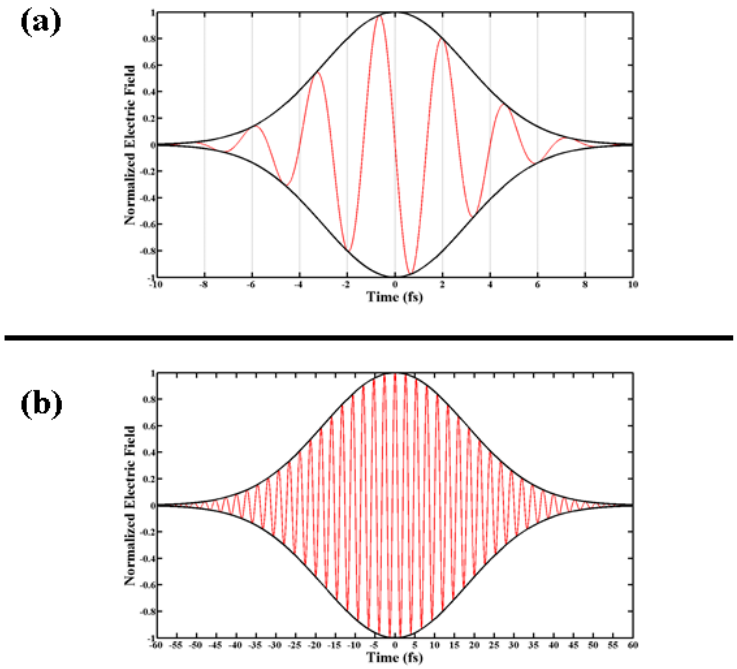

Figure 8.6: (a) Few-cycle laser pulse (5 fs, 800 nm) showing CE-phase shift of $\pi/2$ and (b) multi-cycle laser pulse (30 fs, 800 nm).

8.3.2 Locking the Carrier-envelope Phase

In the frequency domain, the output of a laser cavity, without dispersion is a frequency comb with mode spacing of:

$$f_m = \frac{mc}{2nL} \tag{8.2}$$

where m is the mode index, c is the speed of light, n is the average index of refraction, and L is the cavity length.

If we now add dispersion, we can add in the effects of phase and group velocities. The electric field of the pulse train in the time domain can be expressed as:

$$E_{p-train}(t) = E_0(t)\cos(i\omega_c t) \otimes \sum_{m=-\infty}^{\infty} \delta(t - m\tau_{RT}) \tag{8.3}$$

and in the frequency domain:

$$\tilde{E}_{p-train}(f) = \tilde{E}_0(f - \frac{\omega_c}{2\pi}) \sum_{m=-\infty}^{\infty} \delta(f - mf_{rep}) \tag{8.4}$$

where $\tau_{RT} = 1/f_{rep}$ [96].

When the phase and group velocities are different, phase shifts arise:

$$\Delta\phi_{CE} = kL(n_g - n) = \omega L\left(\frac{1}{\nu_g} - \frac{1}{\nu_p}\right) = \frac{\omega^2 L}{c}\frac{dn}{d\omega} = -2\pi L\frac{dn}{d\lambda} \tag{8.5}$$

where n_g is the group index of refraction, n is the index of refraction, λ is the wavelength, ν_g is the group velocity, and ν_p is the phase velocity.

Including the CE-phase shift, the electric field of the pulse train in the time domain becomes:

$$E_{p-train}(t) = \sum_{j=-\infty}^{\infty} E(t - j\tau_{RT})\exp[i(\omega_c t + j(\Delta\phi_{CE} - \omega_c\tau_{RT})) + \phi_0] \tag{8.6}$$

and in the frequency domain:

$$\tilde{E}_{p-train}(\omega) = \tilde{E}(\omega - \omega_c)\exp(i\phi_0)\sum_{m=-\infty}^{\infty}\delta(\Delta\phi_{CE} - \omega\tau_{RT} - 2\pi m) \tag{8.7}$$

where ϕ_0 is the CE-phase of the zeroth pulse.

The frequency spacing in the comb can now be written as:

$$f_m = \frac{m}{\tau_{RT}} - \frac{\Delta\phi_{CE}}{2\pi\tau_{RT}} = mf_{rep} + f_0 \tag{8.8}$$

This implies that if f_0 is held constant, then the laser output is considered to be CE-phase stabilized. Experimentally, without an active feedback loop, the CE-phase is essentially random on a shot-to-shot basis. In order to lock the phase to some particular value, measuring f_0 is essential.

f-to-$2f$ Interferometer

One common way to measure the CE-phase of a laser pulse is through the use of an f-to-$2f$ interferometer, self-referencing technique. The basic idea, visualized in Fig. 8.7, begins with the laser output pulse that we want to measure being spectrally broadened to span $\sim$ 1 octave. This is accomplished with a sapphire plate in the HITS system. The now broadened pulse is frequency doubled. This is accomplished by using a BBO in the HITS system. The original broadened pulse and the frequency doubled pulse co-propagate with a time delay τ between the two pulses. The "blue" side of the original broadened pulse now interferes with the "red" side of the frequency doubled pulse. Mathematically:

$$2f_m - f_{2m} = 2(mf_{rep} + f_0) - (2mf_{rep} + f_0) = f_0 \tag{8.9}$$

The interference pattern is measured by a spectrometer, with an integration time on the order of the repetition rate of the laser (1 kHz), and the "jitter" of the fringe pattern from laser pulse to laser pulse is what indicates the CEP noise of the laser system.

In order to phase lock the laser system, the interference pattern from the f-to-$2f$ output, is also sent to a quadrant position sensitive photodiode. The photodiode signal is integrated

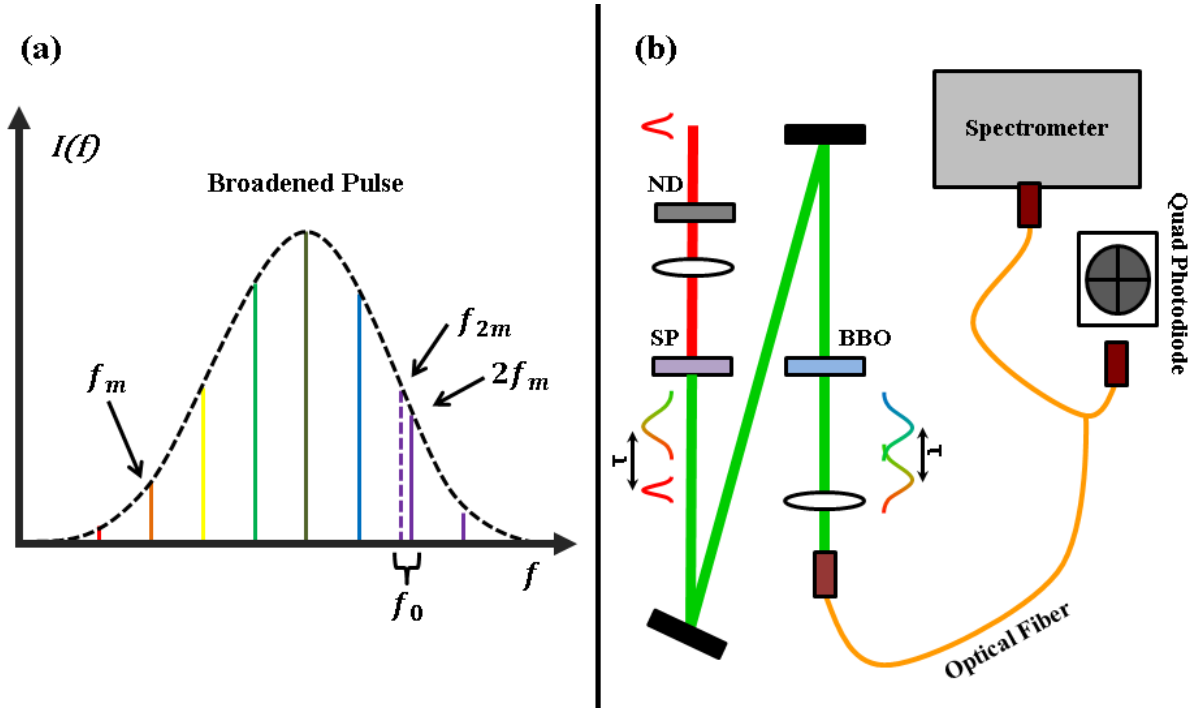

Figure 8.7: (a) Broadened laser pulse indicating the appropriate interference frequencies and (b) schematic of the HITS f-to-$2f$ interferometer.

to give an analog error signal which is used as the input for a proportional-integral-derivative (PID) locking device. The feedback from the PID controller is sent to a piezo actuator mounted to a cavity mirror in the oscillator (fast-loop) and also to an actuator in the grating compressor (slow-loop). It should be noted the f-to-$2f$ interferometer described in this section is located at the output of the HITS system, after the compressor, see Fig. 8.8(a). A different design of f-to-$2f$ can be found in the oscillator (Menlo Systems, XPS800). Although not discussed in detail, the oscillator f-to-$2f$ acts as a fast-loop feedback in a more controlled environment, allowing for an initially CEP stable seed for the rest of the HITS system.

8.3.3 CE Phase Stabilization Improvements

When first installed, the HITS laser was able to be CE-phase locked, but was far from the anticipated 250 mrad RMS single-shot stability that was projected. Through the collaboration of the original laser design team (KM-Labs) and Carlos Trallero's research group (Kansas State University), the HITS laser was modified to reach that goal, and for longer

time durations than originally predicted.

The CE-phase noise in a laser system comes from many different sources. Typically, air flow causes fast drifts in the CEP by varying the path index of refraction on a shot-to-shot basis. Also, temperature changes introduce a slow drift to the CE-phase as optics materials expand or relax which, in effect, changes the laser alignment. Both of these issues are addressed by keeping the system boxed in its own environment with excellent temperature and humidity control of the laser room. Another source of noise, and the most prevalent one in the HITS system, is vibrations induced by equipment and the building environment as a whole.

Vibration Mapping and Analysis

Although CE-phase noise due to vibration was always a suspected source, precautions were made prior to the construction of the laser. The optics table (Newport RS 4000) is designed to dampen high frequency noise ($\gtrsim$ 200 Hz). The damping effect works as a function of distance from the source on the table and also helps to isolate the table from floor vibrations.

In order to identify the sources of vibrations, we performed a systematic study, which involved the use of an accelerometer (Omega Engineering, INC. Model ACC-PS2) to map out potential "problem areas" in the laser while comparing them to areas outside of the laser box environment, see Fig. 8.8. The accelerometer output was recorded by an oscilloscope over time durations long enough to resolve low frequency oscillations (range: $<$ 1 - 1200 Hz). Each trace in time was Fourier-transformed to the frequency domain. The prominent frequency components were identified and the corresponding mechanism for the noise was determined.

Labeled in Fig. 8.8(a), the areas that were tested were the optics table far from the laser, stretcher, compressor, next to the 1st stage amplifier crystal, the floor, a wall between the laser room and the equipment/pump closet, and the floor in that closet. In order to see what was causing the noise, we systematically shut down different sources and recorded the frequency spectrum. The sources were the AC unit in the closet (CAC), the laser room AC

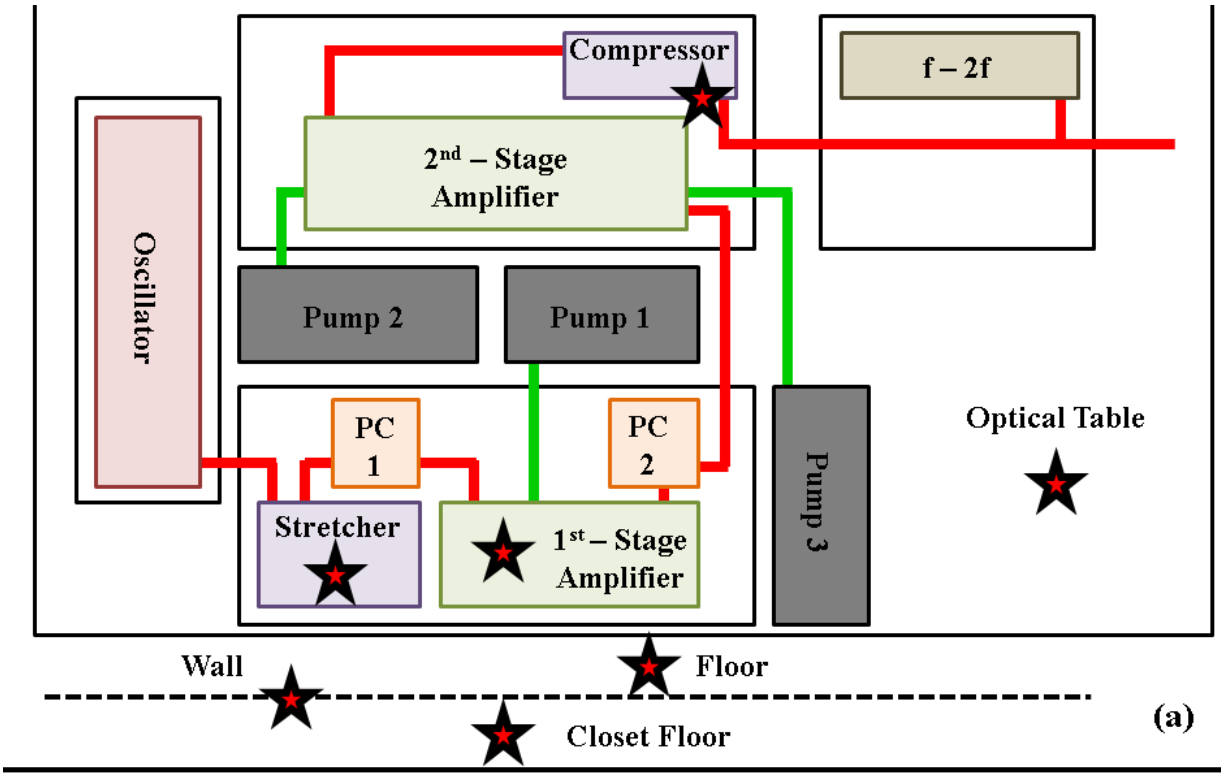
Compressor
f – 2f
2nd – Stage Amplifier
Oscillator
Pump 2
Pump 1
PC 1
PC 2
Pump 3
Optical Table
Stretcher
1st – Stage Amplifier
Wall
Floor
Closet Floor

(a)

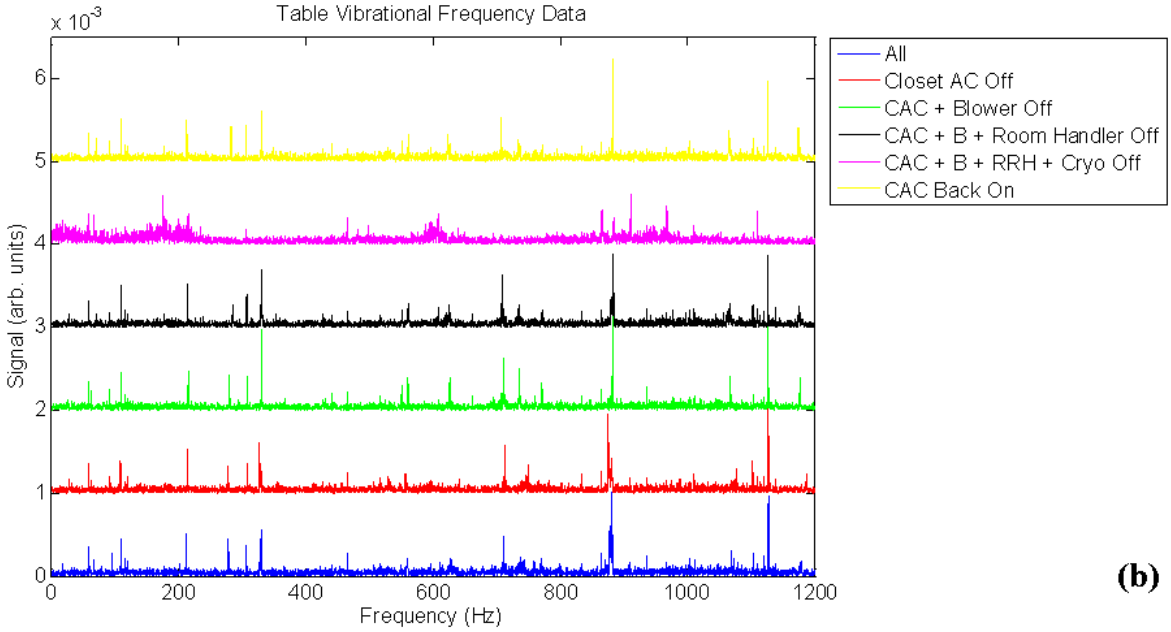
Table Vibrational Frequency Data
x 10-3
Signal (arb. units)
Frequency (Hz)
All
Closet AC Off
CAC + Blower Off
CAC + B + Room Handler Off
CAC + B + RRH + Cryo Off
CAC Back On

(b)

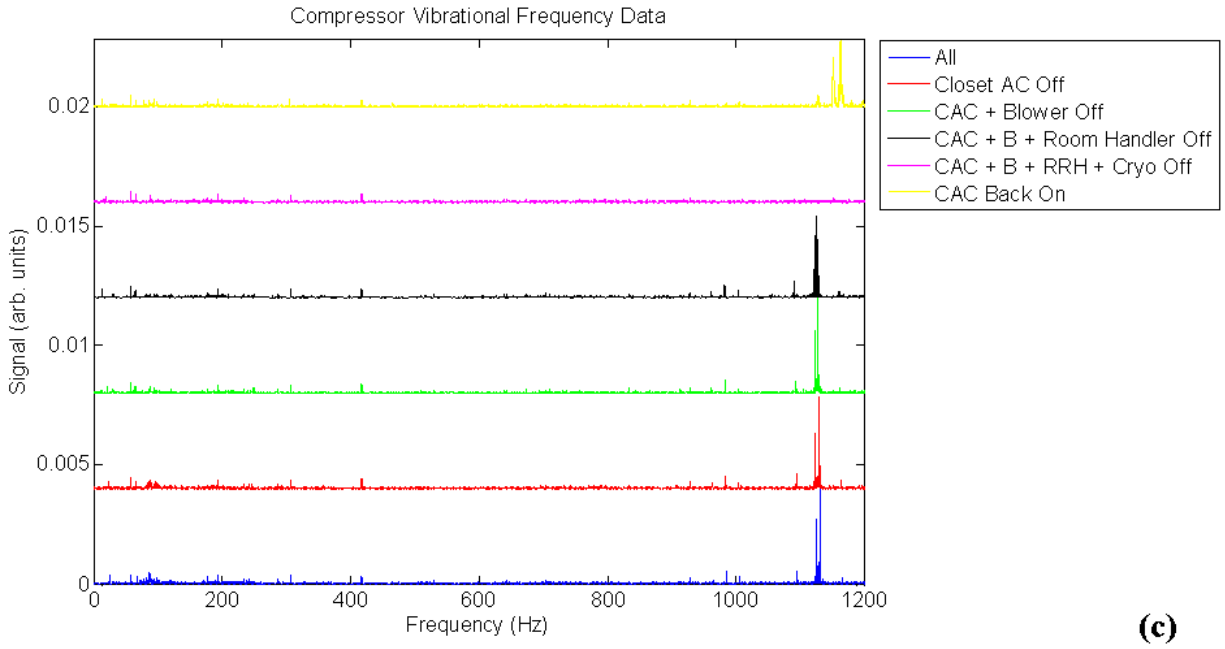
Compressor Vibrational Frequency Data
Signal (arb. units)
Frequency (Hz)
0
0.005
0.01
0.015
0.02
0
200
400
600
800
1000
1200
All
Closet AC Off
CAC + Blower Off
CAC + B + Room Handler Off
CAC + B + RRH + Cryo Off
CAC Back On

(c)

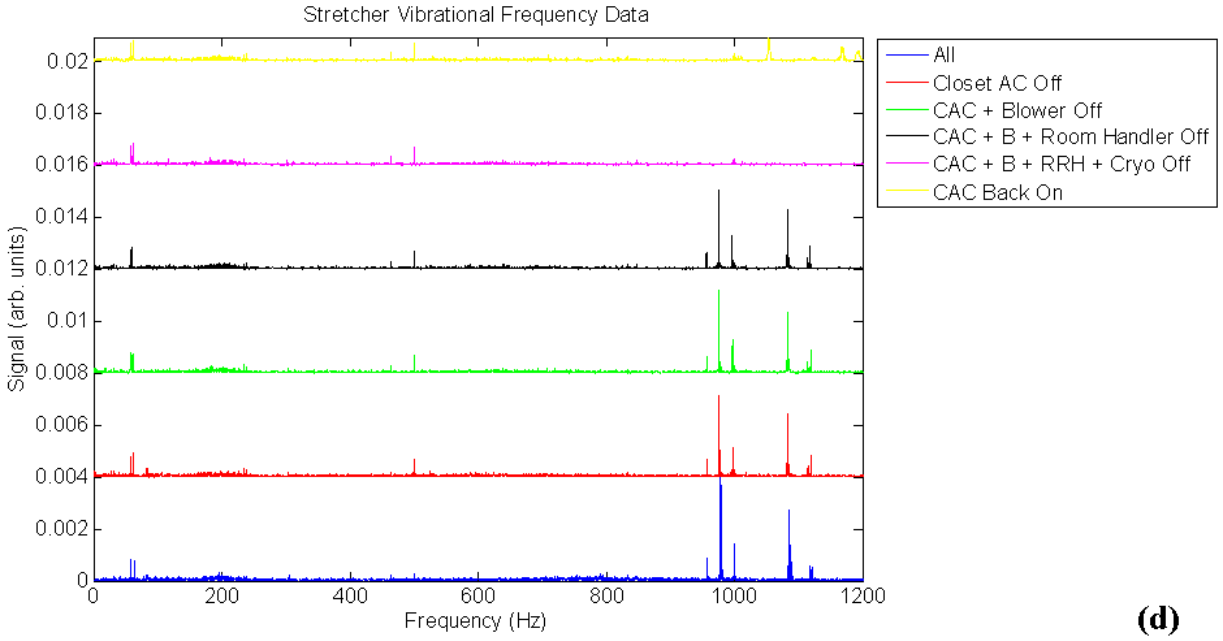
Stretcher Vibrational Frequency Data
Signal (arb. units)
Frequency (Hz)
0
0.002
0.004
0.006
0.008
0.01
0.012
0.014
0.016
0.018
0.02
0
200
400
600
800
1000
1200
All
Closet AC Off
CAC + Blower Off
CAC + B + Room Handler Off
CAC + B + RRH + Cryo Off
CAC Back On

(d)

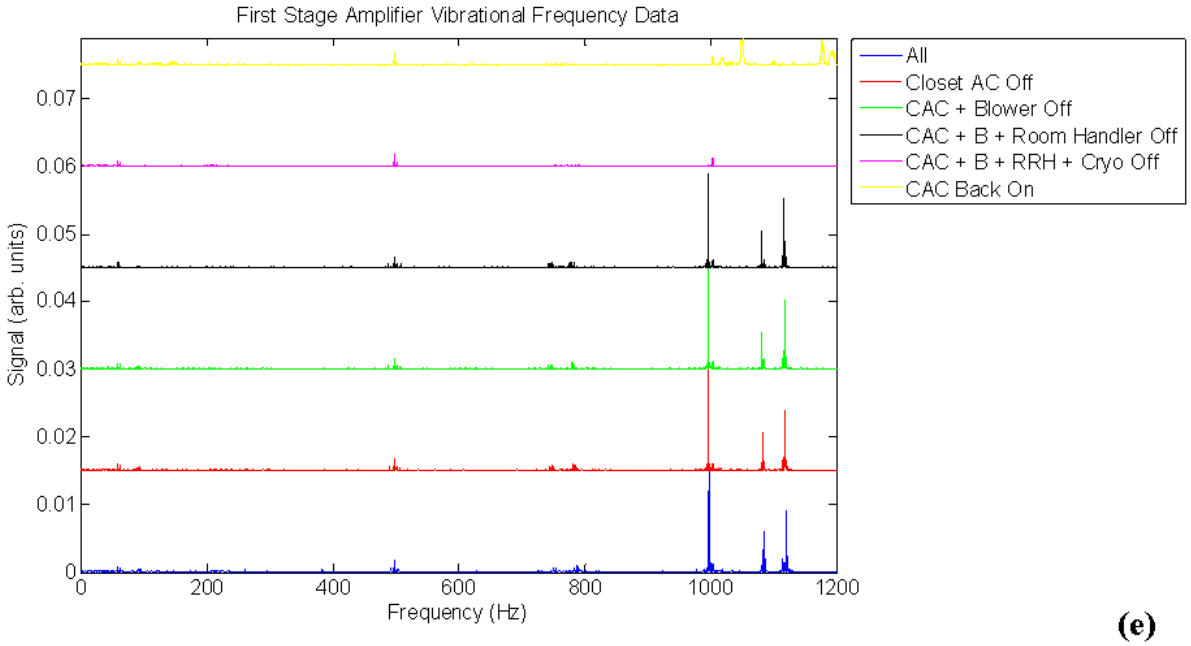
First Stage Amplifier Vibrational Frequency Data
Signal (arb. units)
Frequency (Hz)
0
0.01
0.02
0.03
0.04
0.05
0.06
0.07
0
200
400
600
800
1000
1200
All
Closet AC Off
CAC + Blower Off
CAC + B + Room Handler Off
CAC + B + RRH + Cryo Off
CAC Back On

(e)

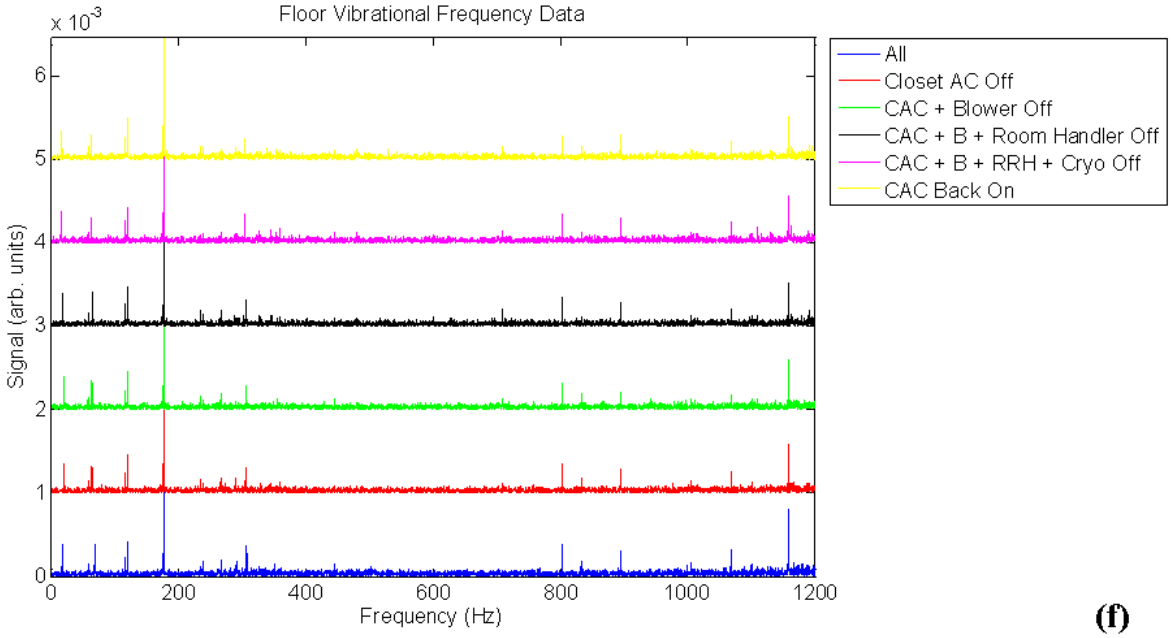
Floor Vibrational Frequency Data
x 10^-3
Signal (arb. units)
Frequency (Hz)
0
1
2
3
4
5
6
0
200
400
600
800
1000
1200
All
Closet AC Off
CAC + Blower Off
CAC + B + Room Handler Off
CAC + B + RRH + Cryo Off
CAC Back On

(f)

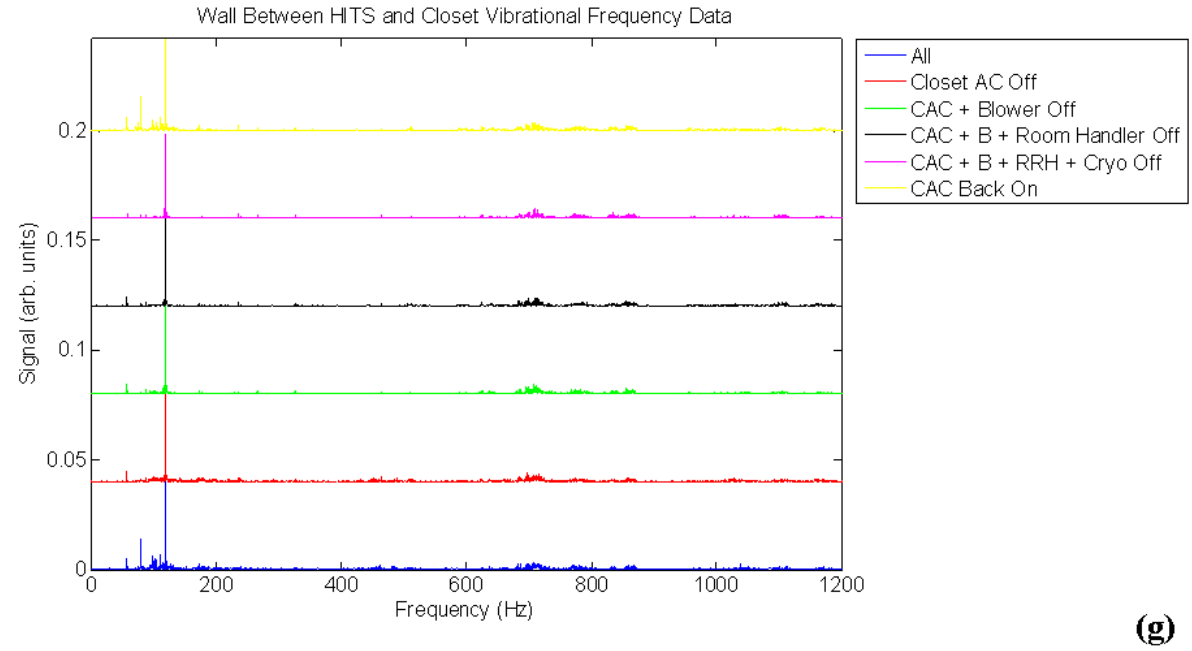

(g)

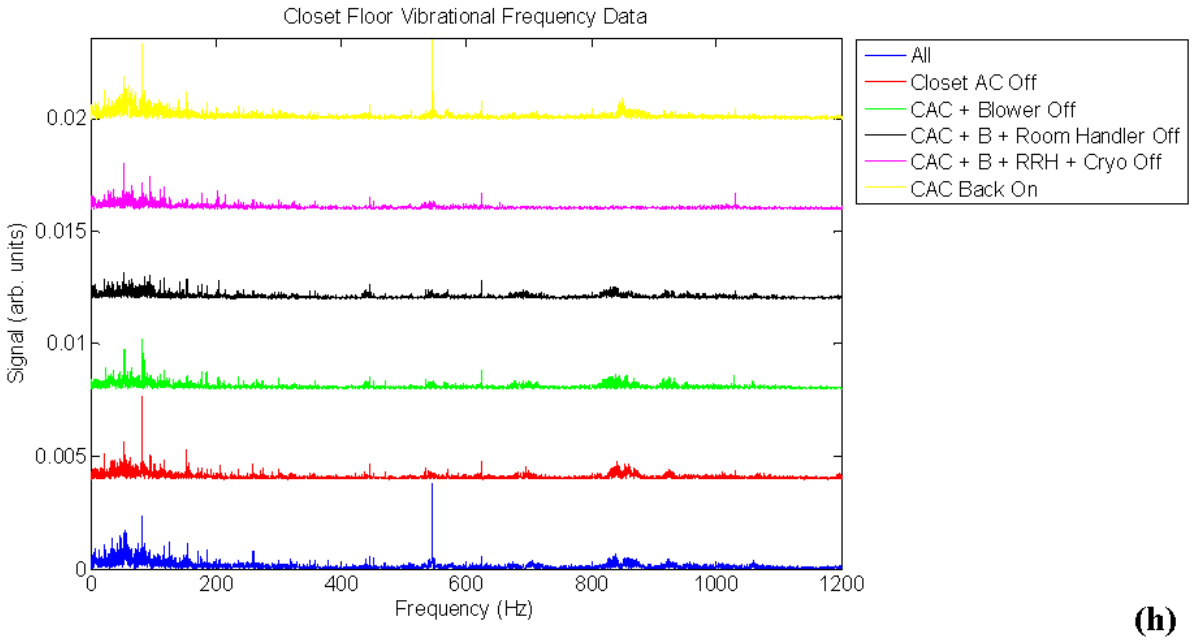

(h)

Figure 8.8: Mapping the vibrations on the HITS laser system: (a) locations of the accelerometer measurements (stars), (b) optics table, (c) compressor, (d) stretcher, (e) first stage amplifier, (f) laser room floor, (g) equipment/pump closet wall, (h) equipment/pump closet floor. Each frequency spectrum is offset for better visual clarity.

blowers (B), the laser AC room handler (RH), and the cryo cooling system for the amplifier crystals (cryo). The system cannot run without the cryo system for very long, but it was a helpful indicator of problem areas.

In brief summary, shown in Fig. 8.8, the vibration sources contributed the most in the higher frequencies. The lower frequency components were persistent overall; however, of the sources, the room AC and cryo cooling system coupled the most noise to the table. By looking at the first stage amplifier, compressor, and stretcher, it was determined that the table noise could not be eliminated externally, because the cryo is an essential system. It was decided that the best course of action was to further isolate the stretcher and compressor from the rest of the table.

In Fig. 8.9, three different isolation techniques were tested. The first was a vibration absorbing mat that went under the breadboard of the stretcher. The second was four rubber bushings placed under the stretcher breadboard with supporting clamps. The final, and most effective technique, was to "float" the stretcher. Supportive clamps placed on vibration absorbing rubber, minimized direct table contact and reduced vibrations from coupling into the stretcher breadboard.

Results

The "floating" breadboard technique was used in both the stretcher and compressor. As shown in Fig. 8.10, the laser was successfully locked for 9 hours with a single-shot RMS value of 300 mrad! Although a CE-phase stability milestone was reached, further modifications to the damping design could be made to reach even lower single-shot CEP error. Continued testing is currently an active research endeavor.

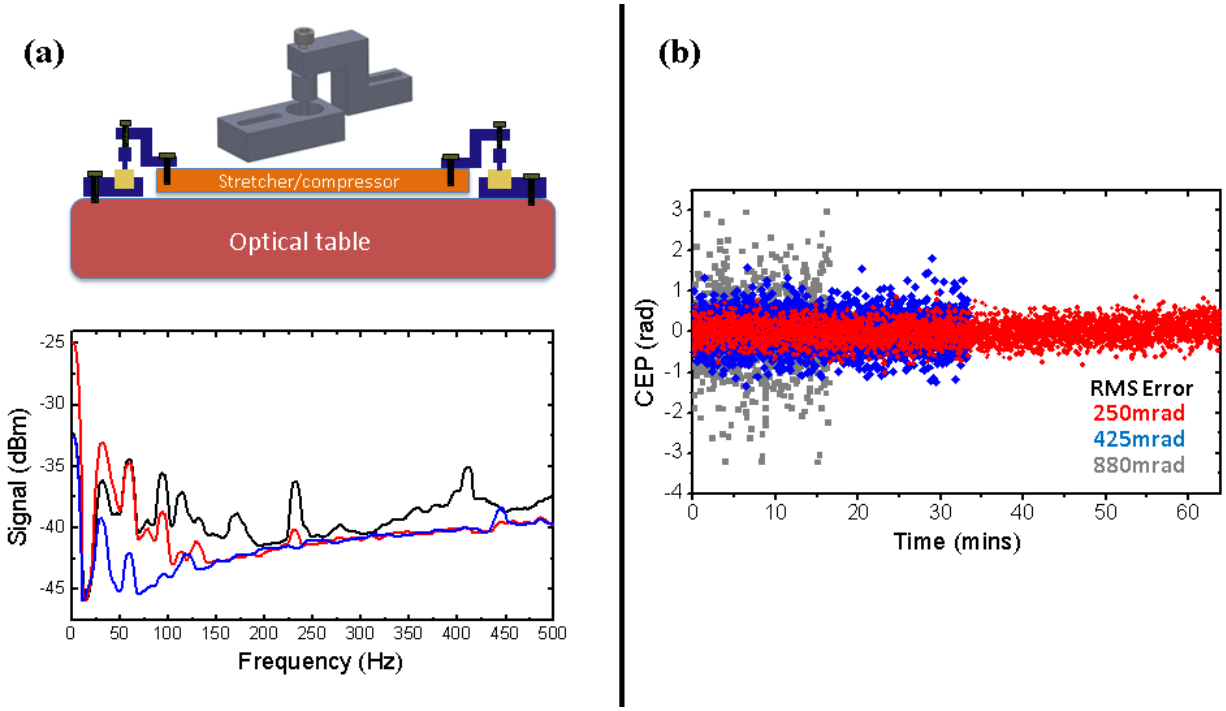

Figure 8.9: Vibration damping schemes of the laser stretcher for the improvement of CE-phase locking: (a) Floating stretcher design and low frequency spectral damping from absorbing mat (black), rubber bushings (red), and "floating" (blue). (b) The effect of different damping schemes on the CEP for absorbing mat (grey), rubber bushings (red), and "floating" (blue). Adapted from Langdon *et al.* [59].

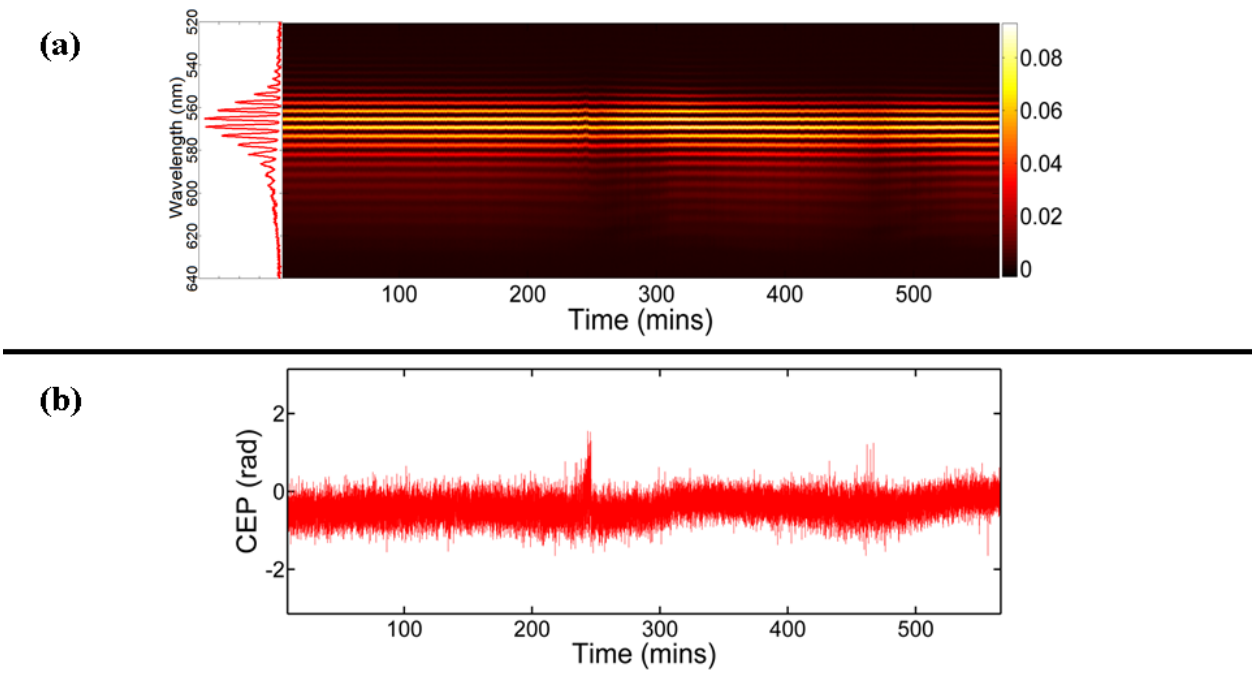

Figure 8.10: (a) Spectral fringes of CEP measurement. (b) CEP for long-term single-shot stability with "floating" stretcher and compressor. Adapted from Langdon *et al.* [59].

8.4 Summary

In this chapter, we introduced three new directions that the strong-field ionization experiments covered in this thesis could move toward. The first was continued spectroscopic studies of isomeric molecules by looking at the photoelectron momentum distributions of the samples studied in this thesis. Through the use of a VMI spectrometer and pump-probe (NIR-XUV) experiment design, the structure and dynamics of molecules can be better understood. The outlook and next step is to complete testing of the VMI and further develop an intense XUV source.

The second direction is to continue wavelength dependent ionization studies by using an intense, femtosecond tunable light source in the long-wave infrared (5500 - 8500 nm). By pushing further into the infrared, the tunneling ionization regime becomes more dominant. It is possible that at these longer wavelengths, the known models for SFI start to break down. The outlook and next step are to reconfirm our observations in our atomic studies and once fully characterized, move onto molecular systems.

The final direction is into carrier envelope phase dependent, strong-field spectroscopic studies. We show that the HITS laser has the capabilities to generate CE-phase stable laser pulses in the NIR with an RMS error of 300 mrad over a time duration of 9 hours. In addition to CE-phase experiments, this capability is a starting point for more advanced light source development projects including waveform synthesis.

Chapter 9

Summary and Concluding Remarks

The main goal of this thesis was to study the complexities of photoionization in both the strong- and weak-field limits such that they serve as examples for the continued understanding of single photoionization both experimentally and theoretically. To be more specific, the focus was the study of the photoionization of isomeric molecules in order to gain insight into the effects of structural differences on the ionization yields of molecules. In this section, we summarize the work presented in this thesis and, in fact, show that our goal was accomplished.

Our investigation of strong-field ionization of isomeric molecules began with an experiment comparing two molecular stereoisomer pairs, *cis*-, *trans*-2-butene and *cis*-, *trans*-1,2-dichloroethylene. Our initial hypothesis was that for randomly oriented molecular isomers with $\Delta I_p \approx 0.01$ eV, the ratio of the parent ion yields as a function of intensity should be approximately unity. However, we found that the difference between the yields in each pair was as large as a factor of two for femtosecond laser pulses centered at 790 nm. The yield ratios were compared to the theoretical ratios calculated using three different strong-field molecular ionization models, MO-ADK, MO-PPT, and MO-SFA. Within the error of the measurement, it was unclear as to which model best matched the experiment.

Returning to our original motivation for the investigation of stereoisomers in the presence of a strong-field, namely, HHG of isomeric molecules, our results are in disagreement with

previous studies [41, 42], where the large differences in HHG yield is attributed to differences in ionization yields. Furthermore, following the theme of differential characterization of molecular isomers, we are now able to comment on the effects in strong-field ionization yield due to a permanent dipole moment in a molecule. We found that when comparing the polar *cis*-isomer to the non-polar *trans*-isomer, there was no consistent dominance of the polar isomer over the non-polar isomer.

Expanding on the study of stereoisomers, we added two additional isomer pairs to the sample list, 1,3-butadiene, 1-butyne and butane, isobutane. These new pairs are structural isomers and introduce larger changes between the ground states of the isomer pairs. The isomers 1,3-butadiene, 1-butyne have the largest ionization potential difference, $\Delta I_p \approx 1$ eV and butane, isobutane have $\Delta I_p \approx 0.1$ eV. Wavelength-dependent strong-field ionization yield studies were performed in the wavelength range of 790 - 2000 nm on all four isomeric pairs. Although each molecular isomer pair had unique results, the main conclusions of the experiment were that ionization potential appears to be the dominating contributor to yield differences, in cases of large ΔI_p, and that the influence is great enough to mask other effects that might be present. Within the error of the measurement, the wavelength dependence was not very significant.

Continuing our investigation of single photoionization, measurements of the total ionization yield of isomeric molecule pairs in the weak-field limit were performed. Single photon ionization using photon energies of 20 - 45 eV showed that the ratio of the ionization yields of the isomeric pairs were close to unity as a function of photon energy. Although the comparison to the strong-field limit is not direct, the results suggest that strong-field ionization is more heavily influenced by the structural changes between isomeric molecules.

As a concluding remark, the strong-field single ionization of molecules as a function of intensity is a complex problem. The work in this thesis succeeded in providing examples of photoionization of molecular isomer pairs in both the strong- and weak-field limit. The examples should be used for the continued understanding of single photoionization both experimentally and theoretically.

Bibliography

[1] S. Wallin, A. Pettersson, H. Östmark, and A. Hobro, Anal. Bioanal. Chem. **395**, 259 (2009).

[2] A. J. DeMaria, D. A. Stetser, and H. Heynau, Appl. Phys. Lett. **8**, 174 (1966).

[3] C. V. Shank and E. P. Ippen, Appl. Phys. Lett. **24**, 373 (1974).

[4] P. F. Moulton, J. Opt. Soc. Am. B **3**, 125 (1986).

[5] D. E. Spence, P. N. Kean, and W. Sibbett, Opt. Lett. **16**, 42 (1991).

[6] D. Strickland and G. Mourou, Opt. Commun. **56**, 219 (1985).

[7] M. J. Rosker, M. Dantus, and A. H. Zewail, J. Chem. Phys. **89**, 6113 (1988).

[8] A. H. Zewail, Science **242**, 1645 (1988).

[9] C. I. Blaga, F. AU Catoire, P. Colosimo, G. G. Paulus, H. G. Muller, P. Agostini, and L. F. DiMauro, Nat. Phys. **5**, 335 (2009).

[10] A. McPherson, G. Gibson, H. Jara, U. Johann, T. S. Luk, I. A. McIntyre, K. Boyer, and C. K. Rhodes, J. Opt. Soc. Am. B **4**, 595 (1987).

[11] M. Ferray, A. L'Huillier, X. F. Li, L. A. Lompre, G. Mainfray, and C. Manus, J. Phys. B: At., Mol. Opt. Phys. **21**, L31 (1988).

[12] X. F. Li, A. L'Huillier, M. Ferray, L. A. Lompré, and G. Mainfray, Phys. Rev. A **39**, 5751 (1989).

[13] P. B. Corkum, Phys. Rev. Lett. **71**, 1994 (1993).

[14] J. B. Bertrand, H. J. Wörner, P. Hockett, D. M. Villeneuve, and P. B. Corkum, Phys. Rev. Lett. **109**, 143001 (2012).

[15] L. V. Keldysh, Sov. Phys. JETP **20**, 1307 (1965).

[16] F. H. M. Faisal, J. Phys. B: At., Mol. Opt. Phys. **6**, L89 (1973).

[17] H. R. Reiss, Phys. Rev. A **22**, 1786 (1980).

[18] S. L. Chin, F. Yergeau, and P. Lavigne, J. Phys. B: At., Mol. Opt. Phys. **18**, L213 (1985).

[19] M. V. Ammosov, N. B. Delone, and V. P. Krainov, Sov. Phys. JETP **64**, 1191 (1986).

[20] A. M. Perelomov, V. S. Popov, and M. V. Terent'ev, Sov. Phys. JETP **23**, 924 (1966).

[21] A. M. Perelomov, V. S. Popov, and M. V. Terent'ev, Sov. Phys. JETP **24**, 207 (1967).

[22] A. M. Perelomov and V. S. Popov, Sov. Phys. JETP **25**, 336 (1967).

[23] S. V. Popruzhenko, V. D. Mur, V. S. Popov, and D. Bauer, Phys. Rev. Lett. **101**, 193003 (2008).

[24] M. G. Pullen, W. C. Wallace, D. E. Laban, A. J. Palmer, G. F. Hanne, A. N. Grum-Grzhimailo, K. Bartschat, I. Ivanov, A. Kheifets, D. Wells, H. M. Quiney, X. M. Tong, I. V. Litvinyuk, R. T. Sang, and D. Kielpinski, Phys. Rev. A **87**, 053411 (2013).

[25] G. N. Gibson, R. R. Freeman, and T. J. McIlrath, Phys. Rev. Lett. **67**, 1230 (1991).

[26] G. Gibson, T. S. Luk, and C. K. Rhodes, Phys. Rev. A **41**, 5049 (1990).

[27] S. Augst, D. D. Meyerhofer, D. Strickland, and S. L. Chin, J. Opt. Soc. Am. B **8**, 858 (1991).

[28] B. Walker, B. Sheehy, L. F. DiMauro, P. Agostini, K. J. Schafer, and K. C. Kulander, Phys. Rev. Lett. **73**, 1227 (1994).

[29] C. Guo, M. Li, J. P. Nibarger, and G. N. Gibson, Phys. Rev. A **58**, R4271 (1998).

[30] C. Guo, M. Li, J. P. Nibarger, and G. N. Gibson, Phys. Rev. A **61**, 033413 (2000).

[31] C. Guo and G. N. Gibson, Phys. Rev. A **63**, 040701 (2001).

[32] J. Wu, L. P. H. Schmidt, M. Kunitski, M. Meckel, S. Voss, H. Sann, H. Kim, T. Jahnke, A. Czasch, and R. Dörner, Phys. Rev. Lett. **108**, 183001 (2012).

[33] I. V. Litvinyuk, K. F. Lee, P. W. Dooley, D. M. Rayner, D. M. Villeneuve, and P. B. Corkum, Phys. Rev. Lett. **90**, 233003 (2003).

[34] X. M. Tong, Z. X. Zhao, and C. D. Lin, Phys. Rev. A **66**, 033402 (2002).

[35] E. P. Benis, J. F. Xia, X. M. Tong, M. Faheem, M. Zamkov, B. Shan, P. Richard, and Z. Chang, Phys. Rev. A **70**, 025401 (2004).

[36] L. B. Madsen, F. Jensen, O. I. Tolstikhin, and T. Morishita, Phys. Rev. A **87**, 013406 (2013).

[37] O. I. Tolstikhin, T. Morishita, and L. B. Madsen, Phys. Rev. A **84**, 053423 (2011).

[38] L. B. Madsen, O. I. Tolstikhin, and T. Morishita, Phys. Rev. A **85**, 053404 (2012).

[39] S.-F. Zhao, L. Liu, and X. X. Zhou, Opt. Commun **313**, 74 (2014).

[40] S.-F. Zhao, A.-T. Le, C. Jin, X. Wang, and C. D. Lin, Phys. Rev. A **93**, 023413 (2016).

[41] M. C. H. Wong, J. P. Brichta, M. Spanner, S. Patchkovskii, and V. R. Bhardwaj, Phys. Rev. A **84**, 051403 (2011).

[42] M. C. H. Wong, J. P. Brichta, M. Spanner, S. Patchkovskii, and V. R. Bhardwaj, Phys. Rev. A **85**, 049901 (2012).

[43] A.-T. Le, R. R. Lucchese, and C. D. Lin, Phys. Rev. A **88**, 021402 (2013).

[44] X. Zhu, X. Liu, P. Lan, D. Wang, Q. Zhang, W. Li, and P. Lu, Opt. Express **24**, 24824 (2016).

[45] J. M. Dela Cruz, V. V. Lozovoy, and M. Dantus, J. Mass Spectrom. **42**, 178 (2007).

[46] C. Zhou, T. Qiu-Nan, Z. Cong-Cong, and H. Zhan, Chin. Phys. B **24**, 043303 (2015).

[47] F. R. Elder, A. M. Gurewitsch, R. V. Langmuir, and H. C. Pollock, Phys. Rev. **71**, 829 (1947).

[48] J. B. West and G. V. Marr, Proc. R. Soc. A **349**, 397 (1976).

[49] Annu. Rev. Biophys. Biomol. Struct. **33**, 157 (2004), pMID: 15139809.

[50] M. Y. Ivanov, M. Spanner, and O. Smirnova, J. Mod. Opt. **52**, 165 (2005).

[51] G. L. Yudin and M. Y. Ivanov, Phys. Rev. A **64**, 013409 (2001).

[52] A. M. Dykhne, Sov. Phys. JETP **11**, 411 (1960).

[53] N. B. Delone and V. P. Krainov, J. Opt. Soc. Am. B **8**, 1207 (1991).

[54] M. J. F. *et al.*, "Gaussian 03, Revision C.02," (2004), Gaussian, Inc., Wallingford, CT.

[55] M. W. Schmidt, K. K. Baldridge, J. A. Boatz, S. T. Elbert, M. S. Gordon, J. H. Jensen, S. Koseki, N. Matsunaga, K. A. Nguyen, S. Su, T. L. Windus, M. Dupuis, and J. A. Montgomery, J. Comput. Chem. **14**, 1347 (1993).

[56] A.-T. Le, R. R. Lucchese, S. Tonzani, T. Morishita, and C. D. Lin, Phys. Rev. A **80**, 013401 (2009).

[57] M. Lewenstein, P. Balcou, M. Y. Ivanov, A. L'Huillier, and P. B. Corkum, Phys. Rev. A **49**, 2117 (1994).

[58] B. Chang, P. R. Bolton, and D. N. Fittinghoff, Phys. Rev. A **47**, 4193 (1993).

[59] B. Langdon, J. Garlick, X. Ren, D. J. Wilson, A. M. Summers, S. Zigo, M. F. Kling, S. Lei, C. G. Elles, E. Wells, E. D. Poliakoff, K. D. Carnes, V. Kumarappan, I. Ben-Itzhak, and C. A. Trallero-Herrero, Opt. Express **23**, 4563 (2015).

[60] D. J. Kane and R. Trebino, IEEE J. Quant. Electron. **29**, 571 (1993).

[61] R. Trebino, K. W. DeLong, D. N. Fittinghoff, J. N. Sweetser, M. A. Krumbügel, B. A. Richman, and D. J. Kane, Rev. Sci. Instrum. **68**, 3277 (1997).

[62] R. Trebino and D. J. Kane, J. Opt. Soc. Am. A **10**, 1101 (1993).

[63] D. J. Kane, J. Opt. Soc. Am. B **25**, A120 (2008).

[64] K. W. DeLong, R. Trebino, and W. E. White, J. Opt. Soc. Am. B **12**, 2463 (1995).

[65] H. Deutsch, K. Becker, R. K. Janev, M. Probst, and T. D. Märk, J. Phys. B: At., Mol. Opt. Phys. **33**, L865 (2000).

[66] J. E. Hudson, C. Vallance, M. Bart, and P. W. Harland, J. Phys. B: At., Mol. Opt. Phys. **34**, 3025 (2001).

[67] C. Szmytkowski and S. Kwitnewski, J. Phys. B: At., Mol. Opt. Phys. **36**, 4865 (2003).

[68] A. D. Shiner, C. Trallero-Herrero, N. Kajumba, B. E. Schmidt, J. B. Bertrand, K. T. Kim, H. C. Bandulet, D. Comtois, J. C. Kieffer, D. M. Rayner, P. B. Corkum, F. Legare, and D. M. Villeneuve, J. Mod. Opt. **60**, 1458 (2013).

[69] G. N. Gibson, R. R. Freeman, T. J. McIlrath, and H. G. Muller, Phys. Rev. A **49**, 3870 (1994).

[70] S. Zigo, A.-T. Le, P. Timilsina, and C. A. Trallero-Herrero, Sci. Rep. **7** (2017), 10.1038/srep42149.

[71] M. H. Kutner, C. Nachtsheim, and J. Neter, *Applied Linear Regression Models*, 4th ed. (McGraw-Hill/Irwin, 2004).

[72] E. G. Lewars, *Computational Chemistry: Introduction to the Theory and Applications of Molecular and Quantum Mechanics*, 2nd ed. (Springer Science and Business Media, 2011).

[73] H. Li, D. Ray, S. De, I. Znakovskaya, W. Cao, G. Laurent, Z. Wang, M. F. Kling, A. T. Le, and C. L. Cocke, Phys. Rev. A **84**, 043429 (2011).

[74] L. Holmegaard, J. L. Hansen, L. Kalhoj, S. L. Kragh, H. Stapelfeldt, F. Filsinger, J. Küpper, G. Meijer, D. Dimitrovski, M. Abu-samha, C. P. J. Martiny, and L. B. Madsen, Nat. Phys. **6**, 428 (2010).

[75] D. Dimitrovski, C. P. J. Martiny, and L. B. Madsen, Phys. Rev. A **82**, 053404 (2010).

[76] J. L. Hansen, L. Holmegaard, J. H. Nielsen, H. Stapelfeldt, D. Dimitrovski, and L. B. Madsen, J. Phys. B: At., Mol. Opt. Phys. **45**, 015101 (2012).

[77] Q. Song, Z. Li, H. Li, P. Lu, X. Gong, Q. Ji, K. Lin, W. Zhang, J. Ma, H. Zeng, F. He, and J. Wu, Opt. Express **25**, 2221 (2017).

[78] S. De, I. Znakovskaya, D. Ray, F. Anis, N. G. Johnson, I. A. Bocharova, M. Magrakvelidze, B. D. Esry, C. L. Cocke, I. V. Litvinyuk, and M. F. Kling, Phys. Rev. Lett. **103**, 153002 (2009).

[79] S. G. Lias, in *NIST Chemistry WebBook, NIST Standard Reference Database Number 69*, edited by P. Linstrom and W. Mallard (National Institute of Standards and Technology, Gaithersburg MD, 20899, retrieved July 28, 2016).

[80] M. Berglund and M. E. Wieser, Pure Appl. Chem. **83**, 397 (2011).

[81] A.-T. Le, H. Wei, C. Jin, and C. D. Lin, J. Phys. B: At., Mol. Opt. Phys. **49**, 053001 (2016).

[82] D. J. Dummer, S. G. Kaplan, L. M. Hanssen, A. S. Pine, and Y. Zong, Appl. Opt. **37**, 1194 (1998).

[83] U. Ablikim, C. Bomme, H. Xiong, E. Savelyev, R. Obaid, B. Kaderiya, S. Augustin, K. Schnorr, I. Dumitriu, T. Osipov, R. Bilodeau, D. Kilcoyne, V. Kumarappan, A. Rudenko, N. Berrah, and D. Rolles, Sci. Rep. **6** (2016), 10.1038/srep38202.

[84] N. G. Kling, D. Paul, A. Gura, G. Laurent, S. De, H. Li, Z. Wang, B. Ahn, C. H. Kim, T. K. Kim, I. V. Litvinyuk, C. L. Cocke, I. Ben-Itzhak, D. Kim, and M. F. Kling, J. Instrum. **9**, P05005 (2014).

[85] D. A. Dahl, J. E. Delmore, and A. D. Appelhans, Rev. Sci. Instrum. **61**, 607 (1990).

[86] D. Whitley, Stat. Comput. **4**, 65 (1994).

[87] G. A. Garcia, L. Nahon, and I. Powis, Rev. Sci. Instrum. **75**, 4989 (2004).

[88] A. M. Summers, X. Yu, X. Wang, M. Raoul, J. Nelson, D. Todd, S. Zigo, S. Lei, and C. A. Trallero-Herrero, Opt. Express **25**, 1646 (2017).

[89] S. Linden, J. Kuhl, and H. Giessen, Opt. Lett. **24**, 569 (1999).

[90] O. Smirnova, M. Spanner, and M. Ivanov, J. Phys. B: At., Mol. Opt. Phys. **39**, S307 (2006).

[91] M. G. Pullen, W. C. Wallace, D. E. Laban, A. J. Palmer, G. F. Hanne, A. N. Grum-Grzhimailo, B. Abeln, K. Bartschat, D. Weflen, I. Ivanov, A. Kheifets, H. M. Quiney, I. V. Litvinyuk, R. T. Sang, and D. Kielpinski, Opt. Lett. **36**, 3660 (2011).

[92] W. C. Wallace, M. G. Pullen, D. E. Laban, O. Ghafur, H. Xu, A. J. Palmer, G. F. Hanne, K. Bartschat, A. N. Grum-Grzhimailo, H. M. Quiney, I. V. Litvinyuk, R. T. Sang, and D. Kielpinski, New J. Phys. **15**, 033002 (2013).

[93] E. Goulielmakis, M. Schultze, M. Hofstetter, V. S. Yakovlev, J. Gagnon, M. Uiberacker, A. L. Aquila, E. M. Gullikson, D. T. Attwood, R. Kienberger, F. Krausz, and U. Kleineberg, Science **320**, 1614 (2008).

[94] T. Wittmann, B. Horvath, W. Helml, M. G. Schatzel, X. Gu, A. L. Cavalieri, G. G. Paulus, and R. Kienberger, Nat. Phys. **5**, 357 (2009).

[95] A. Wirth, M. T. Hassan, I. Grguraš, J. Gagnon, A. Moulet, T. T. Luu, S. Pabst, R. Santra, Z. A. Alahmed, A. M. Azzeer, V. S. Yakovlev, V. Pervak, F. Krausz, and E. Goulielmakis, Science **334**, 195 (2011).

[96] S. T. Cundiff, J. Phys. D: Appl. Phys. **35**, R43 (2002).

Appendix A

Data Analysis Code

Contained within this appendix are five different scripts written to aid in the data analysis process of the experiments presented in this thesis. Each section of the appendix will contain a brief description of the script presented, what language it was written in, what it was used for, and the script itself.

Appendix Outline:

1. Nonadiabatic Tunneling Ionization and ADK Theory Code
2. Robust Fitting Code
3. Time-of-Flight Analysis Code
4. Intensity Redistribution Code
5. SIMION Sequential Search VMI Electrostatic Lens Optimization Code

A.1 Nonadiabatic Tunneling Ionization and ADK Theory Code

File Name: theory_calc.p

Language: Python 3.x

The purpose of this script is to calculate the strong-field ionization rate of a particular atomic system as a function of intensity. The user has the option of using two different atomic ionization models, nonadiabatic tunneling ionization [51] or ADK [19]. These are chosen by the user by defining *method* as either 'YI' or 'ADK', respectively.

In general, the script works with a user defined input arbitrary waveform representing the laser pulse used in the calculation. The input files are individual text files in single column format. The three files are essentially data arrays representing the electric field envelope, *envelope_file*, and phase, *phase_file*, both of which are a function of time, *time_file*. The array lengths for each file must be equal to each other and the time step size should be small enough to fully characterize the laser pulse. Typically this on the order of tens of picoseconds as the laser pulses are on the order of femtoseconds. The laser pulse is also defined by the center wavelength, *wavelength*.

In addition to the pulse parameters, the script requires the ionization potentials for both single ionization, *Ipot*, and double ionization, *Ipot2*, of the atomic system of interest. The ionization potentials of the nobel gases are listed within the code for reference. The inclusion of the second ion is to account for saturation effects in the calculation. Some atomic systems should include higher charge states, however, this script was not written to account for that. If the inclusion of double ionization is undesired, input a large ionization potential for the second ion such that its contribution is negligible.

The final required input for the script is the intensity range, *Imin* to *Imax*, and intensity step size, *Istep*, for the theoretical yield output. It is recommended that the intensity step size is at least half an order of magnitude smaller than the minimum intensity. The more

intensity values, the longer the code will take to run. Input units of the variables are listed within the code itself.

The output of the script is two text files in single column format. One automatically labeled *inten.txt* is the intensity points defined by the user input intensity range parameters and the other is the calculated ionization yield values. The text file for the yield is user selected by defining *file_name*. The calculated yield utilizes volume averaging for a gaussian beam described in [58].

Please note that the nonadiabatic tunneling ionization method utilizes the arbitrary waveform completely, but the ADK ionization method assumes an FTL pulse for the input envelope. Also, for both ionization methods, the ability to easily change the l and m quantum numbers is not included. Future users of this script might need to modify the code accordingly as these parameters are dependent on the atomic system of interest. As a final caution, the calculations break down for very low intensities where the ionization rates become extremely small. This is due to a limitation in the computer to represent numbers small enough without simply rounding to zero. The user should investigate the validity of the output yield values before using them for future applications. In general, the break down yield values occur in intensity ranges that are not realistic for most applications.

```
#  Utilizes intensity averaging from Chang et al, PRA vol47 num5 (1993)
#  mainly equations 13, 14 ,and 15

import math as ma
import numpy as nu
import os
import matplotlib.pyplot as plt

envelope_file = 'envelope.txt' # input .txt file arb. pulse envelope
time_file = 'time.txt' #in fs, input .txt file arb. pulse time array
phase_file = 'phase.txt' #in rad, input .txt file arb. pulse phase
path_base = '' # folder path for saving
file_name = '' # file name for saving the yield

# Sample input:
# He 24.5874, 54.417760 #Ip first and second
# Ne 21.5646, 40.96296
# Ar 15.7596, 27.62965
# Kr 13.9996, 24.35984
# Xe 12.1298, 20.9750

Ipot = 15.7596 #in eV, Ionization potential first ion
Ipot2 = 27.62965 #in eV, Ionization potential second ion
wavelength = 1940 #in nm, center wavelength
Imax = 1E15 #in W/cm^2, Intensity range max
Imin = 1E12 #in W/cm^2, Intensity range min
Istep = 5e+11 #in W/cm^2, Intensity step size
method = 'YI' # theory method 'YI' or 'ADK'
scale_factor = 1 # arbitrary scaling factor to help with numerical limitations
                    # Note,This destroys any ability to directly compare methods

def ADKRate(single_inten = 0, wavelength = 0, Ipot = 0, Z = 1, envelope = [],
    l = 0, m = 0):

        # Input ADKRate(inten in W/cm^2, wavelength in nm, Ipot in eV,
        # ion charge, pulse duration in s)
        # Calculates the cycle averaged ionization rate of an atom
        # in a laser field.  This comes from
        #M. V. Ammosov, N. B. Delone, and V. P. Krainov,
        # Sov. Phys. JETP 64, 1191 (1986).
        Ip = Ipot/27.211
        E = Ipot/27.211
        w = ((3E8/(wavelength*10**-9))*2*3.1415926)*2.419E-17
        kappa = ma.sqrt(2*Ip)
        Dt = 2*3.14159/w
        F = (nu.sqrt((single_inten)/(3.5E16)))*envelope
        omegas = Ip
        omegat = F/((2*Ip)**(0.5))
        nstar = Z*((2*E)**(-0.5))
        lstar = nstar-1
```

```
51          G = (2*l+1)*(ma.factorial(l+ma.fabs(m)))*(2**(-ma.fabs(m)))/((
52          ma.factorial(ma.fabs(m)))*(ma.factorial(l-ma.fabs(m))))
53          c_squared = (2**(2*nstar))/(nstar*ma.gamma(nstar+lstar+1)*ma.gamma(
54          nstar-lstar))
55          Wstat = omegas*c_squared*G*((4*omegas/omegat)**((2*nstar)-m-1))*nu.exp(
56          (-4*omegas)/(3*omegat))
57          W_star = ((((3*F)/(ma.pi*(kappa**3)))**0.5)*Wstat)/2.419E-17
58          #Rate in 1/s
59          W = (ma.fsum(W_star))*Dt*2.419E-17
60          return float(W)
61
62  def YIRate(single_inten = 0, wavelength = 0, Ip = 0, Z = 1, Dt = 0,
63      envelope = [], phase = [], time = [], theta = []):
64
65      # Calculates the instantaneous ionization rate of an atom
66      # in a laser field.  This comes from
67      # "Nonadiabatic tunnel ionization: Looking inside a laser cycle"
68      # G L Yudin and M Yu Ivanov, Phys Rev A 64, 013409 (2001)
69      # Mostly from eq. 17.
70      # exponential part of the rate
71      f = envelope
72      E = (((nu.sqrt((single_inten)/(3.5E16))*f)))
73      omega = 2*ma.pi*3E17/4.134E16 / wavelength  #laser angular freq in a.u.
74      gam = (2.32E6*nu.sqrt(Ip/(single_inten*(
75      wavelength*1E-3)**2)))/f #Keldysh parameter
76      a = 1 + gam**2 - nu.sin(theta)**2
77      b = nu.sqrt(a**2 + 4*gam**2*nu.sin(theta)**2)
78      c = nu.sqrt( ( nu.sqrt((b+a)/2)+gam )**2 + ( nu.sqrt((b-a)/2)+nu.fabs(
79      nu.sin(theta)) )**2 )
80      phi = ( gam**2 + nu.sin(theta)**2 + 0.5 ) * nu.log(c) - (3*nu.sqrt(b-a)/(
81      2*nu.sqrt(2)) * nu.fabs(nu.sin(theta)) ) - nu.sqrt(b+a)/(2*nu.sqrt(2))*gam
82      rateexp = nu.exp( -E**2*phi/(omega**3)) * 4.134E16 #exponential rate
83      # pre-exponential term
84      # We include l and m quantum numbers that we set to zero.
85      # gamma(x) is the gamma function.
86      el = 0              #angular quantum number
87      m = 0              #magnetic quantum number
88      Ei = Ip/27.2       #ionization potential in Hartrees
89      nstar = Z/(ma.sqrt(2*Ei))    #effective quantum number
90      lstar = nstar-1         #effective angular quantum number
91      A1 = 2**(2*nstar) / ( nstar*ma.gamma(nstar+lstar+1)*ma.gamma(nstar-lstar) )
92      B1 = (2*el+1)*ma.factorial((el+ma.fabs(m))) / (2**ma.fabs(m)*ma.factorial(
93      ma.fabs(m))*ma.factorial(el-ma.fabs(m)))
94      kappa = nu.log(gam+nu.sqrt(gam**2+1)) - gam/(gam**2+1)
95      preexp = A1*B1*Ei * (2*(2*Ei)**1.5/E)**(2*nstar-nu.fabs(m)-1) * nu.sqrt(
96      3*kappa/(gam**3))
97      # rate in units of s^-1.
98      rate_star =  preexp * rateexp
99      rate = ma.fsum(rate_star)*(Dt*1e-15)
100     return float(rate)
```

```
101
102 def read_array(file = 'default_name'):
103     with open(file, 'r') as f:
104         array = [float(line[:-1]) for line in f]
105     return array
106
107 def write_array(file_save = 'data_default.txt', data = []):
108     fw = open(file_save, 'w')
109     [fw.write(str(y)+'\n') for y in data]
110     fw.close()
111
112 ###############################################################################
113
114 # Read in pulse info
115 os.chdir(path_base)
116 envelope = nu.array(nu.float_(read_array(envelope_file)))
117 time = nu.array(nu.float_(read_array(time_file)))
118 phase = nu.array(nu.float_(read_array(phase_file)))
119 # Find Dt
120 Dt = abs(time[0] - time[1])
121 # Find intitial intensity values
122 dI = Imin/100 # Intensity Step
123 I = nu.array([float(a)*dI+0.01 for a in range(0, int(round((
124 Imax-0.01)/dI)))]) # Initial Intensity array
125 I_au = I/3.5E16 #Intensity in Atomic Units
126 init_length = len(I)
127 inten = nu.array([float(a)*Istep+Imin for a in range(
128 0,int(round((Imax-Imin)/Istep)))])
129 inten_length = len(inten)
130 # Generate the space for the arrays
131 N = nu.array([float(0) for a in range(0,inten_length)])
132 # Generate the space for the arrays
133 P_sub_sub = nu.array([float(0) for a in range(0,init_length)])
134 count = 0
135 # calculate theta for YI method only
136 omega = 2*ma.pi*3E17/4.134E16 / wavelength  #laser angular freq in a.u.
137 theta = omega*((time*1e-15)/2.419E-17) + phase
138 theta_length = len(theta)
139 for xxx in range(0,theta_length):
140     while theta[xxx] >= 3.1415962/2:
141         if theta[xxx] >= 3.1415962/2:
142             theta[xxx] = theta[xxx] - 3.1415962
143 # Calculate Rates and Probabilities for initial intensity Imin
144 for uu in range(0,init_length):
145     print('Points left: ' + str(init_length-uu))
146     if method == 'ADK':
147         # call ADK
148         rate_1_sub = ADKRate(I[uu], wavelength, Ipot, 1, envelope,
149         0, 0)/scale_factor  #Ionization rate of the first ion
150         rate_2_sub = ADKRate(I[uu], wavelength, Ipot, 2, envelope,
```

```
151         0, 0)/scale_factor  #Ionization rate of the second ion
152     if method == 'YI':
153         # call YI
154         rate_1_sub = YIRate(I[uu], wavelength, Ipot, 1, Dt, envelope, phase,
155         time, theta)/scale_factor #Ionization rate of the first ion
156         rate_2_sub = YIRate(I[uu], wavelength, Ipot2, 2, Dt, envelope, phase,
157         time, theta)/scale_factor #Ionization rate of the second ion
158     # Calculate Probability using both ion1 and ion2 rates
159     if ((rate_2_sub)-(rate_1_sub)) == 0:
160         P_sub_sub[uu] = 0
161     else:
162         P_sub_sub[uu] = ((rate_1_sub)*((ma.exp(-(rate_1_sub)))-(
163         ma.exp(-(rate_2_sub))))/((rate_2_sub)-(rate_1_sub)))
164     if init_length-uu == 1:
165         plt.plot(I[:uu], P_sub_sub[:uu])
166         plt.xscale('log')
167         plt.ylabel('some numbers')
168         plt.show()
169     if  count <= inten_length-1:
170         if I[uu-1] < inten[count] and inten[count] <= I[uu] and uu > 0:
171         # Volume averaging and Yield
172             P = P_sub_sub[:uu]
173             I0 = inten[count]/3.5E16
174             X3 = (((2*I_au[:uu]+I0)/(I_au[:uu]**2))*nu.sqrt((I0/I_au[:uu])-1))
175             N[count] = ma.fsum(X3*P) #Final Yield array
176             count += 1
177             del P
178             del X3
179 del count
180 # Save the yield and intensity arrays
181 write_array(file_name, N)
182 write_array('inten.txt', inten)
```

Figure A.1

A.2 Robust Fitting Code

File Name: robust_fitting.p

Language: Python 3.x

The purpose of this script is to perform the robust fitting method outlined in section 4.3.2 for use in the intensity calibration procedure outlined in this thesis. In essence, this script will output the best fit, comparing experiment to theory, scaling parameters, a and l. The parameter a linearly scales the power array of the experimental input and the l parameter linearly scales the theoretical ionization yield input. These parameters are automatically determined by the code based on the input data, however, the number of a parameters to be tested is determined by the user with the variable *points*.

As already mentioned, the script will compare ionization yield data from both an experimental source and a theoretical source. Typically, the theory data is the output from section A.1. Formatted as single columns in text files, *inten_file* is the intensity array (in W/cm^2) for the theoretical yield data, *N_file*. Please note that the input yield data should be nonzero. Similarly, formatted as single columns in text files, *plin_file* is the experimental power/photodiode value array (in arbitrary units) for the experimental yield data, *y1lin_file*. In addition, an array for the corresponding experimental error is included, *err_file*. This error is usually the standard error associated with the experimental yield and is used as part of the robust fitting procedure. The experimental data should always be represented as a function of some parameter (power, pulse energy) that is directly proportional to intensity. The parameters *start_ind* and *length_ind* are related to the experimental yield array. The user has the option to choose a subset of the experimental data, starting at a particular array index and defining the length of the subset. Knowledge of the original array length is required so as not to accidentally define a nonexistent subarray.

The remaining input parameters have to do with the robust fitting procedure and the removal of data points as described in section 4.3.2. In general, the starting number of points removed should be 1 for variable *minus_start*. This indicates that the first iteration

in the robust fitting procedure removes only one point. As the script progresses, it cycles through the fitting procedure for subsequent data points removed. The points removed are transparent to the user as the code runs, but can be determined in post analysis. As a good rule of thumb, the total number of points removed, *minus_end*, should not exceed half of the value given to *length_ind*.

As described earlier, the main output of this script is the best fit parameters a and l. These values are written to a single column text file with five outputs based on the best fit parameters: the weighted root mean square error, the best a value, the best l value, the normalization value for the experimental yield array used, and the normalization value for the theoretical yield array used. This output file is named "result_best_error_$\star$.txt", where $\star$ is the number of data points removed. In addition, the un-normalized experimental and and theoretical yields for each fit is output as "result_exp_$\star$.txt" and "result_thy_$\star$.txt", respectively.

Note that all of the information needed to properly calibrate the intensity used in an experiment is contained within the output of this script. The visualization of the analysis, see section 4.3.3, will have to be extracted from this output with a script not provided in this appendix.

```
# This program uses a robust fitting procedure to fit the theoretical yield data
# to experimental yield data as a function data points removed

# File Input:
path_base = '' # folder path for input files
N_file = '' # output yield .txt file from theory code
inten_file = '' # output intensity .txt file from theory code
plin_file = 'p.txt' # .txt file experimental power/photodiode values
y1lin_file = 'y.txt' # .txt file experimental yield values
err_file = 'e.txt' # .txt file experimental yield error values

# Sample Input:
points = 10000 # number of "a" calibration valuse to try (range auto determined)
start_ind = 1 # starting index of exp yield array
length_ind = 35 # length of exp yield array
minus_start = 1 # staring number of points removed (should be 1)
minus_end = 18 # max number of points removed
laser = 1 # artifact related to laser rep. rate (keep as 1)

###############################################################################

from scipy.interpolate import interp1d
#import math as ma
import numpy as nu
import os

###############################################################################

def find_Error(inten, N_orig, plin, y1lin, err, laser, start_ind, length_ind,
    a, remove_p, save):

    # Number of Initial l's
    l_num = 10000
    # Number of steps / 2 to focus around best l value
    step_num = 100
    # Number of new steps in new l range
    new_l_num = step_num * 100
    # determine the experimental data area of interest
    # determine experimental yield and intensity for that region
    s1 = start_ind
    s2 = start_ind + length_ind
    yield_test = y1lin[s1:s2]
    err_test = err[s1:s2]
    inten_test = a*(plin/laser)
    inten_test = inten_test[s1:s2]
    #Interpolate the theory to match the intensity points of the experiment
    N_f = interp1d(inten, N_orig)
    N_new = N_f(inten_test)
    N_max = max(N_orig)
    # array of constants for scaling the theory data
```

```
51      max_N_new = max(N_new/N_max)
52      l_min = min(yield_test/max(yield_test))/max_N_new
53      min_N_new = min(N_new/N_max)
54      l_max = max(yield_test/max(yield_test))/min_N_new
55      l = nu.arange(l_min,l_max,(l_max-l_min)/l_num)
56      l_length = len(l)
57      error, l_best_value, l_step = find_Error_sub(length_ind, remove_p,
58                                  yield_test, N_new, N_max, err_test, a, l_length,
59                                  l, 0)
60      error = None
61      l = None
62      l_length = None
63      new_l_max = l_best_value + (l_step * (step_num/2))
64      new_l_min = l_best_value - (l_step * (step_num/2))
65      if new_l_min < 0:
66          new_l_min = 2**(-32)
67      l = nu.arange(new_l_min,new_l_max,(new_l_max-new_l_min)/new_l_num)
68      l_length = len(l)
69      error, l_best_value, l_step = find_Error_sub(length_ind, remove_p,
70                                  yield_test, N_new, N_max, err_test, a, l_length,
71                                  l, save)
72      return error
73
74  def find_Error_sub(length_ind, remove_p, yield_test, N_new, N_max, err_test, a,
75      l_length, l, save):
76
77      # Find the RMS value of the theorey compared to the experimental data for
78      # many scaling constants
79      a1 = 1/(float(length_ind)+remove_p)
80      a2 = yield_test/(max(yield_test))
81      a3 = (N_new)/(N_max)
82      e1 = 1/((0.434*err_test/a2/(max(yield_test)))**2)
83      # Make matrices
84      a2_m, b2 = nu.asarray(nu.meshgrid(a2,range(0,l_length)))
85      e1_m, e2 = nu.asarray(nu.meshgrid(e1,range(0,l_length)))
86      a3_m, b3 = nu.asarray(nu.meshgrid(a3,range(0,l_length)))
87      a4_m, b4 = nu.asarray(nu.meshgrid(l,range(0,len(a3))))
88      a4_m = nu.transpose(a4_m)
89      # RMS
90      R = (nu.transpose(nu.multiply(e1_m,(nu.log10(a2_m) - nu.log10((a4_m *
91          a3_m)))**2)))
92      S = nu.sort(R, axis = 0)
93      M = nu.sum(S[remove_p:len(a3)], axis=0)
94      C = nu.sqrt(a1*(nu.sum(R, axis=0) - M))
95      # Determine the best error and best scaling constant
96      error = min(C)
97      best_l_ind = nu.argmin(C)
98      best_l = a4_m[best_l_ind]
99      best_l_value = best_l[0]
100     if save == 1:
```

```
        print('Best l: ' + str(best_l[0]))
        best = [error, a, best_l[0], (max(yield_test)), (N_max)]
        write_array('result_exp_' + str(abs(remove_p)) + '.txt', (a2*
        (max(yield_test))))
        write_array('result_thy_' + str(abs(remove_p)) + '.txt', (a3*(
        max(yield_test))*best_l[0]))
        write_array('result_best_error_' + str(abs(remove_p)) + '.txt', best)
        chi_2 = nu.sum(nu.divide((a2-(a3*best_l[0]))**2,(err_test*(
        max(yield_test)))**2))
        print('Chi Squared: ' + str(chi_2))

    l_step = abs(l[0] - l[1])
    return error, best_l_value, l_step

def read_array(file = 'default_name'):
    with open(file, 'r') as f:
        array = [float(line[:-1]) for line in f]
    return array

def write_array(file_save = 'data_default.txt', data = []):
    fw = open(file_save, 'w')
    [fw.write(str(y)+'\n') for y in data]
    fw.close()


################################################################################

for i in range(minus_start,minus_end+1):

    remove_p = -i
    print(str(remove_p))
    # Read in theory and exp data
    os.chdir(path_base)
    N = nu.array(nu.float_(read_array(N_file)))
    inten = nu.array(nu.float_(read_array(inten_file)))
    plin = nu.array(nu.float_(read_array(plin_file)))
    y1lin = nu.array(nu.float_(read_array(y1lin_file)))
    err = nu.array(nu.float_(read_array(err_file)))
    # generate some parameters and constant "a" to test
    inten_min = min(inten)
    inten_max = max(inten)
    s1 = start_ind
    s2 = start_ind + length_ind
    a_min = inten_min / (min(plin[s1:s2]/laser))
    a_max = inten_max / (max(plin[s1:s2]/laser))
    a = nu.linspace(a_min, a_max, num=points, endpoint=True)
    length_a = len(a)
    error_all = nu.array([float(0) for b in range(0,length_a)])
    # test each "a" and find the RMS error
    for i in range(0,length_a):
```

```
        a_in = a[i]
        error = find_Error(inten, N, plin, y1lin, err, laser, start_ind,
                length_ind, a_in, remove_p, 0)
        error_all[i] = error
        if i == 0:
            best_error = error
            best_a = a_in
        if error < best_error:
            best_error = error
            best_a = a_in
    # print the best results
    print('Best Error: ' + str(best_error))
    print('Best a: ' + str(best_a))
    # run the best "a" one last time and save the information
    error = find_Error(inten, N, plin, y1lin, err, laser, start_ind, length_ind,
    best_a, remove_p, 1)
```

Figure A.2

A.3 Time-of-Flight Analysis Code

File Name: ToF_analysis_function.m

Language: MATLAB R2014a

This functionalized MATLAB script is written to go through the raw time-of-flight data from the strong-field ionization experiments presented in this thesis and extract important measurements from the experiment, such as yield and integrated photodiode values. The output is a user named .mat file containing a variety of variables that include some of these desired measurement values.

We start with a brief description of how the raw ionization data is organized. Each data set is contained within a folder. The name of the folder is called the root name, *root*. The data is then further divided into scans, which represent one collection of waveplate angles or the full intensity range of the experiment. The user can input the number of scans into *scans*. Each scan is divided into channel A and channel B. These channels correspond to the channels of the oscilloscope. Typically, A is the TOF signal and B is the photodiode signal. Channel A is divided into three subarrays to save on space: A1, A2, and A3. The script currently only analyzes one of these subarrays at a time, chosen by the user with *file_name*. Each channel is further divided into the number of intensity points in the experiment with a maximum value of *points* - 1. The experiment is run in burst mode meaning that each intensity point file contains a 2D array with a TOF signal trace for a certain number of consecutive laser shots. The number of consecutive laser shots does not need to be known to the user.

The remainder of the input parameters correspond to the integration windows of the various ion signals, background signals, and photodiode signals. Details of the meaning of each window input parameter is contained within the code itself, however, in general, the window is based on array indices and high and low index bounds are chosen. Typically, the window is chosen by the user based on the ion signals at high intensity where the ion count rate is higher per laser shot. The window can also be chosen based on previous calibrations.

It is important to note that the subarrays A1, A2, and A3 are all chosen by the person collecting the data. The index windows do not necessarily have to be consistent across all data sets, i.e. one sample compared to another. In addition to the user defined integration windows, the user can also decide to impose a threshold, setting any data point to zero if it falls below some predetermined value. It is a form of background filtering. The threshold should be set based on the individual ion detected signal strength. This can vary depending on experimental conditions, such as MCP voltage, and should be investigated for every data set before setting the threshold value.

Briefly, we describe the most important saved variables contained within the output .mat file. Of the following, each is a multidimensional array in the format parameter(continuous laser shots x intensity points x scans). y is the integrated ionization yield, *y_pressure* is the pressure corrected integrated ionization yield, *y_count* is the ionization yield and *y_count_pressure* is the pressure corrected ionization yield based on the counting method described in section 5.2.2. Similarly, there are variables pertaining to the yields of the background windows. The integrated photodiode signal is output as *p_int*.

```
% This function reads in the raw yield and photodiode data from the tof
% experiments.  The yield is both integrated within a window of the tof
% array or counted for individual ion detector hitsAll variables are saved
% to be used in other programs.

% Sample input:
% save_data_root = ''; % save folder path
% name = ''; % save name
% root = ''; % folder path to raw data. '_#' needed at the end for indexing
% file_name = 'A1_'; % Channel 1 save window of the scope (A1_, A2_, A3_)
% index_start = 1; % start index data sets with the same intial conditions
% index_finish = 1; % end index
% DIO = 1; %DIO for new data, y = 1, n = 0
% scans = 22; % number of scans
% points = 50; % number of waveplate angles
% bg_thresh_high = 600; % background yield threshold max
% bg_thresh_low = -320000; % background yield threshold min
% bg_thresh_set = 0; % all values in the threshold range become this value
% y_bg_low = 1400; % background window index low
% y_bg_high = 1800; % background window index high
% power_bg_thresh_high = -319999; % photodiode threshold max
% power_bg_thresh_low = -320000; % photodiode threshold min
% power_bg_thresh_set = 0; %all values in threshold range become this value
% p_bg_low = 1; % background window index low
% p_bg_high = 300; % background window index high
% data_region_high = 293; % yield window index yield
% data_region_low = 265; % yield window index low

function [] = ...
    ToF_analysis_function(save_data_root, name, root, ...
    file_name, index_start, index_finish, DIO, scans, points, ...
    bg_thresh_high, bg_thresh_low, bg_thresh_set, y_bg_low, y_bg_high, ...
    power_bg_thresh_high, power_bg_thresh_low, power_bg_thresh_set, ...
    p_bg_low, p_bg_high, data_region_high, data_region_low)

    % Save Initial Conditions
    cd(save_data_root)
    save_int_con = strcat(name,'_initial_conditions','.mat');
    save(save_int_con)
    %Program execution
```

```
    for k = index_start:index_finish
        [p_int] ...
            = load_power(k, scans, points, root, power_bg_thresh_high, ...
            power_bg_thresh_low, power_bg_thresh_set, save_data_root, ...
            name, DIO, p_bg_low, p_bg_high);
        load_yield(k, scans, points, root, bg_thresh_high, ...
            bg_thresh_low, bg_thresh_set, data_region_high, ...
            data_region_low, save_data_root, name, file_name, p_int, ...
            DIO, y_bg_low, y_bg_high);
    end
end

function [p_int] ...
    = load_power(k, scans, points, root, power_bg_thresh_high, ...
    power_bg_thresh_low, power_bg_thresh_set, save_data_root, name, ...
    DIO, p_bg_low, p_bg_high)
    % This function analyzes the data from the photodiode channel

    k_string = num2str(k);
    folder = strcat(root,k_string);
    % Load the IO Data, a file that says if data was taken for that step
    for i = 1:scans
        if DIO == 1
        scan = num2str(i);
        path = strcat(folder,'\Scan_',scan);
        cd(path)
        temp = load('Data_IO');
        data_IO(:,i) = temp;
        else
            data_IO(:,i) = ones(points,1);
        end
    end
    % Generate integrated photodiode array and corrected power
    for i = 1:scans
        i
        scan = num2str(i);
        path = strcat(folder,'\Scan_',scan,'\ChannelB');
        cd(path)
        for j = 1:points
            if data_IO(j,i) == 1
```

```
                point = num2str(j-1);
                file = strcat('B1_',point);
                p_all = load(file);
                pd_int_bg = sum(p_all(p_bg_low:p_bg_high,:))/ ...
                            (p_bg_high-p_bg_low);
                p_int_bg(:,j,i) = pd_int_bg;
                if i == 1 && j == 1
                    p_bg_zero = (pd_int_bg).*0;
                end
            else
                p_int_bg(:,j,i) = p_bg_zero;
            end
        end
    end
    % Polyfit background for ocsilloscope warm-up noise drift
    x_temp = reshape(p_int_bg,1,[]);
    x_temp_length = length(x_temp);
    ind = find(x_temp~=0);
    xx_temp = x_temp(x_temp~=0);
    x_temp2 = smoothing_function_for_inten_cal(xx_temp, 100);
    n = 20; %poly order
    x = 1:length(x_temp2);
    p = polyfit(x,x_temp2,n);
    x_temp3 = polyval(p,x);
    x_temp4 = zeros(x_temp_length,1);
    for r = 1:length(ind)
        x_temp4(ind(r)) = x_temp3(r);
    end
    p_int_bg_size = size(p_int_bg);
    p_int_bg_fit = reshape(x_temp4,[p_int_bg_size(1) p_int_bg_size(2) ...
                    p_int_bg_size(3)]);
    % Loop through the data files
    for i = 1:scans
        i
        scan = num2str(i);
        path = strcat(folder,'\Scan_',scan,'\ChannelB');
        cd(path)
        for j = 1:points
            if data_IO(j,i) == 1
                point = num2str(j-1);
```

```
121 -                   file = strcat('B1_',point);
122 -                   p_all = load(file);
123                     % Background clean
124 -                   p_all_size = size(p_all);
125 -                   temp_bg = reshape(p_int_bg_fit(:,j,i),[],1);
126 -                   for w = 1:p_all_size(2)
127 -                       temp_p_all(:,w) = p_all(:,w) - temp_bg(w,1);
128 -                   end
129 -                   temp = reshape(temp_p_all, [p_all_size(1)*p_all_size(2) 1]);
130 -                   temp2 = find(temp <= power_bg_thresh_high & temp >= ...
131                             power_bg_thresh_low);
132 -                   temp3 = temp;
133 -                   temp3(temp2) = power_bg_thresh_set;
134 -                   p_all = reshape(temp3, [p_all_size(1) p_all_size(2)]);
135                     % integrate
136 -                   pd_int = sum(p_all);
137 -                   p_int(:,j,i) = pd_int;
138 -                   if i == 1 && j == 1
139 -                       p_zero = (pd_int).*0;
140 -                   end
141 -               else
142 -                   p_int(:,j,i) = p_zero;
143 -               end
144 -           end
145 -       end
146         % save the analyzed power data
147 -       cd(save_data_root)
148 -       power_file = strcat(name,'_power_',k_string,'.mat');
149 -       save(power_file)
150 - end
151
152     function [] = load_yield(k, scans, points, root, bg_thresh_high, ...
153                 bg_thresh_low, bg_thresh_set, data_region_high, ...
154                 data_region_low, save_data_root, name, ...
155 -               file_name, p_int, DIO, y_bg_low, y_bg_high)
156 -               % Run this program second (after power program)
157                 % This program generates integrated yields of the data and
158 -               % also pressure corrects the data
159
160 -       k_string = num2str(k);
```

```
161 -       data_region_low_bg = y_bg_low;
162 -       data_region_high_bg = y_bg_low + abs(data_region_high ...
163                             - data_region_low);
164         % Data Location
165 -       folder = strcat(root,k_string);
166 -       cd(folder)
167         % Load the pressure Data
168 -       for i = 1:scans
169 -           scan = num2str(i);
170 -           path = strcat(folder,'\Scan_',scan);
171 -           cd(path)
172 -           temp = load('Pressure');
173 -           pressure(:,i) = (10.^(temp-11)).*1E6; %in microtorr
174 -       end
175         % Load the IO Data
176 -       for i = 1:scans
177 -           if DIO == 1
178 -           scan = num2str(i);
179 -           path = strcat(folder,'\Scan_',scan);
180 -           cd(path)
181 -           temp = load('Data_IO');
182 -           data_IO(:,i) = temp;
183 -           else
184 -               data_IO(:,i) = ones(points,1);
185 -           end
186 -       end
187         % Generate integrated yield array and pressure corrected yield array
188 -       for i = 1:scans
189 -           i
190             % Change folder
191 -           scan = num2str(i);
192 -           path = strcat(folder,'\Scan_',scan,'\ChannelA');
193 -           cd(path)
194 -           for j = 1:points
195 -               if data_IO(j,i) == 1
196                     % load data file
197 -                   point = num2str(j-1);
198 -                   file = strcat(file_name,point);
199 -                   y_all = load(file);
200 -                   yd_int_bg = sum(y_all(y_bg_low:y_bg_high,:))/ ...
```

```
                                (y_bg_high-y_bg_low);
                    y_int_bg(:,j,i) = yd_int_bg;
                    if i == 1 && j == 1
                        y_bg_zero = (yd_int_bg).*0;
                    end
                else
                    y_int_bg(:,j,i) = y_bg_zero;
                end
            end
        end
        % Polyfit background for ocsilloscope warm-up noise drift
        x_temp = reshape(y_int_bg,1,[]);
        x_temp_length = length(x_temp);
        ind = find(x_temp~=0);
        xx_temp = x_temp(x_temp~=0);
        x_temp2 = smoothing_function_for_inten_cal(xx_temp, 100);
        n = 20; %poly order
        x = 1:length(x_temp2);
        p = polyfit(x,x_temp2,n);
        x_temp3 = polyval(p,x);
        x_temp4 = zeros(x_temp_length,1);
        for r = 1:length(ind)
            x_temp4(ind(r)) = x_temp3(r);
        end
        y_int_bg_size = size(y_int_bg);
        y_int_bg_fit = reshape(x_temp4,[y_int_bg_size(1) y_int_bg_size(2) ...
                    y_int_bg_size(3)]);
        % Loop through the data files
        for i = 1:scans
            i
            % Change folder
            scan = num2str(i);
            path = strcat(folder,'\Scan_',scan,'\ChannelA');
            cd(path)
            for j = 1:points
                if data_IO(j,i) == 1
                    % load data file
                    point = num2str(j-1);
                    file = strcat(file_name,point);
                    y_all = load(file);
```

```
241                 % Background clean
242 -               y_all_size = size(y_all);
243 -               temp_bg = reshape(y_int_bg_fit(:,j,i),[],1);
244 -               for w = 1:y_all_size(2)
245 -                   temp_y_all(:,w) = y_all(:,w) - temp_bg(w,1);
246 -               end
247 -               temp = reshape(temp_y_all, ...
248                         [y_all_size(1)*y_all_size(2) 1]);
249 -               temp2 = find(temp <= bg_thresh_high ...
250                         & temp >= bg_thresh_low);
251 -               temp3 = temp;
252 -               temp3(temp2) = bg_thresh_set;
253 -               y_all = reshape(temp3, [y_all_size(1) y_all_size(2)]);
254                 % Find counts or integrate the data
255 -               y_all_int = sum(y_all(data_region_low: ...
256                     data_region_high,:));
257 -               y(:,j,i) = y_all_int;
258 -               y_pressure(:,j,i) = y_all_int./pressure(j,i);
259 -               y_region = y_all(data_region_low:data_region_high,:);
260 -               for n = 1:length(y_region(1,:))
261 -                   temp4 = find(y_region(:,n) > 0);
262 -                   count(n) = length(temp4);
263 -                   clearvars temp4
264 -               end
265 -               y_count(:,j,i) = count;
266 -               y_count_pressure(:,j,i) = count./pressure(j,i);
267 -               if i == 1 && j == 1
268 -                   y_zero = (y_all_int).*0;
269 -               end
270                 % Find counts or integrate the data for bg
271 -               y_bg_all_int = sum(y_all(data_region_low_bg: ...
272                                 data_region_high_bg,:));
273 -               y_bg(:,j,i) = y_bg_all_int;
274 -               y_bg_pressure(:,j,i) = y_bg_all_int./pressure(j,i);
275 -               y_bg_region = y_all(data_region_low_bg: ...
276                             data_region_high_bg,:);
277 -               for n = 1:length(y_bg_region(1,:))
278 -                   temp5 = find(y_bg_region(:,n) > 0);
279 -                   bg_count(n) = length(temp5);
280 -                   clearvars temp5
```

```
                    clearvars temp5
                end
                y_bg_count(:,j,i) = bg_count;
                y_bg_count_pressure(:,j,i) = bg_count./pressure(j,i);
                if i == 1 && j == 1
                    y_bg_zero = (y_bg_all_int).*0;
                end
                clearvars count bg_count
            else
                y(:,j,i) = y_zero;
                y_pressure(:,j,i) = y_zero;
                y_count(:,j,i) = y_zero;
                y_count_pressure(:,j,i) = y_zero;
                y_bg(:,j,i) = y_bg_zero;
                y_bg_pressure(:,j,i) = y_bg_zero;
                y_bg_count(:,j,i) = y_bg_zero;
                y_bg_count_pressure(:,j,i) = y_bg_zero;
            end
        end
    end
    % keep track of number of laser shots
    shots = length(y(:,1,1));
    laser_shots = (sum(transpose(data_IO))).*shots;
    % save the yield data
    cd(save_data_root)
    save_name = strcat(name,'_',k_string,'.mat');
    save(save_name)
end

function [x_smooth] = smoothing_function_for_inten_cal(x, points_avg)
        % a simple rolling average smoothing function with input array x to
        % be smoothed and number of points to average over

    points = round(points_avg/2)-1;
    x_smooth = x;
    for i = points+1:(length(x)- points)
        x_smooth(i) = mean(x((i-points):(i+points)));
    end
end
```

Figure A.3

A.4 Intensity Redistribution Code

File Name: Yield_power_rebin_function.m

Language: MATLAB R2014a

This functionalized MATLAB script is written to take some of the ionization yield output from the analysis code in section A.3 and redistribute it into new power/photodiode bins that were not necessarily the same as the bins originally intended by the person making the measurement. The yield values in each new power bin are output as an average value.

Typically, the user will take the following from section A.3 and rename them: *p_int* as *p_multi_2*, *y_pressure* as *y_multi_2* and *y_bg_pressure* as *bg_multi_2*. Based on the values of *p_multi_2*, the user can choose the maximum and minimum bin values for the power, *bin_max* and *bin_min*, respectively. The range of bin values chosen by the user are divided evenly in a log space with a user defined number of bins, *num_bins*. The distribution in log space is chosen to best mimic how the original intensity data points were distributed when the data was first collected. It is recommended that the user define the number of bins to be close to the number of intensity points from the original data set. The redistribution of the data points is meant to be a filter to help minimize experimental statistical error, as described in section 3.2.2.

```
% This function rebins the yield data based on the coresponding
% power/photodiode value within the newly defined bounds and finds and
% outputs the average yields and power/photodiode values of each bin and
% the corresponding standard error

% Sample input:
% load p_multi_2, y_multi_2, bg_multi_2, multidimantional arrays with the
% yield data,  power/photodiode data, and background yield data,
% respectively.  Generated from yield analysis program.
% num_bins = 50; % # of power/photodiode bins
% bin_min = 6000; % min power/photodiode value
% bin_max = 1.0713e+05; max power/photodiode value
% bg_constant = 0.02051; %constant bg subtraction from the yield

function [pd_best_avg,y_best_avg,y_best_error] = ...
    Yield_power_rebin_function(p_multi_2, y_multi_2, ...
    bg_multi_2, bin_min, bin_max, num_bins, bg_constant)

    % declare generic variables
    a = p_multi_2;
    aa = y_multi_2 - bg_multi_2;
    %BG subtraction
    aa = aa - bg_constant;
    % Reshape the data
    d = (reshape(a,[],1));
    dd = (reshape(aa,[],1));
    clearvars p_multi_2 y_multi_2
    % power/photodiode bin bounds evenly spaced in a log scale
    bin = logspace(log10(bin_min),log10(bin_max),num_bins);
    % Power discrimination for all of the data
    count = 0;
    for i=2:num_bins
       [ind_temp1] = find(bin(i-1) <= d & d < bin(i));
       d_new = d(ind_temp1,1);
       dd_new = dd(ind_temp1,1);
       if isempty(d_new) == 0
           count = count+1;
           P_int_new(count) = d_new;
           Y_new(count) = dd_new;
       end
```

```
41          clearvars d_new dd_new ind_temp1 ind_temp2
42      end
43      % putting the data in cells since the arrays are different sizes
44      for inten = 1:count
45          fprintf('Intensity Number: %i \n', inten);
46          pd_single = (P_int_new{inten}(:));
47          % power/photodiode average value within each bin
48          pd_best_avg(inten) = mean(pd_single);
49          % power/photodiode standard deviation within each bin
50          pd_best_error(inten) = std(pd_single);
51          % power/photodiode relative standard error within each bin
52          pd_best_rel_error(inten) = (std(pd_single)/ ...
53              sqrt(length(pd_single))./mean(pd_single);
54          % power/photodiode relative standard div. error within each bin
55          pd_best_std_rel_error(inten) = (std(pd_single))./ ...
56              mean(pd_single);
57          y_single = Y_new{inten}(:);
58          % yield average value within each bin
59          y_best_avg(inten) = mean(y_single);
60          % yield standard deviation within each bin
61          y_best_error(inten) = std(y_single)/sqrt(length(y_single));
62          % yield relative standard error within each bin
63          y_best_rel_error(inten) = (std(y_single)/ ...
64              sqrt(length(y_single))./mean(y_single);
65          % yield relative standard div. error within each bin
66          y_best_std_rel_error(inten) = (std(y_single))./mean(y_single);
67          y_length(inten) = length(y_single);
68      end
69  end
```

Figure A.4

A.5 SIMION Sequential Search VMI Electrostatic Lens Optimization Code

File Name: HITS_VMI.lua

Language: Lua to be used with SIMION

```
simion.workbench_program()

--====== variables

adjustable average = 0                  -- keep as 0
adjustable step = 100                   -- voltage step size of test voltage
adjustable best_voltage = 0             -- keep as 0
adjustable best_variance = 1000000000000        -- keep as a large number
adjustable particles = 60               -- total particles for all groups
adjustable v1_step = 20                 -- voltage step size of v1
adjustable v1_min = 800                 -- lower bound voltage for v1
adjustable v1_initial = 900             -- high bound voltage for v1
adjustable v2_step = 20                 -- voltage step size of v2
adjustable v2_min = 800                 -- lower bound voltage for v2
adjustable v2_initial = 900             -- high bound voltage for v1
adjustable rep = 1000                 -- repeller voltage
adjustable min_voltage = 0            -- lower bound voltage for test voltage
adjustable run_number = 0             -- rerun counter keep as 0
adjustable initial_voltage = 900      -- electrode voltage (current run)
adjustable request_rerun = 1          -- flag: request a rerun

local update_pe = true                -- mark PE display update at start of each run.

--====== subroutines

-- SIMION initialize segment.  Called on particle creation.
-- Set initial voltages and control reflying.
function segment.initialize()
    update_pe = true
    if run_number == 0 then
        test_voltage = initial_voltage
        v1 = v1_initial
        v2 = v2_initial    -- setup voltage for first run
    end
    -- If the last run cleared the rerun flag, we'll disable further reruns.
    -- (The current run will still execute.)
    sim_rerun_flym = request_rerun
end

-- Update electrode voltage.
function segment.fast_adjust()
        adj_elect01 = rep
        adj_elect02 = v1
        adj_elect03 = v2
-- voltage divider
        adj_elect04 = test_voltage
        adj_elect05 = test_voltage-(test_voltage*1/7)
        adj_elect06 = test_voltage-(test_voltage*2/7)
        adj_elect07 = test_voltage-(test_voltage*3/7)
        adj_elect08 = test_voltage-(test_voltage*4/7)
        adj_elect09 = test_voltage-(test_voltage*5/7)
        adj_elect10 = test_voltage-(test_voltage*6/7)
end

-- Update PE surface display.
function segment.other_actions()
    if update_pe then              -- if update flagged
        update_pe = false
        sim_update_pe_surface = 1       -- update the PE surface display
    end
end

-- SIMION terminate segment.  Called on particle termination.
function segment.terminate()

-- print("ion = " .. ion_number)
        parameter = Ion_Py_gu
```

```
-- intial set of temp variables
        if ion_number == 1 then
                test = 0
                variance = 0
                test2 = 0
                variance2 = 0
        end

-- find the variance on the second fly of particles and sum the positions for first group
        if ion_number <= particles/2 then
                test = test + parameter
                if math.fmod(run_number+1, 2) == 0 then
                        variance = variance + ((parameter - average)*...
                        (parameter - average))/(particles/2)
                else
                        variance = 0
                end
        end

-- Find the average of the first group
        if ion_number == particles/2 then
                average = test/(particles/2)
        end

-- find the variance on the second fly of particles and sum the positions for second group
        if ion_number <= particles and ion_number > particles/2 then
                test2 = test2 + parameter
                if math.fmod(run_number+1, 2) == 0 then
                        variance2 = variance2 + ((parameter - average2)*...
                        (parameter - average2))/(particles/2)
                else
                        variance2 = 0
                end
        end

-- find the variance on the second fly of particles and sum the positions for second group
        if ion_number == particles then
                average2 = test2/(particles/2)
                average_var = (variance + variance2)/2

-- find the total variance of the two groups
                variance_total = (((variance - average_var)*(variance - average_var))+...
                ((variance2 - average_var)*(variance2 - average_var)))/2

                if math.fmod(run_number, 2) == 0 then
                else
-- determine if the variance is the best variance
                        if best_variance >= variance_total then
                                best_variance = variance_total
                                best_voltage = test_voltage
                                best_v1 = v1
                                best_v2 = v2
                        end
-- move to next test voltage
                        test_voltage = test_voltage - step
                end

                run_number = run_number + 1

                if request_rerun == 1 then

-- display results
                print("n = " .. run_number ..
                        ", var = " .. variance ..
                        ", volts = " .. test_voltage ..
                        ", v1 = " .. v1 ..
                        ", v2 = " .. v2)
                end
```

```
-- Update voltages in sequential manner
                if test_voltage < min_voltage then
                        test_voltage = initial_voltage
                        run_number = run_number + 1
                        v2 = v2 - v2_step

                        if v2 < v2_min then

                                v2 = v2_initial
                                v1 = v1 - v1_step
                        end
                end
        end
-- if the last voltage is reached, display the final results
        if v1 < v1_min then

        request_rerun = 0       --  flag termination (if not already)
        print("best voltage = " .. best_voltage)
        print("best v1 = " .. best_v1)
        print("best v2 = " .. best_v2)
        end
end
```

Figure A.5